CONTROLLING PROPERTIES OF METAMATERIALS WITH CHIRAL FIELDS USING LIGHT AND CHIRAL MOLECULES

Christopher Kelly

School of Chemistry

University of Glasgow

A thesis submitted for the degree of

Doctor of Philosophy

December 2020

ABSTRACT

Metamaterials have unique and tuneable properties not found in nature, and the ability to control their properties is crucial to their applications. The desired properties can be attained through specific design of their physical structure, but often lack the ability to be dynamically control after being constructed. In this thesis it has been demonstrated that the properties of inorganic metafilms and chiral metamaterials can be manipulated post-fabrication by reversible perturbations from chiral electromagnetic fields and molecules. Such perturbations have been applied to chiral gold metamaterials that exhibit the plasmonic analogue of electromagnetically induced transparency. Circularly polarised light (that is chiral) and chiral molecules have been demonstrated to asymmetrically modify the coupling between electromagnetic modes in these metamaterials by their interactions with chiral nearfields. This experimental observation has then been validated by numerical electromagnetic simulations that replicate the effect, and confirm that asymmetries in the coupling are a result of differing optical chirality densities in the fields depending on the relative handedness of light, chiral nanostructure and chiral molecule. It has then also been shown that simulations can replicate asymmetries resulting from anisotropic chiral biomolecule (protein) layers on the metamaterial surface, by use of an anisotropic chiral response tensor. Luminescence spectroscopy has been used as a probe of changes in chemical symmetries of inorganic metafilms and metamaterials. Europium (III) oxide, Eu_2O_3, has been used owing to its strong luminescence and the sensitivity of those emissions to the europium symmetry environment. A luminescence microscope has been custom built and tested to optimise luminescence signal and stability. Chiral light interacting with unstructured films chiral nanostructures in the films have been shown to change the relative luminescence intensity of the hypersensitive transition in Eu_2O_3. A model describing the mechanism of these changes has been proposed involving the exchange of optical chirality between light and the films. From the continuity equation for the conservation of optical chirality density, it has been found that optical chirality from incident fields can be exchanged between materials at their interfaces. This exchange results in a bulk chiral polarisation of ions in the film that changes the electronic symmetry around the Eu^{3+} ion and its emission intensities. Electromagnetic simulations have validated this hypothesis by demonstrating an exchange of chirality into the film in a three-layer system (air, Eu_2O_3, polycarbonate).

University of Glasgow

College of Science and Engineering

Statement of Originality to Accompany Thesis Submission

Name: Christopher Kelly

Registration Number:

I certify that the thesis presented here for examination for a PhD degree of the University of Glasgow is solely my own work other than where I have clearly indicated that it is the work of others (in which case the extent of any work carried out jointly by me and any other person is clearly identified in it) and that the thesis has not been edited by a third party beyond what is permitted by the University's PGR Code of Practice.

I declare that the thesis does not include work forming part of a thesis presented successfully for another degree [unless explicitly identified and as noted below].

I declare that this thesis has been produced in accordance with the University of Glasgow's Code of Good Practice in Research.

I acknowledge that if any issues are raised regarding good research practice based on review of the thesis, the examination may be postponed pending the outcome of any investigation of the issues.

Signature:

CHRISTOPHER KELLY

Date: 18/12/20

TABLE OF CONTENTS

List of Figures

LIST OF TABLES

List of Abbreviations Used

EIT – electromagnetically induced transparency

SPP – surface plasmon polariton

LSP – localised surface plasmon

SPR – surface plasmon resonance

LSPR – localised surface plasmon resonance

LH – left-handed

RH – right-handed

CPL – circularly polarised light

ORD – optical rotatory dispersion

CD – circular dichroism

LCP – left circularly polarised / left circular polarisation

RCP – right circularly polarised / right circular polarisation

SEM – scanning electron microscope / scanning electron microscopy

TEM – transmission electron microscope / transmission electron microscopy

IgG – immunoglobulin G

NTA – thiolated nitrilotriacetic acid

HEPES - 4-(2-hydroxyethyl)-1-piperazineethanesulfonic acid

ATS – Autler-Townes splitting

AIC – Akaike information criterion

PIR – plasmon induced reflection

PIT – plasmon induced transmission

QWP – quarter wave plate

FEM – finite element method

EWFD – electromagnetic waves, frequency domain

CAD – computer-assisted design

PML – perfectly matched layer

IE – interface-exchange

OAM – orbital angular momentum

ACKNOWLEDGEMENTS

The road to completing this thesis has been long and challenging, what with global pandemics, worldwide protests and many unsuccessful experiments. I owe much of the fact that I am here at all to the many great colleagues, family and friends in my life who believed I could make it and helped me along the way, even when the outlook was bleak.

What can I say about the inimitable Professor Malcolm Kadodwala that hasn't already been said? Students and staff alike may fear his wrath but I cannot thank him enough for his efforts as my supervisor. He may have been tough at times but it was always in the service of pushing me to improve and progress. I would also like to thank Malcolm for having me in his group for the past four years, for recommending me for the temporary teaching position I hold at the university, and for giving the opportunity to travel to Japan for an international conference in 2018. Not to mention the raucous annual Christmas meal and pub crawl that we will sadly be missing out on this year. I could not have had the several published papers to my name and this completed thesis without his guidance and support.

I would also like to thank my second supervisor Adrian Lapthorn, for being a friendly voice when things were tough as well as for his advice and support when it came to teaching.

To Affar Karimullah, formerly a post-doc in Malcolm's group and now with his own group, I owe immense gratitude. His efforts in teaching me the ins and outs of COMSOL computer simulations, nanofabrication and the theory in our work gave me the strong foundation that allowed me to conduct the research present in this thesis. I appreciate his patience and his help when it came to co-authoring papers, figuring out complex maths, and navigating my way through a PhD.

Next, I wish to mention other current and former members of the Kadodwala group that I worked with over the years. Katie McKay and I collaborated closely in the early stages of the europium oxide project, and it was her work that built the material properties used for it in the simulations, and characterised its broadband optical behaviours. It was always a joy to work with Katie, and I appreciate the fun we had in Japan exploring Osaka and Tokyo. She was a good friend to have in the group, and always have a nice chat when I was stressed. Ryan Tullius taught me how to

use the reflectivity microscope and perform experiments with it, such that his setup became mine once he earned his PhD and left the group. It was a pleasure to meet his friends and family at his wedding reception, as well as to collaborate on the work for our co-authored JACS paper. I first worked with the Kadodwala group during my Masters, and at the time Marion Rodier was the PhD student I worked with on the project. Over the years I worked with Marion on several occasions, and made things more bearable with her good humour despite missing her home in France so much whilst in Glasgow. Oriol Roig and Cameron Gilroy were with the group about as long as I was, and time spent with them discussing work, hanging out over lunch and going for a pint after work was invaluable. I worked less closely with other group members but would still like to thank Dominic Koyroytsaltis-McQuire, Martin Kartau, Calum Jack, Maryam Hajji and Tarun Kakkar for being so welcoming, and making working in the group a rewarding experience.

There have been many Erasmus and Masters students in the Kadodwala group since I started and I would like to mention them here. Thanks to Richard for his help in building, testing, and performing early experiments with the luminescence microscope, Antoine for his work in the continuation of that project, and Anthony for his help on simulations and theory that was eventually published in Nature Communications this year. I owe them all a great deal of gratitude. Thank also to the other students including Gael, Laura, Ine, Amy, Yasmin, Stephanie, Machar, Esther, Mariona, Jules, and Travis, and I wish them the best with all of their future endeavours. Apologies to anyone whose name I have missed.

I would also like to thank the many members of staff in the School of chemistry for their support and insight, as well as those in the James Watt Nanofabrication Centre for sharing their knowledge and assistance with fabrication processes.

A final thank you goes out to my family and friends. My mum and dad, Pam and Peter whose care and support got me to this point, and to whom I owe the quality of life I lead today. They were always there to spend time with me when I needed it and I am eternally grateful for it (including my dad’s occasional advice on writing a PhD thesis). My sister Michelle and her fiancé Tom I thank for the games, tv-watching parties and chats that got me through writing during this pandemic. They and their two greyhounds, Spot and Rushy, were always there for me when I needed it. Lastly, thank to my friends Alasdair, Thomas, Appy, Jo, Cairn, Iain and Matthew for believing in me and supporting me when the going got tough.

Chapter 1 - INTRODUCTION AND THEORY

INTRODUCTION

Metamaterials have properties generally not found in nature and allow for specific optical properties to be engineered. They have applications in data storage, photovoltaics, telecommunications and sensing, and there has been a great deal of discussion and research into the potential use of metamaterials for invisibility cloaking technologies.[1–5] These applications rely on properties of metamaterials such as negative refractive index, electromagnetic bandgap, and nonlinearity, the last of which allows specifically designed metamaterials to mimic the quantum interference phenomenon known as electromagnetically induced transparency (EIT).[6,7] Chiral metamaterials allow for highly sensitive sensing, by exploiting the asymmetry in the optical responses of their chiral nearfields to chiral molecules.[8,9]

In this work chiral metamaterials will be studied using spectroscopy, with the intention to explore how and why their properties can be manipulated with chiral perturbations, such as chiral electromagnetic fields and molecules. This thesis is split into two major parts. The first section (covered by part 1 of the Theory as well as Chapters 3 and 4) is concerned with the chiroptical spectroscopy of gold chiral metamaterials. The EIT-like phenomenon in 'shuriken' shaped nanostructures will be studied, looking at asymmetries in the response of the structures to chiral light and chiral organic molecules. Experimental work will be validated by electromagnetic simulations, which will also allow electromagnetic properties such as the optical chirality density to be calculated so that the root causes of the asymmetries can be established. The second section (part 2 of the theory and Chapters 5 and 6) of the thesis involves using luminescence spectroscopy as a probe of changes in chemical symmetry of an inorganic film as a result of the exchange of optical spin from circularly polarised light. The specific material used is europium (III) oxide (Eu_2O_3) as the Eu^{3+} emissions are highly sensitive to the symmetry of its local environment. Changes in the emissions of Eu_2O_3 will be monitored when exposed to chiral light and chiral nearfields from nanostructures, and electromagnetic simulations designed to confirm the cause of the changes in the luminescence spectra will be run.

THEORY PART 1 – CHIROPTICAL SPECTROSCOPY OF PLASMONIC METAMATERIALS

In this section, background detail relevant to the thesis as a whole as well as the work in chapters 3 and 4 will be discussed, including optical activity and chirality as well as the spectroscopy of chiral plasmonic metamaterials. The second part of this theory chapter will deal with the remaining results chapters.

PLASMONICS

When an electromagnetic wave is incident on a metal particle or surface, the electric field can cause electron (or charge density) oscillations in the metal called plasmons. The plasmon induces an evanescent electric field - its strength decays exponentially with distance from the surface - at the metal surface with a frequency known as the plasma frequency, ω_p. The plasma frequency (**equation 1.1**) is dependent on the concentration, n_e, of charge carriers (electrons in this case) that have effective mass m^* and charge e, and is given by[10]

$$\omega_p = \sqrt{\frac{e^2 n_e}{\varepsilon_0 m^*}} \qquad [1.1]$$

When the frequency of the incident light matches the plasma frequency, they reach resonance, which when observed spectroscopically is seen as an intense peak resulting from an enhancement of the signal. The position and line shape of the resonance peak depends on the identity of the metal and its dielectric environment, as well as the size and shape of the metal particle or nanostructures i.e. a rod-shaped structure will produce a different resonance to a spherical one.[11]

Whether or not any given material is capable of supporting a plasmonic mode is determined by its permittivity. The result is that any number of different materials with similar permittivity will have close to identical optical response. This is because the information about charge carriers in those materials is defined only by their permittivity, so the solution to the wave equation for the plasmonic mode will not take into account the source of that complex permittivity, only its value. Generally speaking, for complex permittivity $\varepsilon_m = \varepsilon'_m + i\varepsilon''_m$, to support a plasmonic mode the real part must be negative and the imaginary part must be small.

The permittivity of a plasmonic material can be expressed by the Drude model in terms of the background permittivity from the bound electrons in the material ε_b, the plasma frequency and the incident light frequency ω as

$$\varepsilon_m = \varepsilon_b - \frac{{\omega_p}^2}{\omega(\omega + i\gamma_m)} \quad [1.2],$$

where γ_m is the electron scattering rate in that material, independent of the frequency.[12] In reality though, this model does not take into account phenomena in the material such as absorption owing to electronic transitions between energy bands, or that in some cases the assumption of the scattering being constant with frequency would no longer be valid.[13] Thus for accuracy this would need to be modified to with a frequency dependent scattering rate $\Gamma_m(\omega)$ and absorption behaviours. This modified Drude formula is given in **equation 1.3**, in which each interband transition is modelled as a Lorentzian absorption with amplitude f_n, central frequency ω_n and line-broadening term γ_n

$$\varepsilon_m = \varepsilon_b - \frac{{\omega_p}^2}{\omega\big(\omega + i\Gamma_m(\omega)\big)} + \sum_n \frac{f_n \omega_n}{{\omega_n}^2 - \omega^2 + i\omega\gamma_n} \quad [1.3],$$

and the summation represents each absorption term being added as its own alteration to the permittivity.

If a plasmon is induced at a continuous surface it is referred to as a surface plasmon polariton (SPP) and is able to propagate along the surface until it dissipates as heat in the metal. The relationship between the SPP generated at a metal surface and the light incident on that surface is given by the dispersion relation, **equation 1.4.**[14] It relates the wavevector k of the electromagnetic field in free space to that of the SPP, k_{SPP}. This relation arises when examining the relationship between the z- and x-components of the electric field in the metal and dielectric when illuminated with light normal to its surface, and results in the wavevector and hence momentum of the SPP being higher. To account for this discrepancy, the light and SPP must only couple at the surface when $\varepsilon_m + \varepsilon_d = 0$. This leads to the equation for the frequency of the SPP ω_{SPP} (**equation 1.5**), where ε_d is the permittivity of the dielectric material at the metal surface, showing that its frequency will be lower than the plasma frequency of the bulk metal.

$$k_{SPP} = k\sqrt{\frac{\varepsilon_d \varepsilon_m}{\varepsilon_d + \varepsilon_m}} \quad [1.4]$$

$$\omega_{SPP} = \frac{\omega_p}{\sqrt{1 + \varepsilon_d}} \quad [1.5]$$

A surface plasmon that is confined to a discrete particle whose dimensions are smaller than the wavelength of the incident light is called a localised surface plasmon (LSP).[15] Schematics of the differing SPP and LSP excitation mechanisms are shown in **figure 1.1**. SPPs and LSPs can be used for a variety of applications, including surface enhanced spectroscopies such as surface enhanced Raman spectroscopy and surface enhanced infrared absorption as well as biosensing techniques like surface plasmon resonance (SPR) and localised surface plasmon resonance (LSPR).[3,16–20] SPR and LSPR operate by detecting the change in the refractive index, Δn, at a surface as a result of an adsorbed layer of molecules, allowing for both biological and chemical sensing. This can be done by, for example, measuring the reflectivity of the metal surface over a range of wavelengths which includes the resonance, and then detecting the shift in wavelength of the peak in the presence of an adsorbed layer. The shift scattering wavelength peak in LSPR spectroscopy, for example, in which a nanoparticle with bulk refractive index response m has an adsorbed layer of thickness d can expressed as[21]

$$\Delta\lambda = m\Delta n\left[1 - e^{-2d/l_d}\right] \quad [1.6],$$

where l_d is the electromagnetic field decay length characteristic of LSPR.

In some cases, the metal structures that support plasmonic modes will be designed such that their shape and electric fields have a sense of twist, referred to generally as chirality. This property now will be discussed, as the nanostructures used in this thesis will all be chiral and their exact natures will be described in the relevant chapters.

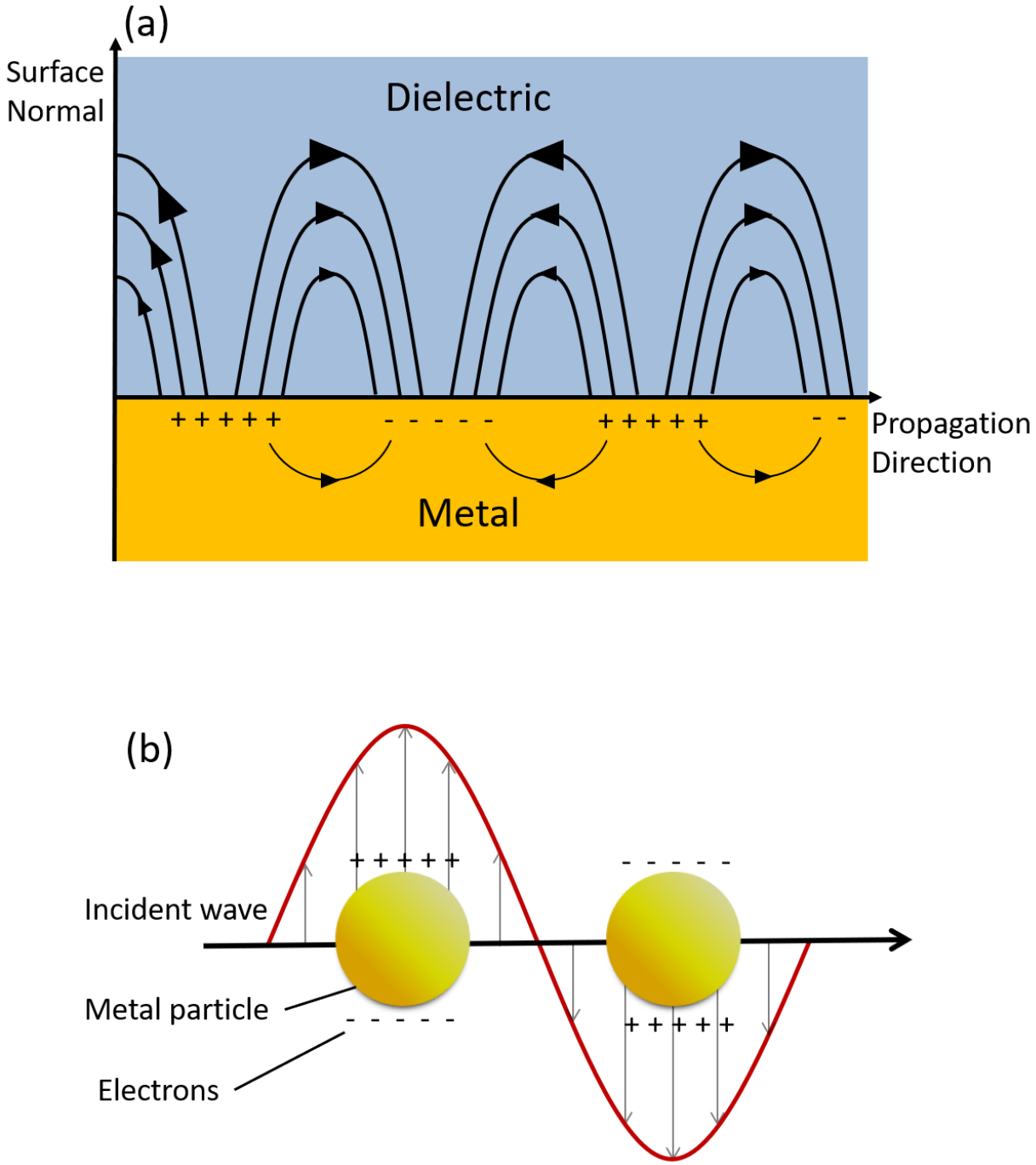

Figure 1.1. A Representation of the Mechanisms of SPP and LSP Excitation. The electric field of the incident wave causes electron oscillation in (a) a metal surface at its interface with a dielectric resulting in the propagation of a surface plasmon, and (b) metal particles which are smaller than the wavelength of light, resulting in an LSP. The movement of charge at the surface or within the particle is represented by '-' for electrons, '+' for the resulting positive charge and arrows in the diagrams.

Chirality in Chemistry

Chirality is a property an object has if it can exist in mirror-image forms which are not superimposable. This property manifests at a wide range of scales, from small single molecules to larger macrostructures, and can even be observed in nature – the spirals in a snail shell are chiral. Pairs of mirror image molecules or structures are called enantiomers. Larger, non-molecular structures can also be chiral, a simple example of which is a person's hands. In fact, it is for this reason that chiral objects can be referred to as left-handed (LH) and right-handed (RH) to differentiate between them, a convention which is frequently used in this work. In general a chiral structure lacks mirror symmetry planes, but may have rotational symmetry.[22,23]

A molecule can be considered chiral if it has one or more chiral stereocentres, such as carbon atoms where each of its four bonded groups is different. The enantiomers of a chiral molecule are often given labels to differentiate them, and how the label is assigned depends on the context in which the molecule is being used. The rules introduced by Cahn, Ingold and Prelog provide an unambiguous naming convention to ascribe the 'handedness' of chiral centres in molecules, labelling them as 'R' or 'S' (referring to the Latin *rectus* and *sinister* for right and left respectively).[24] Note that a molecule with several chiral centres may have a mixture of R and S stereochemistry. The rules involve assigning a 'priority' to each group bound to the chiral centre and following an imagined arrow from the highest priority group to the lowest. If the arrow rotates clockwise the centre is R, and anti-clockwise it is S. The priority is most simply assigned according to the atomic number of the constituents, with the highest atomic number (or atomic mass when considering isotopes of the same element) being highest priority. Further rules exist to distinguish between groups that appear to have the same priority, involving what is bonded to the constituents on the chiral centre further down the chain. The R and S labels are not the only identifiers that have been used historically however – amino acids, the building blocks of proteins, are all chiral with the exception of Glycine and are given the labels L and D (laevorotatory and dextrorotatory) to distinguish enantiomer pairs. This assignment is based on the relationship the molecule has to the equivalent configuration of D- or L-serine and hence D- or L-glyceraldehyde.[25] The result is that there is not necessarily a connection between the Cahn-Ingold-Prelog labels and the older D and L labels for amino acids.

Many naturally occurring biological molecules are chiral, including the smaller building blocks like amino acids and sugars (**figure 1.2a, b**), as well as larger structures such as proteins and DNA (**figure 1.2c, d**). These building blocks are known to be 'homochiral', or enantiopure, meaning that their naturally occurring forms in living organisms exist only as one enantiomer; in proteins there are only L-amino acids and only D-sugars form the backbone of DNA and RNA.[26] In addition, the larger molecules are organised into higher order structures that are themselves chiral. For example, proteins contain secondary structure features such as α-helices whose chirality is determined by the sense of their rotation, as well as β-sheets in which chirality can arise from twists in their conformation, owing to the arrangement of constituent amino acids.[27,28]

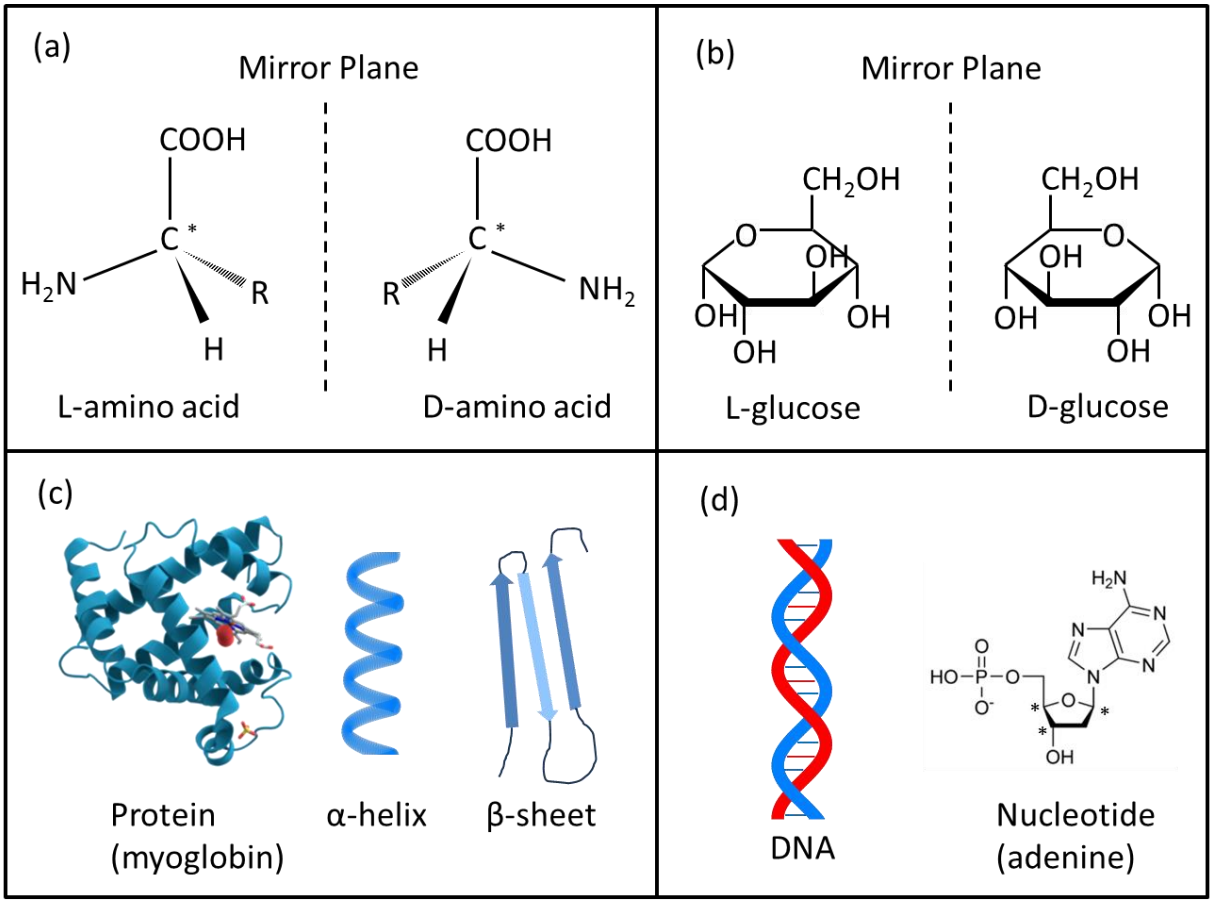

Figure 1.2. Examples of Chiral Biomolecules. (a) Amino acids (other than glycine) are chiral and exist in the shown enantiomer pairs, as do (b) sugars such as glucose. These small units make up (c) proteins that have chiral secondary structure such as α-helices and β-sheets, and (d) DNA that is organised in a chiral helix, respectively.

Chirality is also a vital consideration in pharmaceuticals, as often only one enantiomer of a certain molecule exhibits the desired biological activity. The other enantiomer will be inactive at best, or at worst dangerous to the recipient. For example, *(S)*-penicillamine can be used to treat Wilson's disease and metal poisoning by removing heavy metals, and can also treat rheumatoid arthiritis. However, its enantiomer *(R)*-penicillamine is known to cause severe reactions such as optic neuritis (inflammation of the optic nerve that can be damaging) and osteomyelitis (an infection causing pain in the bones).[29,30] A more well-known example is that of thalidomide, whose widespread use across the world in the 1950s lead to developmental problems and birth defects in children after thalidomide was taken to treat nausea in pregnant women. In this case, the *R* enantiomer is the bioactive molecule, and the *S* enantiomer is a teratogen.[31,32] Molecular structures of the enantiomers of penicillamine and thalidomide are shown in **figure 1.3.** Racemic mixtures (a mixture of each enantiomer of a molecule in equal amounts) may therefore contain one enantiomer which is far more active than the other, enantiomers of equal activity, or even enantiomers which undergo inversion in the body to their opposite. Thalidomide is an example of a molecule that can interconvert between its enantiomers, enabling it to 'self-racemise' – it can form a racemic mixture *in vivo*. Thus it can be important to synthesise molecules of only one enantiomer using a stereoselective process for instance, or to separate a mixture into a single form using an enantioselective process.[33]

Optical activity

The ability to determine the relative proportions of enantiomers in a mixture is thus crucial. This can be done using optical rotation, a method that exploits the optical activity of chiral molecules and structures. Optical activity arises from the differential interaction of circularly polarised light (CPL) with chiral materials (CPL is light whose electric field vector rotates in a circle as the light propagates). This phenomenon is often observed as optical rotation, in which plane polarised light (i.e., light whose electric field vector only oscillates in one direction orthogonal to the propagation direction) is rotated with respect to some defined axis as it passes through an optically active material. Circular dichroism is also a manifestation of optical acitivity.[34] In this work, only natural optical activity will be discussed; that which results from a material's intrinsic chirality.

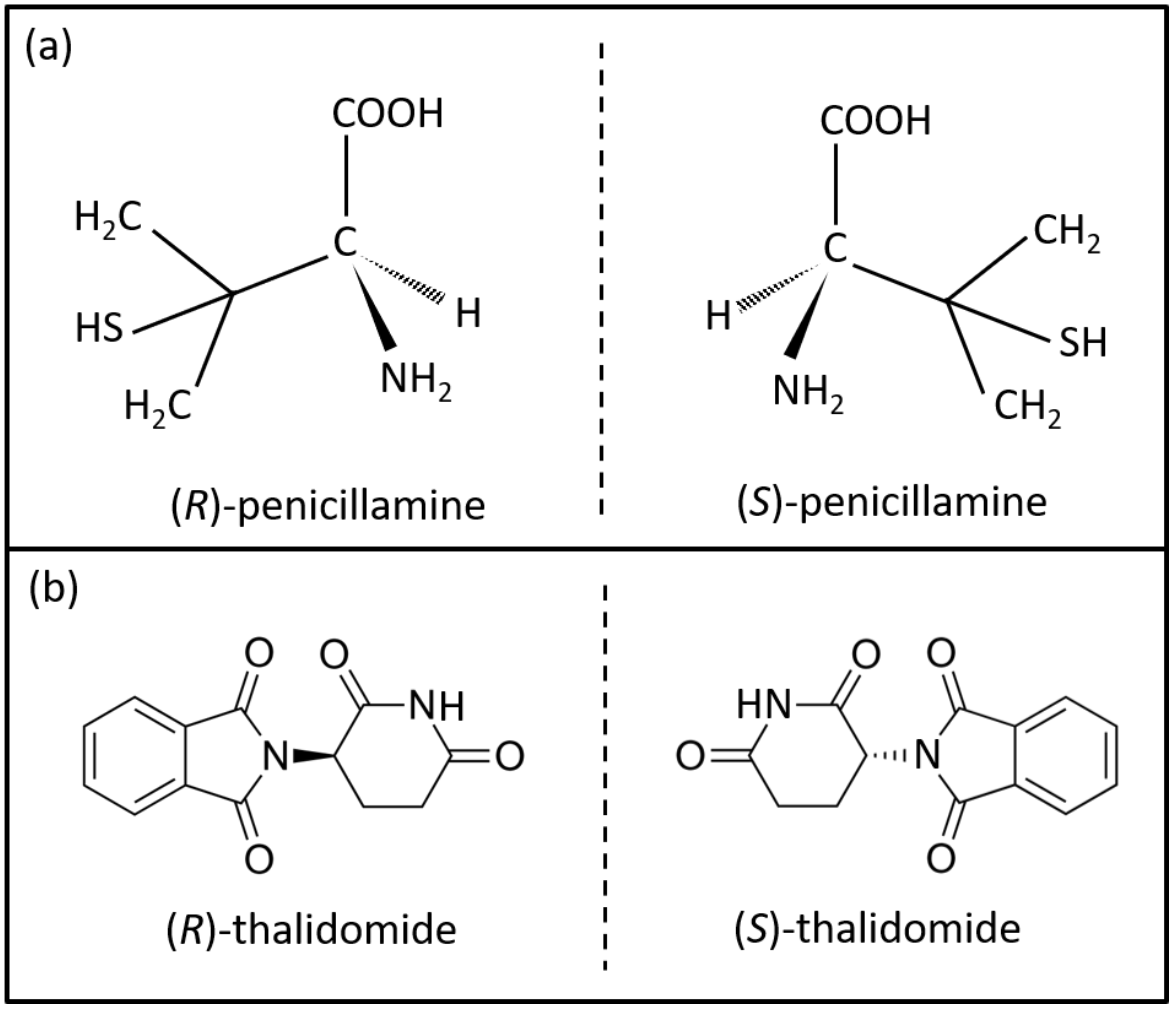

Figure 1.3. Molecular Structure of Chiral Pharmaceuticals. The structures of the R and S enantiomers of (a) penicillamine and (b) thalidomide. The dashed lines represent mirror planes, showing how the structure of one enantiomer can be obtained from the other. Pharmaceuticals like these demonstrate the importance of distinguishing between different enantiomers of a molecule, given the vastly different properties of each from its counterpart.

Note that optical activity can arise in other ways such as by the application of a magnetic field causing asymmetric responses in a material. The manner in which light interacts with a magnetised material can be described by the Kerr and Faraday magneto-optical effects. Polarised light interacting at the surface of a magnetised substance is known as the magneto-optic Kerr effect, in which the light polarisation is rotated as it is reflected, and the magneto-optic Faraday effect instead sees polarised light rotating when it is transmitted through a magnetised material.[35–37] Magneto-chiral dichroism, in which the optical activity of a molecule changes in the presence of a magnetic field, may be observed in a substance which exhibits both natural and magnetic optical activity.[38–40] In any case, optical rotation will occur in the opposite sense for each of the two enantiomers, although for chiral molecules

the direction of rotation is not necessarily predictable from the label given to it (i.e. D- and L- for amino acids, S and R for absolute configuration); it must be measured. Other labels, notably the (+) and (-) prefixes, directly relate to the rotation direction – clockwise and anti-clockwise respectively – and may be added along with other labels to define the actual rotation. For example, L-amino acids may have (+) or (-) optical rotation, depending on the identity of the amino acid.

Optical rotation was first discovered by E. L. Malus in the early nineteenth century and Malus' law (**equation 1.7**) is named after him. Malus' Law describes how the irradiance I of a polarised light beam of incident irradiance I_o varies as it passes through a perfect polarising material, and is written[41]

$$I = I_0 \cos^2 \theta \qquad [1.7].$$

Such a material known as a polariser will have a designated plane of polarisation, generally indicating the polarisation direction that can be transmitted through the polariser completely. Thus, the irradiance, by Malus' Law, depends on the angle θ that the incident light polarisation makes with respect to the polariser plane.

Optical activity was later quantified by J. B. Biot who discovered the dependence of optical rotation on the thickness of the material through which the light is passing.[42] Experimentally, the optical rotation of a given sample can be measured with a polarimeter – in instrument in which plane polarised light is passed through the sample then through an analyser (a second linear polariser) so that when the analyser is either rotated to block out the light or let the maximum amount through, the angle α through which the light rotated can be determined. Given that the optical rotation depends on both the length l of sample the light passed through and its density ρ (or its concentration if it is a solution rather than a pure liquid) a property called specific rotation that is independent of these factors, $[\alpha]_\lambda^T$, can be calculated using

$$[\alpha]_\lambda^T = \frac{\alpha}{l\rho} \qquad [1.8],$$

where the labels T and λ refer to the measurement temperature and wavelength of incident light respectively.[43]

The techniques of optical rotatory dispersion (ORD) and circular dichroism (CD) can be used to give information on how the optical activity of a substance varies with light frequency. In ORD, the optical rotation is measured over a light spectrum whereas in CD the differential absorption of left-handed and right-handed circularly polarised light by the sample is measured. This then provides information on the chirality and structure of a sample, as a particular enantiomer or chiral secondary protein structure will preferentially absorb one handedness of light over the other.[44] As linearly polarised light can be considered a superposition of equal parts left circularly polarised (LCP) and right circularly polarised (RCP) light such that a differential amount of one handedness being absorbed results in rotation of the light, the ORD and CD are intrinsically linked. Indeed, in principle the Kramers-Krönig relations, which are generally used to connect the real and imaginary parts of complex functions, can be used to interconvert ORD and CD spectra.[45,46]

Optical Chirality

In electromagnetics, a vast number of quantities must be conserved in interactions within the fields, including energy, linear and angular momentum and charge, and the origin of these conserved quantities is found in Noether's theorem.[47–49] Maxwell's equations (**equations 1.9-1.12**)**,** a set of differential equations forming the fundamentals of electromagnetism, can be used to find solutions to optical problems and interactions of fields and matter. They also contain this information about conservation, and are defined by expressions for how the electric field $\boldsymbol{E}$ and magnetic field $\boldsymbol{B}$ are generated and changed by material charges (represented by charge density ρ), currents (current density $\boldsymbol{J}$) and each other:

$$\nabla \cdot \boldsymbol{E} = \frac{\rho}{\varepsilon_0} \qquad [1.9],$$

$$\nabla \cdot \boldsymbol{B} = 0 \qquad [1.10],$$

$$\nabla \times \boldsymbol{E} = -\frac{\partial \boldsymbol{B}}{\partial t} \qquad [1.11],$$

$$\nabla \times \boldsymbol{B} = \mu_0 \left(\boldsymbol{J} + \varepsilon_0 \frac{\partial \boldsymbol{E}}{\partial t} \right) \qquad [1.12],$$

where ε_0 and μ_0 are the free space permittivity and permeability respectively. For example, using the Maxwell-Faraday equation (**equation 1.11**) and Ampere's Law (**equation 1.12**) an expression describing the conservation of energy can be

obtained. It is a differential continuity equation known as Poynting's theorem (**equation 1.13**), where $\boldsymbol{S}$ is the Poynting vector or electromagnetic energy flux and U is the electromagnetic energy density:

$$\frac{\partial U}{\partial t} + \frac{1}{\mu_0}\nabla \cdot \boldsymbol{S} = -\boldsymbol{J} \cdot \boldsymbol{E} \qquad [1.13],$$

$$\boldsymbol{S} = \frac{\mathbf{1}}{\mu_0}(\boldsymbol{E} \times \boldsymbol{B}) \qquad [1.14],$$

$$U = \frac{1}{2}\left(\varepsilon_0 \boldsymbol{E} \cdot \boldsymbol{E} + \frac{1}{\mu_0}\boldsymbol{B} \cdot \boldsymbol{B}\right) \qquad [1.15].$$

The meaning of Poynting's theorem (and continuity equations in general for quantities besides energy), is that the rate of change of energy with time *t* within a given region is equal to the flow of energy out of that volume through its surface plus the rate of work done by the fields on charges in that region.[50] In free space, in the absence of any currents or charges, the right-hand side of **equation 1.13** becomes 0, such that any change in energy density over time is due to the flux of energy through the surface.

In 1964 Daniel Lipkin described a conserved quantity he had discovered, similar to conserved quantities such energy and momentum, that he termed the 'zilch' of the electromagnetic field.[51] As with energy in **equations 1.16-1.18**, the conservation of the zilch of an arbitrary field in a vacuum can be described by its own continuity equation (**equation 1.16**) as well as the zilch flux $\boldsymbol{S}_Z$ and density Z^0:

$$\frac{\partial Z^0}{\partial t} + \nabla \cdot \boldsymbol{S}_Z = 0 \qquad [1.16],$$

$$\boldsymbol{S}_Z = \frac{\varepsilon_0}{2}\boldsymbol{E} \times \frac{\partial \boldsymbol{E}}{\partial t} + \frac{1}{2\mu_0}\boldsymbol{B} \times \frac{\partial \boldsymbol{B}}{\partial t} \qquad [1.17],$$

$$Z^0 = \frac{\varepsilon_0}{2}\left(-\boldsymbol{E} \cdot \frac{\partial \boldsymbol{B}}{\partial t} + \boldsymbol{B} \cdot \frac{\partial \boldsymbol{E}}{\partial t}\right) \qquad [1.18].$$

In this original work, Lipkin noted that the behaviour of zilch flow is similar to that for fields with intrinsic spin, which he believed was an indicator of a possible physical interpretation of the zilch. Further work by Kibble a year later and others such as Przanowski et al in 1994 demonstrated that there are essentially infinite conserved

quantities that have bilinear density functions like the zilch, and that although few if any of the conservation laws associated with them have any physical or practical application, they do merit further study.[52,53]

In 2010 Tang and Cohen discussed the connection between the chirality of optical fields and the zilch.[54] They state that a chiral electromagnetic field, whose field lines twist around a central axis perpendicular to the rotation plane whilst also having a component parallel to the axis, have a density property called optical chirality that describes that geometry. The optical chirality density, *C*, takes the same form as the zilch density given in **equation 1.18**, which when combined with Maxwell's equations (**1.11** and **1.12**) in the absence of currents and charges gives

$$C = \frac{\varepsilon_0}{2}\boldsymbol{E}\cdot(\nabla\times\boldsymbol{E}) + \frac{1}{2\mu_0}\boldsymbol{B}\cdot(\nabla\times\boldsymbol{B}) \qquad [1.19],$$

where $\boldsymbol{E}$ and $\boldsymbol{B}$ are real, time *t* dependent fields with frequency ω given by

$$\boldsymbol{E}(\boldsymbol{r},t) = \boldsymbol{\mathcal{E}}(\boldsymbol{r})e^{-i\omega t} \qquad [1.20],$$

$$\boldsymbol{B}(\boldsymbol{r},t) = \boldsymbol{\mathcal{B}}(\boldsymbol{r})e^{-i\omega t} \qquad [1.21].$$

These fields and their time derivatives can then also be expressed as

$$\boldsymbol{E}(\boldsymbol{r},t) = \frac{1}{2}\mathrm{Re}\left[\boldsymbol{\mathcal{E}}(\boldsymbol{r})e^{-i\omega t} + \boldsymbol{\mathcal{E}}^*(\boldsymbol{r})e^{i\omega t}\right] \qquad [1.22],$$

$$\boldsymbol{B}(\boldsymbol{r},t) = \frac{1}{2}\mathrm{Re}\left[\boldsymbol{\mathcal{B}}(\boldsymbol{r})e^{-i\omega t} + \boldsymbol{\mathcal{B}}^*(\boldsymbol{r})e^{i\omega t}\right] \qquad [1.23],$$

$$\frac{\partial\boldsymbol{E}}{\partial t} = \frac{1}{2}\mathrm{Re}\left[-i\omega\boldsymbol{\mathcal{E}}e^{-i\omega t} + i\omega\boldsymbol{\mathcal{E}}^*e^{i\omega t}\right] \qquad [1.24],$$

$$\frac{\partial\boldsymbol{B}}{\partial t} = \frac{1}{2}\mathrm{Re}\left[-i\omega\boldsymbol{\mathcal{B}}e^{-i\omega t} + i\omega\boldsymbol{\mathcal{B}}^*e^{i\omega t}\right] \qquad [1.25].$$

where asterisks indicate the complex conjugate of the space-dependent fields $\boldsymbol{\mathcal{E}}$ and $\boldsymbol{\mathcal{B}}$**.** By modifying C with Maxwell's equations in free space (so that it takes the same form as the zilch, **equation 1.18**) and then inserting **equations 1.24** and **1.25**, the equation for the optical chirality density can be expanded

$$C = \frac{\varepsilon_0}{2} \times \frac{1}{4} \mathrm{Re}\left[-\left(\boldsymbol{\mathcal{E}} e^{-i\omega t} + \boldsymbol{\mathcal{E}}^* e^{i\omega t}\right) \cdot \left(-i\omega \boldsymbol{\mathcal{B}} e^{-i\omega t} + i\omega \boldsymbol{\mathcal{B}}^* e^{i\omega t}\right)\right]$$

$$+ \frac{\varepsilon_0}{2} \times \frac{1}{4} \mathrm{Re}\left[\left(\boldsymbol{\mathcal{B}} e^{-i\omega t} + \boldsymbol{\mathcal{B}}^* e^{i\omega t}\right) \cdot \left(-i\omega \boldsymbol{\mathcal{E}} e^{-i\omega t} + i\omega \boldsymbol{\mathcal{E}}^* e^{i\omega t}\right)\right]$$

$$= \frac{\varepsilon_0}{2} \times \frac{1}{4} \mathrm{Re}\left[i\omega \boldsymbol{\mathcal{E}} \cdot \boldsymbol{\mathcal{B}} e^{-2i\omega t} - i\omega \boldsymbol{\mathcal{E}} \cdot \boldsymbol{\mathcal{B}}^* + i\omega \boldsymbol{\mathcal{E}}^* \cdot \boldsymbol{\mathcal{B}} - i\omega \boldsymbol{\mathcal{E}}^* \cdot \boldsymbol{\mathcal{B}}^* e^{2i\omega t}\right.$$

$$\left. - i\omega \boldsymbol{\mathcal{B}} \cdot \boldsymbol{\mathcal{E}} e^{-2i\omega t} - i\omega \boldsymbol{\mathcal{B}}^* \cdot \boldsymbol{\mathcal{E}} + i\omega \boldsymbol{\mathcal{B}} \cdot \boldsymbol{\mathcal{E}}^* + i\omega \boldsymbol{\mathcal{B}}^* \cdot \boldsymbol{\mathcal{E}}^* e^{2i\omega t}\right]$$

$$= 2\omega \frac{\varepsilon_0}{2} \times \frac{1}{4} \mathrm{Re}\left[i\boldsymbol{\mathcal{E}}^* \cdot \boldsymbol{\mathcal{B}} - i\boldsymbol{\mathcal{B}}^* \cdot \boldsymbol{\mathcal{E}}\right] \qquad [1.26],$$

which leads to the time independent expression for optical chirality density

$$C = -\frac{\varepsilon_0}{2} \omega \mathrm{Im}\{\boldsymbol{\mathcal{E}}^* . \boldsymbol{\mathcal{B}}\} \qquad [1.27].$$

As with the other conserved quantities in electromagnetic fields, the optical chirality obeys a continuity equation whose form is recognisably similar to others discussed previously. A major difference however, in comparison to e.g., energy, is that when the chiral field interacts with matter not only must losses in the material owing to (for example) absorption be considered, but also the exchange of chirality at interfaces. This interface-exchange arises from gradients in the complex permittivity $\varepsilon = \varepsilon' + i\varepsilon''$, and complex permeability $\mu = \mu' + i\mu''$. The narrow-bandwidth chiral continuity equation for light-matter interactions is given by

$$\frac{\partial C}{\partial t} - i\omega \nabla \cdot \underbrace{\left[\varepsilon'(\boldsymbol{\mathcal{E}} \times \boldsymbol{\mathcal{E}}^*) + \mu'(\boldsymbol{\mathcal{H}} \times \boldsymbol{\mathcal{H}}^*)\right]}_{\text{chirality flux}} = +i\omega^2 \underbrace{(\boldsymbol{\mathcal{E}} \cdot \boldsymbol{\mathcal{H}}^* - \boldsymbol{\mathcal{H}} \cdot \boldsymbol{\mathcal{E}}^*)(\mu'\varepsilon'' + \varepsilon'\mu'')}_{\text{loss term}} +$$

$$i\omega \underbrace{\left[(\nabla\varepsilon') \cdot (\boldsymbol{\mathcal{E}} \times \boldsymbol{\mathcal{E}}^*) + (\nabla\mu') \cdot (\boldsymbol{\mathcal{H}} \times \boldsymbol{\mathcal{H}}^*)\right]}_{\text{interface-exchange term } (IE)}, \qquad [1.28].$$

This equation and its full implication will be discussed in more rigorous detail in chapter 6, when an exploration of the interface-exchange between chiral fields and matter becomes necessary.

Optical chirality density is a pseudoscalar, and a chiral system is parity-odd and even on time-reversal.[55] This means that if all spatial co-ordinates of a chiral system x, y, z are changed in sign to -x, -y, -z the optical chirality density also changes sign, but if time t is reversed the chirality retains its original sign. C can be used as a measure of chiral asymmetry in the interaction of chiral electromagnetic fields with matter, such as chiral molecules, nanoparticles or metamaterials.[56] The convention

held here is that a left-handed chiral field yields a positive value of C and a right-handed field a negative. A unique case of a chiral field is CPL, in which the optical chirality is given by

$$C_{CPL} = \pm \frac{2U_e}{\omega c} \qquad [1.29],$$

where U_e is the time-average electrical energy density and the convention above is maintained, i.e. that a positive value of C corresponds to LCP and a negative value to RCP.[54]

Light can carry angular momentum, and for a circularly polarised light beam it is in the form of spin angular momentum with quantised values of $\pm\hbar$ depending on if the beam is LCP or RCP. Orbital angular momentum is carried by beams with spatially varying phasefronts, such as Laguerre-Gauss beams.[57–59] The optical helicity of the light is the projection of its spin angular momentum vector onto its linear momentum, such that it is right-handed if they are parallel and left-handed if anti-parallel.[60] For massless particles such as photons, the helicity and chirality are essentially the same, and are related by the electric field energy density. This is because the direction of the spin vector will not change from the point of view of any observer as no observer can move faster than the speed of light, which would be necessary for this reversal of spin. Thus, for light the spin density can conveniently be quantified by the optical chirality.[59] However, the chirality and helicity differ in the case where particles have mass where it is possible an observer could move faster than the particle and see the spin as having reversed, and hence reversed the helicity. In this work only the chirality (and spin) of light and other electromagnetic fields will be considered, so this distinction between helicity and chirality is here for clarity only.

Superchirality

As suggested by the continuity equation (**1.28**) optical chirality density within a system must be conserved. Locally in space however, the density of the optical chirality in electromagnetic fields arising from light-matter interactions can increase beyond that of the same frequency circularly polarised wave, assuming that there is a compensating decrease elsewhere – this phenomenon is known as ‘superchirality’. A plane wave cannot be superchiral – the maximum chirality it can have is that of CPL – but superchiral fields have been shown to arise from structures with planar or 3-dimensional chirality, similar to the enhancement of the electric nearfields in plasmonic structures.[61,62]

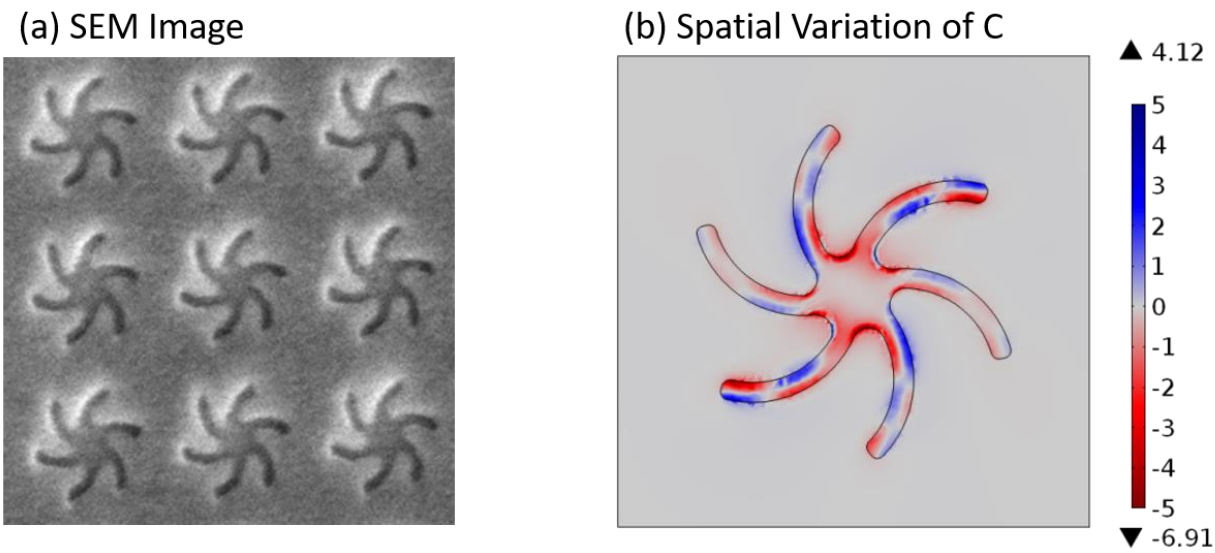

Figure 1.4. Chiral Metamaterials Show Locally Increased Optical Chirality. (a) A scanning electron microscope (SEM) image of a periodic array of gold shuriken nanostructures, that are composed of a shuriken shaped hole indented into a gold film with an identically shaped solid structure beneath it. (b) An electromagnetic simulation of the array in (a) illuminated by linearly polarised incident light (performed using COMSOL) yields a map of the spatially varying optical chirality density, showing in certain areas it can increase well above 1, the value for CPL. This C map is in the xy-plane and is measured at the top surface of the solid structure at about 700 nm incident light wavelength.

An example is shown in **figure 1.4** of an array of 'shuriken' shaped gold nanostructures illuminated with linearly polarised light, demonstrating that the spatially varying chiral field can locally have a C value greater than 1 after being normalised by the equivalent value for CPL in air.

It has been demonstrated in recent years that spectroscopies involving chiral light-matter interactions can be enhanced in sensitivity by superchiral fields, in a similar vein to plasmonic fields enhancing, for example, Raman spectroscopy.[63,64,65] This includes enhancements to the signal in CD spectroscopy when the sample is within the chiral nearfield. This enhancement is a desired effect because the CD signal is commonly weak, owing to the difference in scale between the wavelength of light and size of the molecules to be detected.[56,66–68] The platforms that produce these superchiral fields are broad in their variety, and can include assemblies of nanoparticles, chiral nanostructures and chiral metamaterials to name a few.[69–71] The chiral structures used in this work take the form of planar chiral metamaterials deposited on templated polycarbonate substrates. In chapters 3 and 4 plasmonic

metamaterials fabricated with thin films of gold are used to study chiral interactions using reflectivity, whereas dielectric metamaterials formed from europium (III) oxide (Eu_2O_3) are used in chapters 5 and 6 for luminescence spectroscopy as Eu^{3+} emits in the visible region of the electromagnetic spectrum.

THEORY PART 2 – LUMINESCENCE SPECTROSCOPY OF EUROPIUM (III) COMPOUNDS

The second part of this thesis will involve the study of the effect of chiral fields on an inorganic metamaterial – Eu_2O_3 – using luminescence spectroscopy as a probe for structural change. As such, in this section the theoretical background relevant to results in chapters 5 and 6 will be discussed.

LUMINESCENCE SPECTROSCOPY

Luminescence spectroscopy is a highly sensitive technique useful for analysing inorganic, organic and biological molecules and structures. Phenomena such as fluorescence, phosphorescence, and bioluminescence are all forms of luminescence, providing information on the structure, identity and energies of the emitting molecules. Bioluminescence is the emission of light as a result of chemical reaction in living organisms such as some species of cephalopod.[72] Fluorescence and phosphorescence are both forms of photoluminescence, the process by which atoms first absorb light exciting their electrons to higher energy levels, and then emit light when the electrons relax down to lower energy levels again. One distinction between fluorescence and phosphorescence can be found in their respective lifetimes, as fluorescence typically occurs on a much shorter timescale than phosphorescence. . In addition, for fluorescence the emission results from an excited singlet state relaxing to the ground singlet state (a singlet is an electronic configuration in which the total spin is 0 and its spin multiplicity is 1). For phosphorescence, a triplet state (S = 1, multiplicity = 3) can be achieved by inter-system crossing from the excited singlet state, and then decays from the triplet down to the singlet ground state emitting light. The singlet-singlet transition is spin allowed (as $\Delta S = 0$) but the triplet-singlet transition is forbidden, and so is much less likely to occur and has a lower rate.[73]

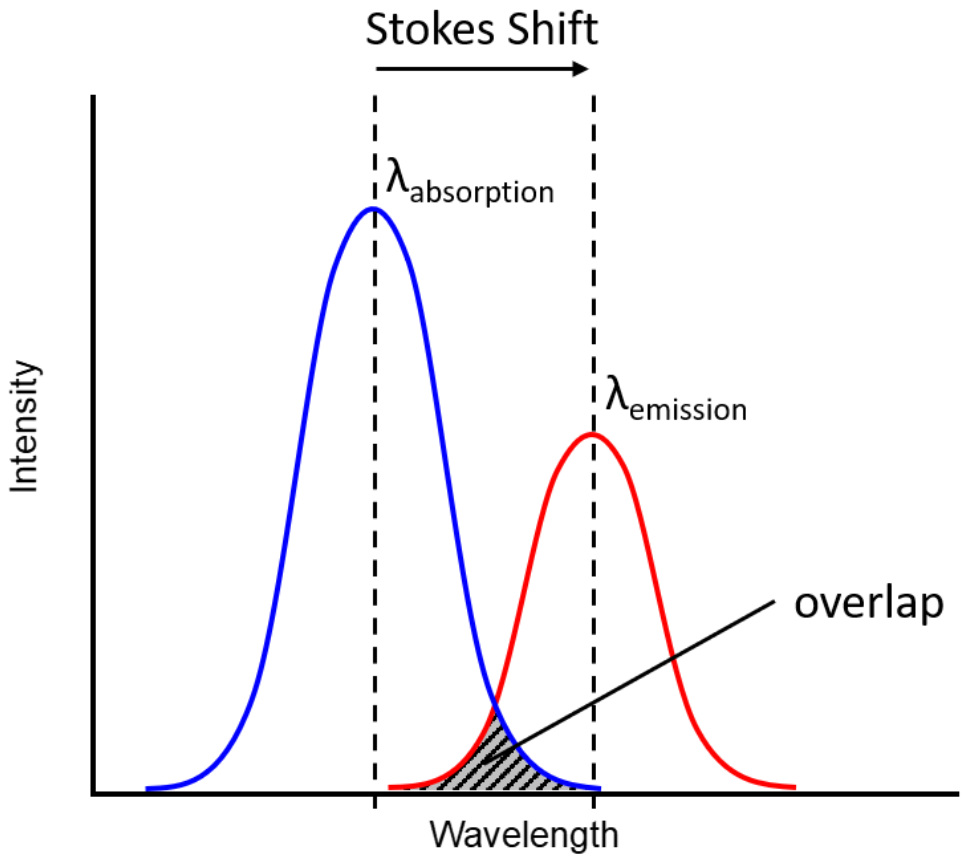

Figure 1.5. Photoluminescence Absorption and Emission Spectra. The absorption spectrum (blue) overlaps with the emission spectrum (red) if the Stokes shift is below a certain threshold. This overlap can be removed by the addition of a filter or dichroic mirror.

Once the luminescent material has absorbed energy from the excitation beam, there will be some non-radiative relaxation processes reducing its vibrational energy down to the ground state for the excited electronic energy level – vibrations and heat transferred to surrounding material without light being emitted. What this is means is that the energy absorbed in the excitation will be greater than that involved in the emission transition, and so the emitted light will have a longer wavelength than the incident light; this red-shift from absorption to emission is called the Stokes shift. This is shown in **figure 1.5**. There can however still be overlap between the higher wavelength end of the absorption spectrum and the lower end of the emission, which can be a problem as this may result in the intense excitation beam masking the weaker emissions from the material. In these cases, it is necessary to make use of a dichroic mirror or filter chosen to operate at the appropriate wavelength to block the incident light from being detected.

EUROPIUM PHOTOLUMINESCENCE

Lanthanides (also known as the rare earth elements) are a series of 15 elements in the f-block of the periodic table, and are so-called because they share some chemical properties with Lanthanum, atomic number 57. The 4f electron shell is filled going across this series and as such much of their chemistry involves these f-electrons. The 3+ ions of some of the lanthanides, notably samarium, terbium, dysprosium and europium exhibit strong luminescence. In particular, Eu^{3+} has a strong series of emissions in the red part of the visible spectrum that are known to be sensitive to their chemical environment, making it a useful probe for structural or chemical changes in a material.[74–76] Europium (III) will hence be the focus here, with the intention to study its luminescence when in the form of europium sesquioxide (Eu_2O_3) in later chapters.

In europium (III) the photoluminescence arises from f-f transitions (electron transfer from one f orbital to another) in the ion. It would ordinarily be assumed that the f-f transitions would be forbidden owing to the Laporte selection rule, which states that there must be a change of parity (from odd to even or even to odd) for a transition to occur in a centrosymmetric atom; f-orbitals are parity-odd and f-f transitions conserve parity.[77] The parity transformation is even if an orbital is unchanged under the inversion operation and odd if it changes sign under inversion. However, if the europium ion is contained within a ligand field, it is able to undergo processes such as spin-orbit coupling resulting in degenerate atomic states becoming non-degenerate molecular states, thus relaxing the selection rules and allowing classically forbidden transitions to become observable. The result is that what was, in isolated europium, a 4f-4f transition is now a $^5D_0 \rightarrow {}^7F_J$ transition in the emission spectrum, where J is the total angular momentum quantum number taking into account the coupling of spin angular momentum S and orbital angular momentum L.

Changes of electronic energy in an atom can be described by a Jablonski diagram (**figure 1.6**), which includes fluorescence, phosphorescence and other processes including those that are non-radiative, i.e., do not involve the emission of light. Europium (III) compounds absorb strongly in the near-UV and blue visible regions of the electromagnetic spectrum, exciting it to the ^5D_k excited states, where k = 0-4, or the $^5L_6$ excited state.[78]

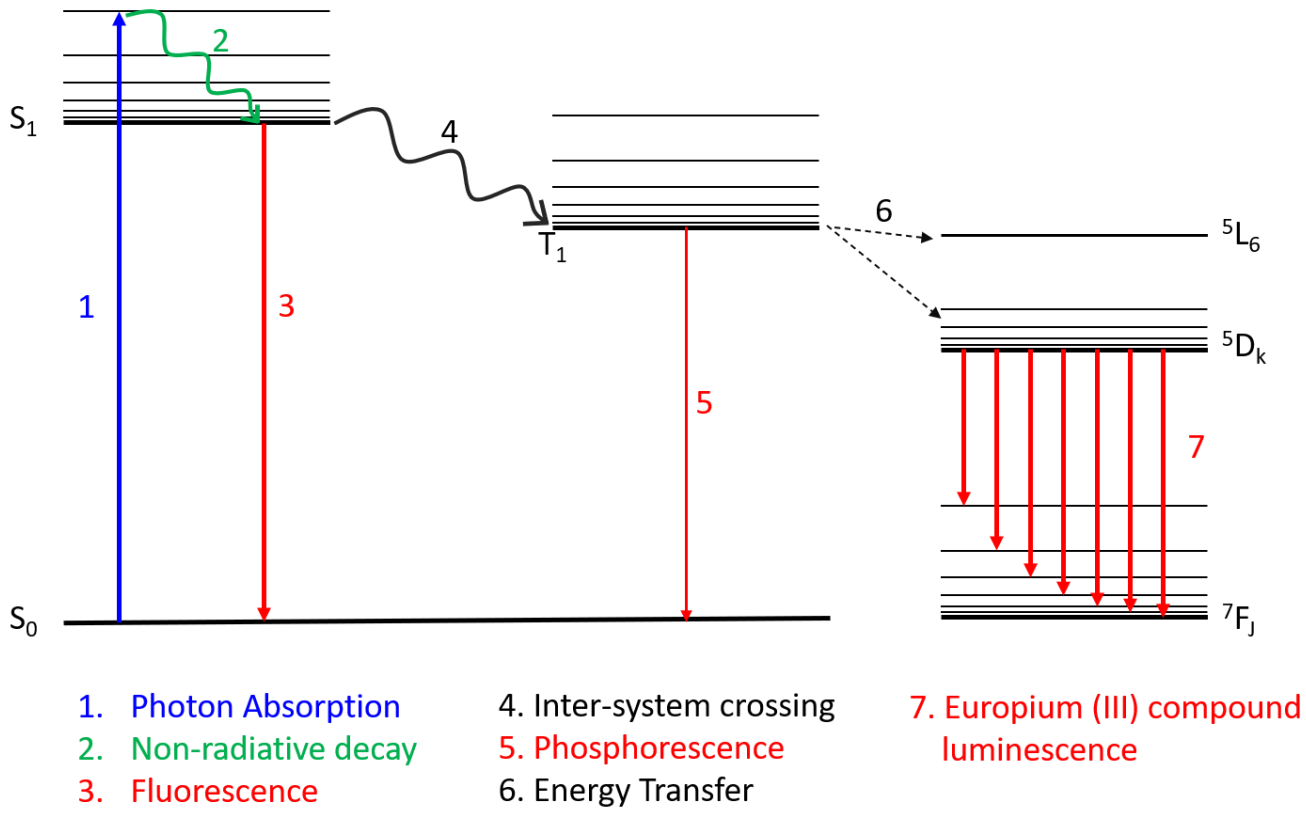

Figure 1.6. Jablonski Diagram for Europium (III) compounds. Excitation by photon absorption can occur directly in the Eu^{3+} ion or its surrounding ligands, and then transferred to the ion. S_0 and S_1 refer to the ground and first excited singlet states, and T_1 to a triplet state. Decay by fluorescence is a fast process as it is spin-allowed, but much slower by phosphorescence as it is classically forbidden. Non-radiative decay can include, for example, vibrational decay as phonons or heat in the surrounding material.

In addition, excitation in europium (III) compounds can arise from energy transfer processes from the attached ligands to excited states in the Eu^{3+} ion.[79] After non-radiative decay processes (such as vibrational energy being transferred as phonons, or heat) the emissions observed in the visible region are a result of the $^5D_0 \rightarrow {}^7F_J$ transition series, where J = 0 – 6. The selection rules for europium (III) luminescence are found from Judd-Ofelt theory – named for B. R. Judd and G. S. Ofelt. In the 1960s they assigned selection rules to the transitions in lanthanides to understand their relative abundancies, and wrote about the transition probabilities and dipole strengths for lanthanide ions, allowing for the form of the emission spectra from compounds of these ions to be predicted.[80–82]

The dipole strength *D* provides an expression for the intensities of the transitions in Eu^{3+} compounds, and can be calculated from absorption spectra. The method of calculation of dipole strength depends on whether the transition takes on electric

dipole character (requiring a change of parity from odd to even or even to odd) or magnetic dipole character (in which parity can be conserved). For magnetic dipole transitions, the dipole strength can be calculated using the wavefunction for the 4f free-ion, so the magnetic dipole strength D_{MD} of the $^5D_0 \rightarrow {}^7F_1$ transition can be directly determined to be 9.6×10^{-6} Debye^2, and is 0 for the other transitions.[83]

For electric dipole transitions, to calculate the dipole strength D_{ED} the Judd-Ofelt parameters Ω_λ must be used, where $\lambda = 2,4,6$, with the equation

$$D_{ED} = e^2 \sum_{\lambda=2,4,6} \Omega_\lambda \left|\langle J \| U^{(\lambda)} \| J' \rangle\right|^2 \qquad [1.30]$$

where e is the elementary charge, and the factors $\langle J \| U^{(\lambda)} \| J' \rangle$ are the reduced matrix elements of the dipole operator for these emissions.

The values of the square matrix elements used in calculating the dipole strength for the $^5D_0 \rightarrow {}^7F_2$, $^5D_0 \rightarrow {}^7F_4$ and $^5D_0 \rightarrow {}^7F_6$ transitions are shown in **table 1-1**.[84] The values of D_{MD} and D_{ED} for the remaining three transitions $^5D_0 \rightarrow {}^7F_0$, $^5D_0 \rightarrow {}^7F_3$ and $^5D_0 \rightarrow {}^7F_5$ are all zero. This follows from the Judd-Ofelt selection rules, which state that for an electric dipole transition (either absorption or emission) to occur in a lanthanide compound $\Delta J = 2,4,6$ if the initial or final state has $J = 0$ and $\Delta L \leq 6$. In addition, the selection rules state that for magnetic dipole transitions $\Delta L = 0$ and $\Delta J = 0, \pm 1$ only but a $J = 0 \rightarrow 0$ transition is forbidden. For both electric and magnetic dipole transition $\Delta S = 0$.

The Judd-Ofelt parameters used in the calculation of the electric dipole strength can be calculated using **equation 1.31** from experimental data. From experiment the intensity I_λ of the transition $^5D_0 \rightarrow {}^7F_\lambda$ occurring at average wavenumber $\tilde{\nu}_\lambda$ and intensity I_1 of $^5D_0 \rightarrow {}^7F_1$ at average wavenumber $\tilde{\nu}_1$ can be found in a medium with refractive index n.

$$\Omega_\lambda = \frac{D_{MD}\tilde{\nu}_1^3}{e^2\tilde{\nu}_\lambda^3 |\langle J \| U^{(\lambda)} \| J' \rangle|^2} \frac{9n^3}{n(n^2+2)^2} \frac{\int I_\lambda d\tilde{\nu}}{\int I_1 d\tilde{\nu}} \qquad [1.31]$$

The factor $9n^3/n(n^2+2)^2$ in this equation accounts for corrections due to dipole-dipole interactions. With the Judd-Ofelt parameters and the dipole strengths now

calculated, the spontaneous emission probability *A* of the transition from state ΨJ to state $\Psi' J'$ that emits at average wavenumber $\tilde{\nu}$ can be determined from

$$A(\Psi J, \Psi' J') = \frac{64\pi^4 \tilde{\nu}^3}{3h(2J+1)} \left(\frac{n(n^2+2)^2}{9} D_{ED} + n^3 D_{MD} \right) \quad [1.32]$$

where h is Planck's constant. If the Judd-Ofelt parameters for absorption have been determined experimentally, then the expected luminescence intensities can be predicted by using **equation 1.32** to calculate branching ratios.[85]

TABLE 1-1. SQUARE REDUCED MATRIX ELEMENTS OF THE ELECTRIC DIPOLE USED FOR CACLULATING DIPOLE STRENGTH

Transition	$\lvert\langle J \Vert U^{(2)} \Vert J' \rangle\rvert^2$	$\lvert\langle J \Vert U^{(4)} \Vert J' \rangle\rvert^2$	$\lvert\langle J \Vert U^{(6)} \Vert J' \rangle\rvert^2$
$^5D_0 \rightarrow {}^7F_2$	0.0032	0.0	0.0
$^5D_0 \rightarrow {}^7F_4$	0.0	0.0023	0.0
$^5D_0 \rightarrow {}^7F_6$	0.0	0.0	0.0002

Eu_2O_3 Emission Spectra

The exact nature of the emission spectrum for europium (III) compounds depends on the identity and symmetry of the surrounding ligands and crystal structure, as Eu^{3+} is highly sensitive to its environment. The sensitivity of each transition to the local environment is recorded in **table 1-2** along with the wavelengths at which each emission peak is observed.[83] Crucial to note from this table is that the $^7F_2$, uniquely among these emission peaks, is hypersensitive. This term is comparative and denotes this transition as being much more sensitive to its environment that the others, potentially by several orders of magnitude.[86] They belong to a set of transitions present for lanthanides that are formally allowed known as quasiquadrupolar transitions, that take the same selection rules as those for quadrupoles ($\Delta S = 0, |\Delta J| \leq 2, |\Delta L| \leq 2$), albeit with much higher emission intensities. This observation is not entirely explained by the Judd-Ofelt model, and so a covalency model that explains the intensity of the hypersensitive transitions as a consequence of charge transfer mixing from its ligands has previously been established.[87]

TABLE 1-2. EMISSION BANDS OF Eu^{3+} FOR THE $^5D_0 \rightarrow {}^7F_J$ TRANSITIONS AND THEIR DIPOLE CHARACTER (ED REFERS TO ELECTRIC DIPOLE, MD TO MAGNETIC DIPOLE). THE RELATIVE STRENGTH OF THE EMISSION PEAKS CAN VARY ACCORDING TO THEIR SENSITIVITY TO THE LOCAL CO-ORDINATION ENVIRONMENT.

Transition	Wavelength	Dipole	Sensitivity to Environment
$^5D_0 \rightarrow {}^7F_0$	570nm - 585nm	ED	Observed only for certain symmetries
$^5D_0 \rightarrow {}^7F_1$	585nm – 605nm	MD	Independent of local co-ordination geometry
$^5D_0 \rightarrow {}^7F_2$	605nm – 640nm	ED	Strongly dependent on local co-ordination geometry - hypersensitive
$^5D_0 \rightarrow {}^7F_3$	645nm – 665nm	ED	Forbidden transition
$^5D_0 \rightarrow {}^7F_4$	680nm – 710nm	ED	Dependent on local co-ordination geometry - not hypersensitive
$^5D_0 \rightarrow {}^7F_5$	740nm – 770nm	ED	Forbidden Transition
$^5D_0 \rightarrow {}^7F_6$	810nm – 840nm	ED	Rarely Observed, dependent on local co-ordination geometry - not hypersensitive

The charge transfer is highly dependent on the ligand environment and the lanthanide ion, providing some explanation for the sensitivity of the quasiquadrupolar transition. In fact, the hypersensitive transition of Eu^{3+} is much stronger than those for other lanthanide compounds. As such, the luminescence spectra for Eu^{3+} can be used to characterise the local geometry and potentially structural changes of europium containing compounds such as Eu_2O_3. The hypersensitive peak will therefore be the one most closely examined in this work, given its high sensitivity.

The Judd-Ofelt selection rules discussed previously state that the $^5D_0 \rightarrow {}^7F_0$, $^5D_0 \rightarrow {}^7F_3$ and $^5D_0 \rightarrow {}^7F_5$ electric dipole transitions are forbidden, as they do not obey $\Delta J = 2,4,6$. As mentioned in table 1-2, the $^5D_0 \rightarrow {}^7F_0$ does become allowed for certain symmetry environments of the Eu^{3+} ion but the $^5D_0 \rightarrow {}^7F_3$ and $^5D_0 \rightarrow {}^7F_5$ remain forbidden. However, an example luminescence spectrum of a Eu_2O_3 thin film deposited on a polycarbonate substrate is shown in **figure 1.7**, and it is clear that some of these emission bands are detected albeit weakly compared to other transitions. Note that the $^5D_0 \rightarrow {}^7F_5$ and $^5D_0 \rightarrow {}^7F_6$ transitions are not observed perhaps due to equipment limitations but most likely because they are generally very weak and not commonly observed. The reason that forbidden transitions can still be oberved in europium (III) compounds is thought to be J-mixing. J-mixing is a phenomenon in which the wave functions of states with different J values mix together, and so wave functions with overlapping symmetry can mix when in a crystal field, particularly when the J levels are close in energy.[88]

Effectively one transition can 'borrow' intensity from another, which is why the $^5D_0 \rightarrow {}^7F_0$ and $^5D_0 \rightarrow {}^7F_3$ peaks appear in the spectrum in **figure 1.7** – the final composition of these states includes contributions from the allowed electric dipole transitions. Because of this, studies of the intensities of the emissions in europium (III) compounds are often quoted as ratios of one transition to the $^5D_0 \rightarrow {}^7F_1$ because this transition is essentially independent of its chemical environment and resists J-mixing. These comparitive intensity differences can be used as a marker for physical structure, as they vary notably in molecular europium complexes.[83]

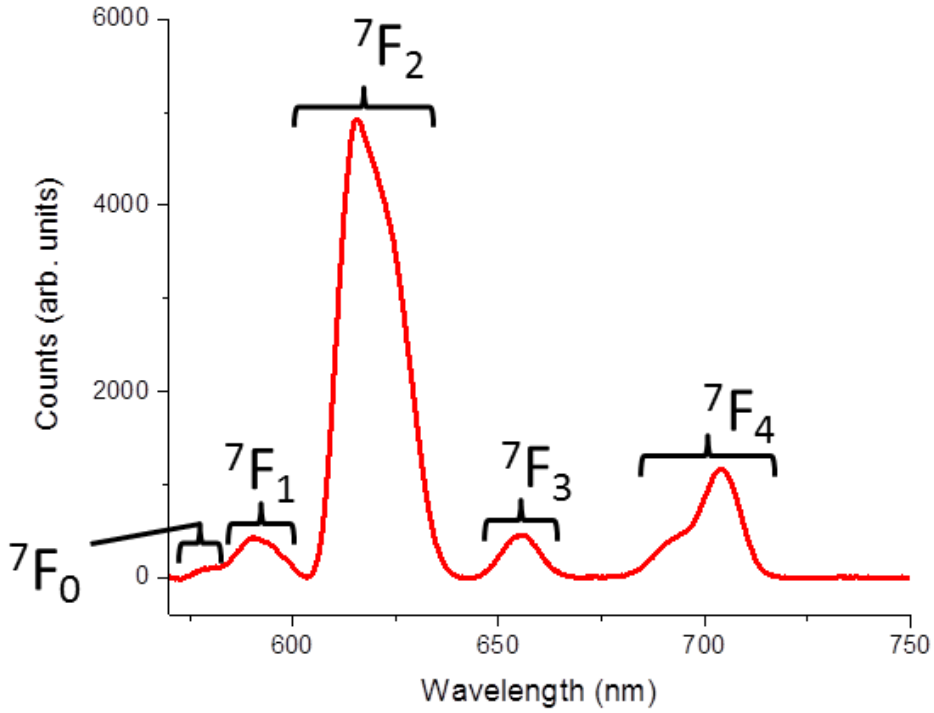

Figure 1.7. Eu^{3+} Emission Spectrum from a Thin Film of Eu_2O_3, Showing the $^5D_0 \rightarrow {}^7F_J$ Transitions. Each peak in the spectrum is labelled with the final state of its associated luminescence transition. The peaks resulting from transitions to the $^7F_5$ and $^7F_6$ states are not shown as they have not been detected.

Chapter 2 - Experimental Methods and Materials

In this chapter details will be given of the experimental setups and methods used in the following four chapters. This will include the microscopes, samples and materials used in both the chiroptical spectroscopy of gold metamaterials and luminescence spectroscopy of Eu_2O_3 films and metafilms.

Experimental Setup and Methods

Microscopes and Optical Components

Experimental work in this thesis was conducted using custom made microscopes that were built using modular components from Thorlabs, Inc. A diagram showing the standard setup used for spectroscopy of gold metamaterials is given in **figure 2.1**, along with a labelled photograph of the microscope itself. An example process by which a similar modular microscope for luminescence spectroscopy can be built and tested is described in chapter 5.

In each setup, a calcite Glan-Thomson polariser (Thorlabs) is used to change the unpolarised light entering the microscope from the source to linearly polarised light. Glan-Thomson polarisers consist of two calcite triangular prisms cemented together, allowing the s-polarised light (parallel to the cemented faces) to be transmitted through the prism and deflecting the p-polarised light (perpendicular to the cemented faces). Birefringence in the prism owing to the alignment of the calcite crystal's optical axis results in different refractive indices being experienced by the two polarisations of light, so that the p-polarised light is internally reflected at the cemented interface. A diagram illustrating this effect is given in **figure 2.2.**

The microscope in **figure 2.1** uses a tungsten halogen broadband light source (Thorlabs) whose light is carried to the microscope tubes by fibre optics before passing through a collimating lens. The light is then plane polarised in a vertical orientation by the Glan-Thomson prism before being directed down towards the sample by a 50:50 beamsplitter (Thorlabs). A 10x UPlanFLN objective lens (Olympus) with a numerical aperture of 0.3 is used to focus the light onto the sample surface. After reflection from the sample, the light passes through an analyser set in the same orientation as the input polariser and is focussed by a 30 mm focal length lens (Thorlabs) onto a second beamsplitter.

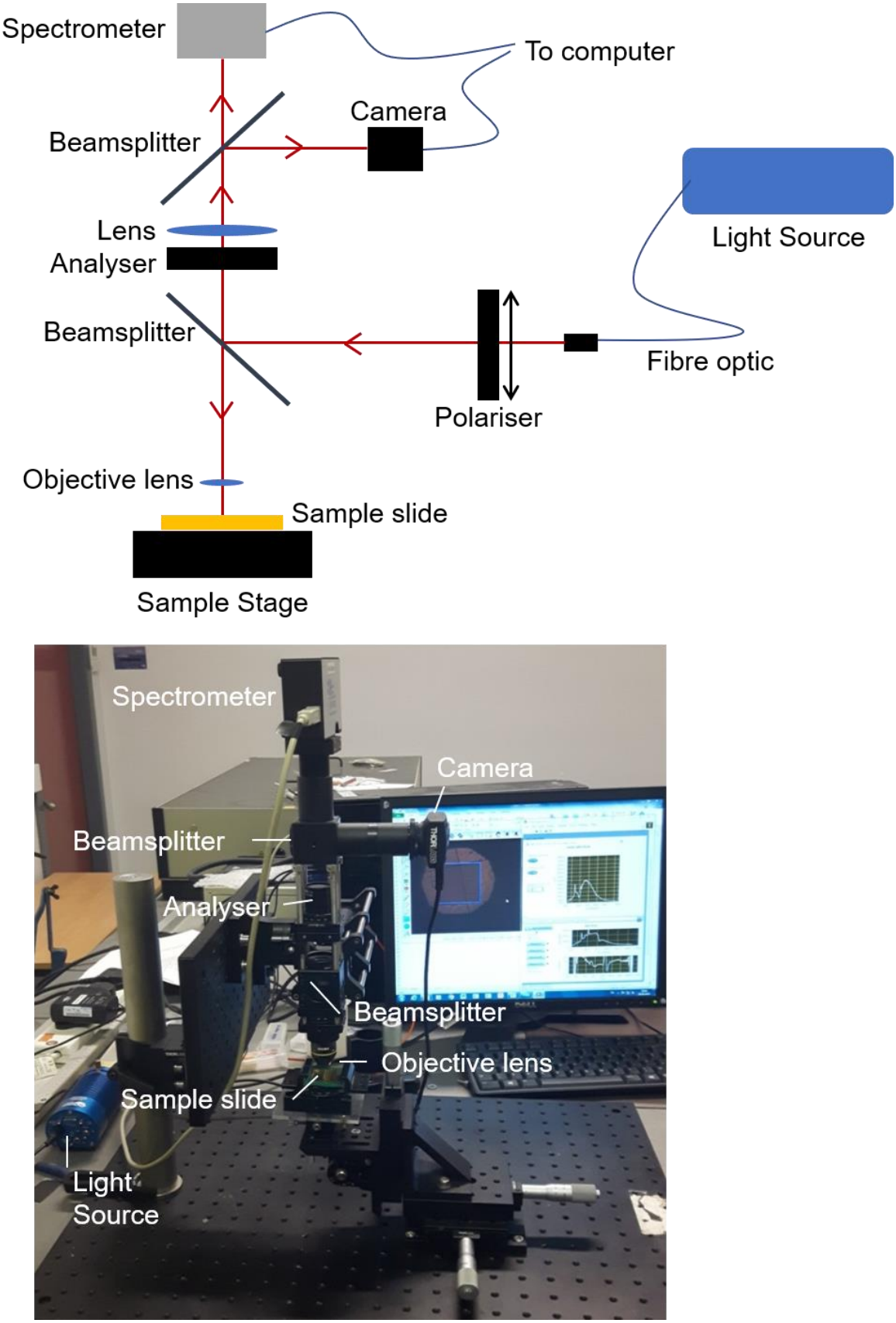

Figure 2.1. Chiroptical Spectroscopy Microscope. The top figure is a diagram of the microscope setup used to measure reflectivity and ORD from gold metamaterials. The bottom picture is a photo of the microscope with the visible parts labelled.

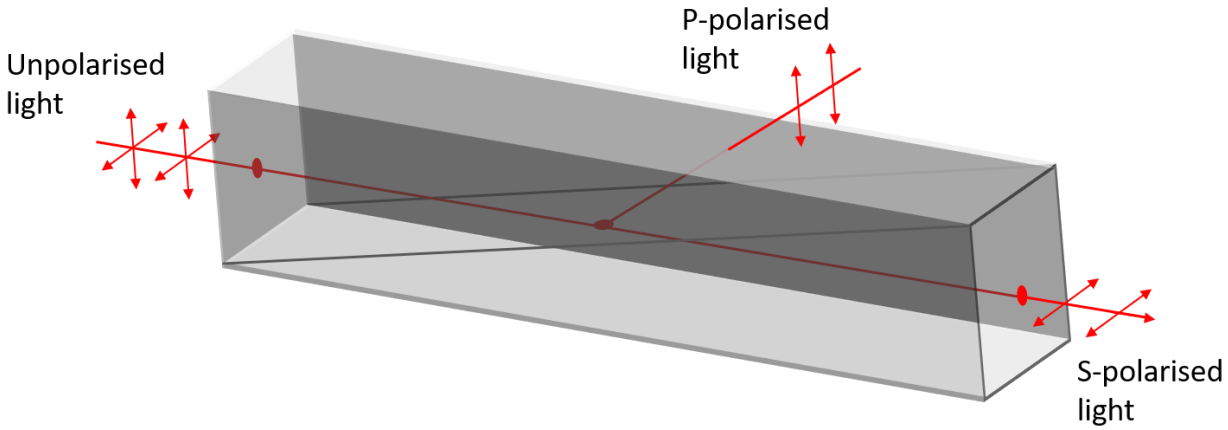

Figure 2.2. Diagram of a Glan-Thomson Polariser. Glan-Thomson polarisers consist of two triangular calcite prisms cemented together. When unpolarised light hits the surface between the prisms it reflects p-polarised light and transmits the s-polarised light as shown, so that the output from the polariser is linearly polarised light.

It splits the light between the detector and a DCC1645C optical camera (Thorlabs) whose display is viewed on the monitor to ensure that the beam is directed onto the correct array of nanostructures in the sample. The position of the beam can be controlled by moving the sample stage laterally, and the stage is moved vertically to ensure a good focus on the visual display. The light is detected by a compact USB4000 spectrometer (Ocean Optics) that has an operating spectral wavelength of 350 nm to 1000 nm.

The microscope setup used for luminescence spectroscopy in chapters 5 and 6 is similar to the one described above with some differences in components. The light source for the microscope was a 404 nm laser diode (Thorlabs) fitted to a mount that was attached directly to the microscope. The mount was connected to laser diode drivers to control the operating current and power as well as to control and stabilise its temperature. After reflection from the sample, output light was focussed into a fibre optic using a 30 mm focal length lens and detected by a Newton CCD camera (Andor) attached to a Shamrock Spectrograph (Andor). The spectrograph was fitted with a diffraction grating to give it a spectral range of 550 nm, ordinarily set at 324 nm to 874 nm. The microscope was also fitted with a longpass filter (Thorlabs) with a cut-on wavelength of 450 nm to reduce the background laser light reaching the detector.

Circularly Polarised Light and Wave Plates

In this thesis, in several cases samples are illuminated with circularly polarised light (CPL) to act as a source of chirality in the system. The light from the source is first passed through a Glan-Thomson polariser to linearly polarise it, then through an achromatic crystalline quartz quarter-wave plate (Thorlabs, Inc.) to generate CPL. Being achromatic allows these components to operate over a range of wavelengths so that chiroptical measurements with CPL can be taken over a broad spectrum.

Wave plates are made from birefringent materials, meaning that their refractive index depends on the angle at which plane polarised light is incident upon them. This means that light will travel at different speeds through the material depending on its orientation, moving fastest when aligned with its principal axis or 'fast' axis and slowest when perpendicular to the principal axis. Generally, for birefringent materials, this would result in a spatial separation of the components of light as the higher refractive index of the slow axis would cause light aligned to it to undergo more refraction and separate from its orthogonal component. However, if the material is thin enough then the difference in speeds will still result in a change of phase between the orthogonal light components effectively without them experiencing this separation, hence it is a wave plate.

A quarter wave plate, as the name suggests, will cause a phase lag of a quarter of a wave or $\pi/2$ radians for the light aligned to the slow axis compared to that aligned to the fast axis. Thus, if a plane polarised wave is incident on a quarter wave plate at a 45° angle between the two wave plate axes, such that it can be considered to have equal components experiencing through the two axes, one component will lag and result in the light becoming circularly polarised. If the wave plate is then rotated by 90° the opposite handedness of CPL will be generated. So, by affixing the quarter wave plate to a rotating mount, this enables quick manual switching between right and left CPL during an experiment. This also means if the wave plate is rotated so that the fast axis is parallel to the light polarisation axis the light will remain linearly polarised, so that measurements with all three polarisations could be made.

Substrate and Metamaterial Fabrication

The substrates used for the metamaterial samples take the form of templated polycarbonate slides the same dimensions as glass microscope slides. They are made using a plastic injection moulding machine (ENGEL) using the technique described by Gadegaard *et al*.[89] A master mould must be fabricated whose

topography is the inverse of the desired plastic template. This process was conducted using electron beam lithography with a VB6 high resolution lithography tool (Raith) and is summarised in **figure 2.3**. Firstly, a pattern for the master shim was designed using the L-Edit software from Mentor's Tanner EDA package, which was then broken down into discrete regions that will be patterned by the electron beam. A silicon wafer was prepared by spin-coating a 100 nm layer of poly(methyl methacrylate) onto it to act as a lithography resist, which was then baked for an hour at 180 ˚C to set. The resist was then exposed to the electron beam by the lithography tool, following a pattern on the surface according to the design previously defined in L-Edit. The areas of resist exposed to the beam are chemically altered and so can be removed by a 'developer', which for this resist is a 3:1 mixture of isopropyl alcohol and methyl isobutyl ketone. The resist was developed for 60 seconds, then thoroughly rinsed with isopropyl alcohol before being dried by a stream of nitrogen gas. The final master shim is then formed by electroplating the resist with nickel before the wafer is removed. By injection moulding using the nickel shim as the pattern, in which polycarbonate pellets are heated and pushed into the tool, the plastic slides can be made with the required 80 nm deep indentations in the surface. By this process, dozens of substrates can be made over the course of a few hours for a low cost, as described by Karimullah *et al*.[90]

To create the gold metamaterial samples, slides are cut using an IR laser to fit the microscope stage and fluidic cell (described in a later section) being used. These cut slides are then coated with 100nm of gold using an electron beam evaporator (Plassys), in a process that lays down the gold vaporised from the target at a rate of ~ 0.3 nm s^{-1}. The Eu_2O_3 films were deposited on the cut slides by pulsed laser deposition (Neocera Pioneer PLD) using sintered Eu_2O_3 targets (Pi Kem Ltd., UK). The deposition was performed in 50mTorr pressure of oxygen and at room temperature, and employed a 248nm KrF excimer laser (Coherent Compex Pro) in 20 ns pulses. The target was rotated during deposition to minimise the transfer of particulates to the sample.

When gold or Eu_2O_3 are deposited on the surface, they uniformly coat the substrate and fill in the shape of the indentations to form a structure constituting an "inverse" hole structure at the top and an identically-shaped solid structure at the bottom. A photograph of an example gold-coated slide is given in **figure 2.4.**

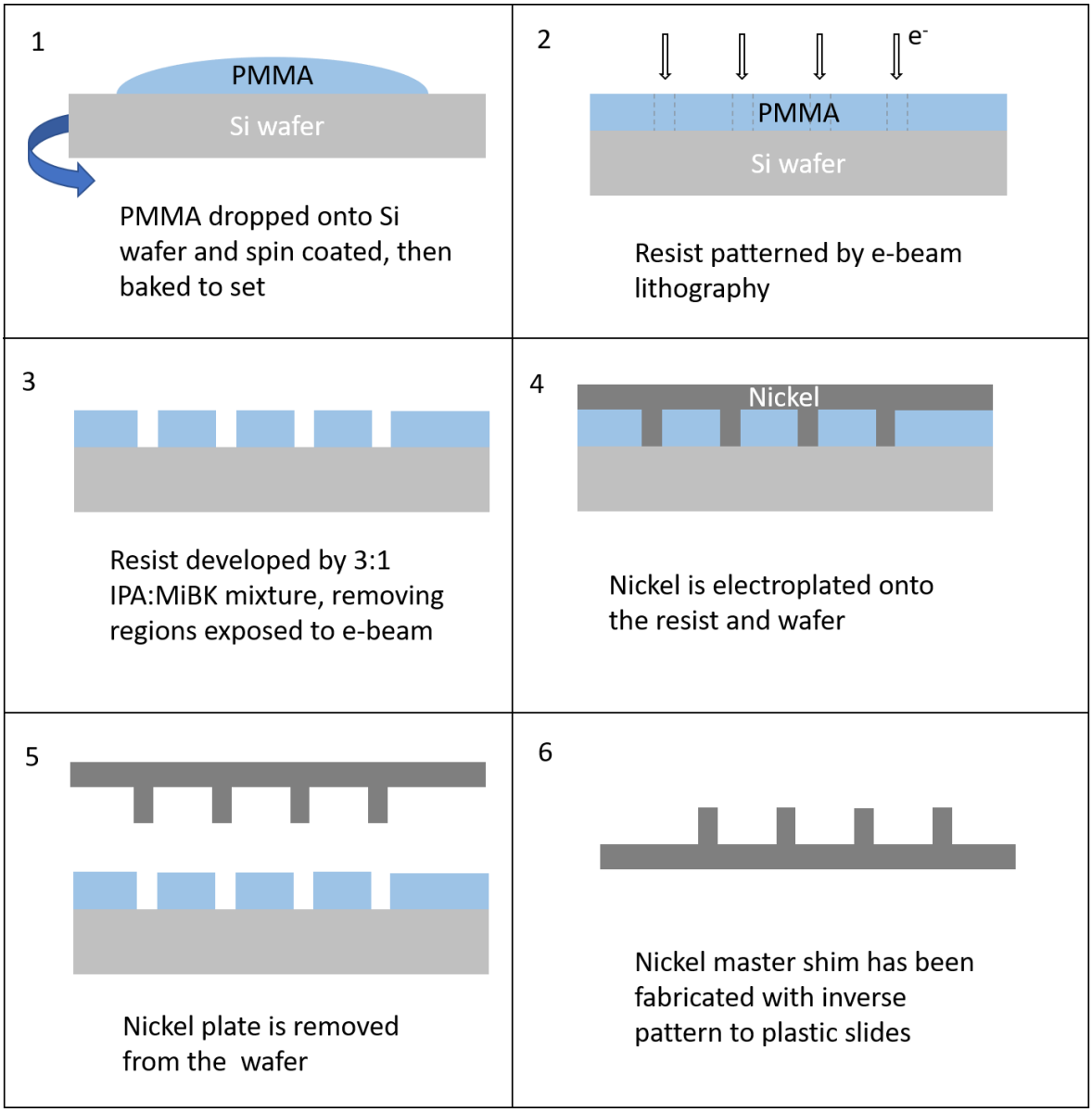

Figure 2.3. Fabrication Process for the Nickel Master Shim. This series of diagrams summarises the electron beam lithography process for fabricating the nickel shim used in injection moulding of the polycarbonate substrates. The resulting shim has the inverse topography to the desired substrates – solid structures on its surface so that the injection moulded plastic has indentations in its surface.

In addition, the Eu_2O_3 film structure was characterised by Donald MacLaren (University of Glasgow, School of Physics & Astronomy) using transmission electron microscopy, described in more detail in chapter 6. TEM was performed by depositing a ~40 nm-thick film directly onto an amorphous holey carbon film and imaged in a JEOL ARM CFEG instrument operated at 200 kV. Characterisation found the film to be amorphous, lacking diffraction features that would indicate a crystalline nature.

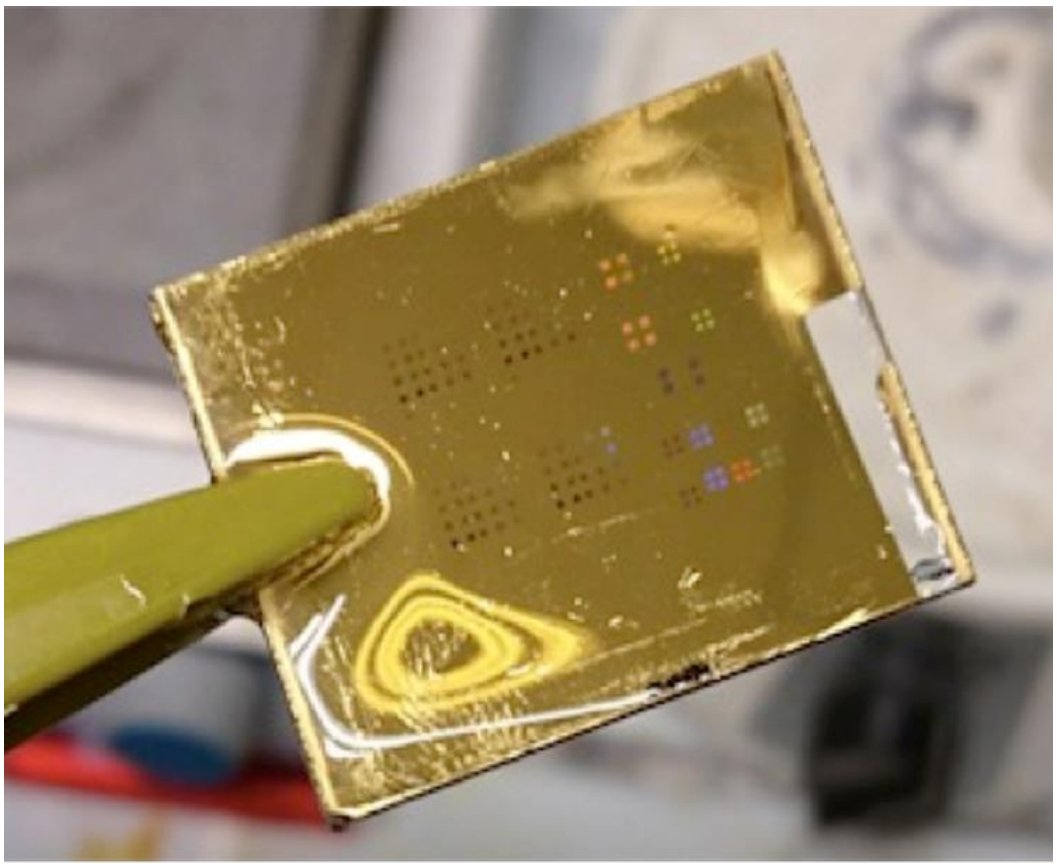

Figure 2.4. Gold Metamaterial on Polycarbonate Substrate. Photograph of an injection moulded polycarbonate slide after being cut to size and coated with 100nm of gold. The arrays of nanostructures can be seen when held up to the light. The larger sets of nanostructure arrays in the middle-left are gammadions with a variety of sizes and interstitial spacings, where the top row arrays are right-handed (RH) structures and the bottom row are left-handed (LH). The remaining structures on the right side of the sample are a variety of different structures – shuriken of various sizes and spirals for example.

CHIROPTICAL SPECTROSCOPY

In this thesis the microscope in **figure 2.1** with the broadband light source is used to perform chiroptical spectroscopy, the spectroscopic technique by which the asymmetrical responses between chiral electromagnetic fields and chiral materials can be exploited to detect, for example, the presence of or changes to chiral molecules. The majority of these experiments involve the calculation of relative reflectivity, but also the optical rotatory dispersion (ORD) is measured. The reflectivity spectrum of the gold metamaterial will exhibit a plasmonic resonance, and the spectral position, width and shape of the peak will depend on the physical properties of the structures present. In chiroptical spectroscopy, if the field around the nanostructure is chiral then the effective refractive index it will experience will

depend on the chirality of the material at its surface, leading to asymmetries in the responses of LH and RH structures. This commonly presents itself as asymmetric wavelength shifts in the spectra, a useful parameter for chiroptical ORD measurements.[63,66] However, the shift owing to refractive index is not the only parameter that exhibits asymmetries in the chiroptical response. For example, the asymmetry in the coupling between electromagnetic modes in the plasmonic equivalent of EIT will be discussed in Chapter 3.

To run reflectivity experiments, the first step was to align the sample under the microscope. The goal of the alignment process was to get the reflectivity spectra for the LH and RH structures to be identical, as without a chiral analyte on the surface there should be no difference between them. This involved an iterative process of measuring the reflectivities and comparing, adjusting the sample stage as necessary in an attempt to improve the similarity between the spectra, and ensuring the same positions on the sample were being measured using the optical camera before measuring again. Reflectivity measurements were run by use of a LabVIEW (National Instruments) program that allowed first to measure background reflected intensity from an area of plain gold surface, I_{BG}, then reflectivity of the nanostructure array, I_{NS}, giving a relative reflectivity spectrum:

$$Relative\ Reflectivity = \left(\frac{I_{NS}}{I_{BG}}\right) \quad [2.1]$$

Each spectrum presented in this work is the average of four individual relative reflectivity measurements, to reduce noise.

ORD spectra can be calculated directly according to Stokes parameters by measuring the reflectivity at different angles of polarisation relative to the input polarisation. Functionally this means taking four reflectivity spectra with the analyser at each of 0°, 45°, 90°, and 135° (135° is equivalent to -45°) with respect to the input polariser. The ORD, θ, in degrees can then be calculated from experiment by measuring the reflected light intensities I_0, I_{45}, I_{90} and I_{135} using

$$\theta(\lambda) = \frac{1}{2}\tan^{-1}\left(\frac{I_{45} - I_{135}}{I_0 - I_{90}}\right) \quad [2.2]$$

In each ORD measurement this property was calculated for the plain gold surface and the nanostructure arrays. The ORD from the plain gold was then subtracted from those of the structures to remove any background.

Many of the experiments conducted using these methods required liquid analytes to be on the sample surface, and that those liquids be removed and others added during the experiment. A fluidic cell, **figure 2.5**, was constructed to fulfil this requirement. The black plastic holder and the orange plastic cover were 3D printed components designed specifically for these experiments. To construct the fluidic cell, first the sample slide is placed in the holder with the gold film side facing up and then a piece of silicone is laid on top. The silicone must have a piece cut out from its centre, forming a window inside the cell that will sit above the nanostructure arrays being measured. This window will act as the fluidic chamber during the experiment. A glass slide is then placed on top of the silicone to hold it in place, before the plastic over is slid in over the glass, forming a tight seal. Needle tips are then pushed through holes in the sides of the plastic holder and through the silicone, into the fluidic chamber at the centre. This way, liquids can be injected onto the sample slide during the experiment. These cells were used for measurements in water, salt solutions, chlorophyll *a* solutions and α-pinene.

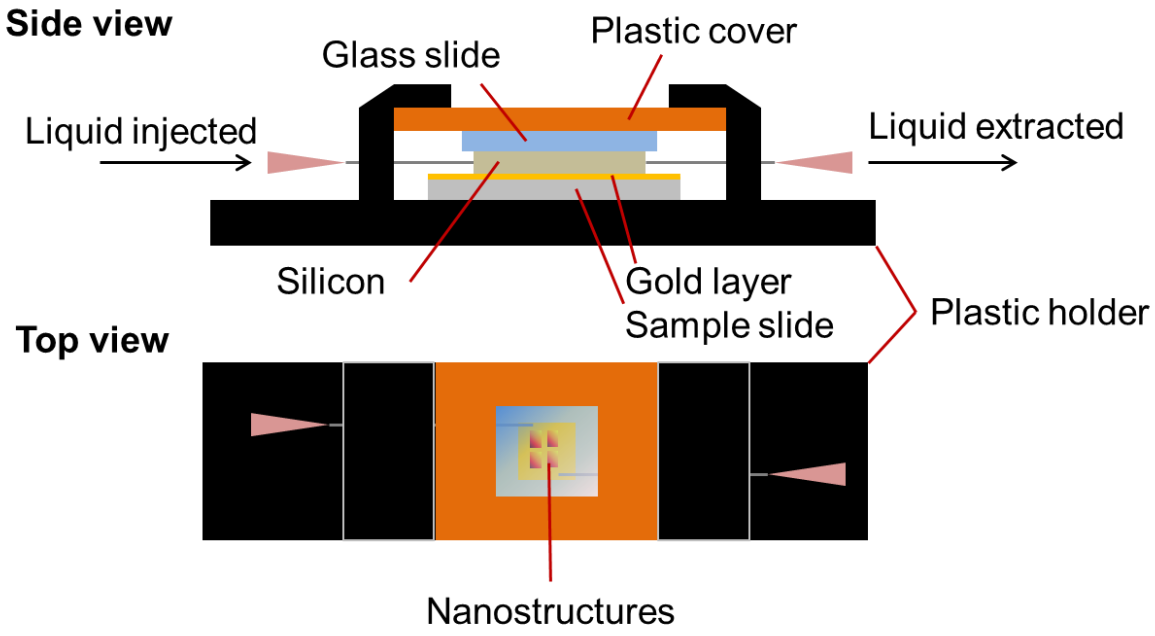

Figure 2.5. Fluidic Cell for Chiroptical Spectroscopy. These diagrams show a cross-section (top) and top-down (bottom) view of the constructed fluidic cell used to measure liquid analytes on the gold metamaterial surface. The silicone layer has a square hole cut in its centre to create a space that the liquid can be injected into. The remaining pieces (glass slide, cover and holder) are there to seal the liquid in the cell and hold the sample in place.

Luminescence Spectroscopy

In Chapters 5 and 6, Eu_2O_3 films and metafilms are studied using luminescence spectroscopy. In those experiments the 404nm laser diode was driven using a 180mA fixed current, resulting in a maximum optical power output of ~18 mW. This power was measured using a digital power meter equipped with a photodiode sensor. A cooling system was used to drop the spectrometer to around -60°C for optimum reduction in thermal noise. Before experiments, after turning on the laser, time was taken to allow the temperature to stabilise, about 30 minutes to an hour. During this time the spectrum was monitored on a continuously updating read out to ensure fluctuations in the spectrum were minimal. The optical camera in the microscope was used to ensure the beam was focussed well on the sample, and that the correct position of the metamaterial was being measured. Spectra were collected using the Solis software (Andor), with an exposure time of 0.1 s and 2400 accumulations per spectrum. This means that 2400 spectra were added together in one measurement, that could later be divided by 2400 to find an average spectrum. An electronic gain was set to 195 to improve the detected luminescence signal. For excitation with linearly polarised light, luminescence spectra were collected using a polarisation orthogonal to the input polarisation, to reduce the background laser light being detected in addition to the attenuation from the longpass filter.

Materials

Organic Molecules

(-)-α pinene and (+)-α-pinene (empirical formula $C_{10}H_{16}$, molecular weight 136.23 Da) used in chapter 3 were both purchased from Sigma Aldrich. The chemical structures are shown in **figure 2.6**. Experiments in which pinene was added to gold metamaterial surfaces, the sample slide was fixed in a fluidic cell as described in **figure 2.5.** Water was injected into the cell first, enough to fill the space in the silicon layer and cover the exposed sample surface, about 500 µl. After reflectivity measurements with water were complete, the water was extracted and the same volume of pinene was injected and measured. This process was carried out for the (-)-α pinene and (+)-α-pinene. For the racemic pinene, first 2 ml each of the two enantiomers were mixed together and stirred gently. The measurement procedure was then followed as with the chiral pinenes.

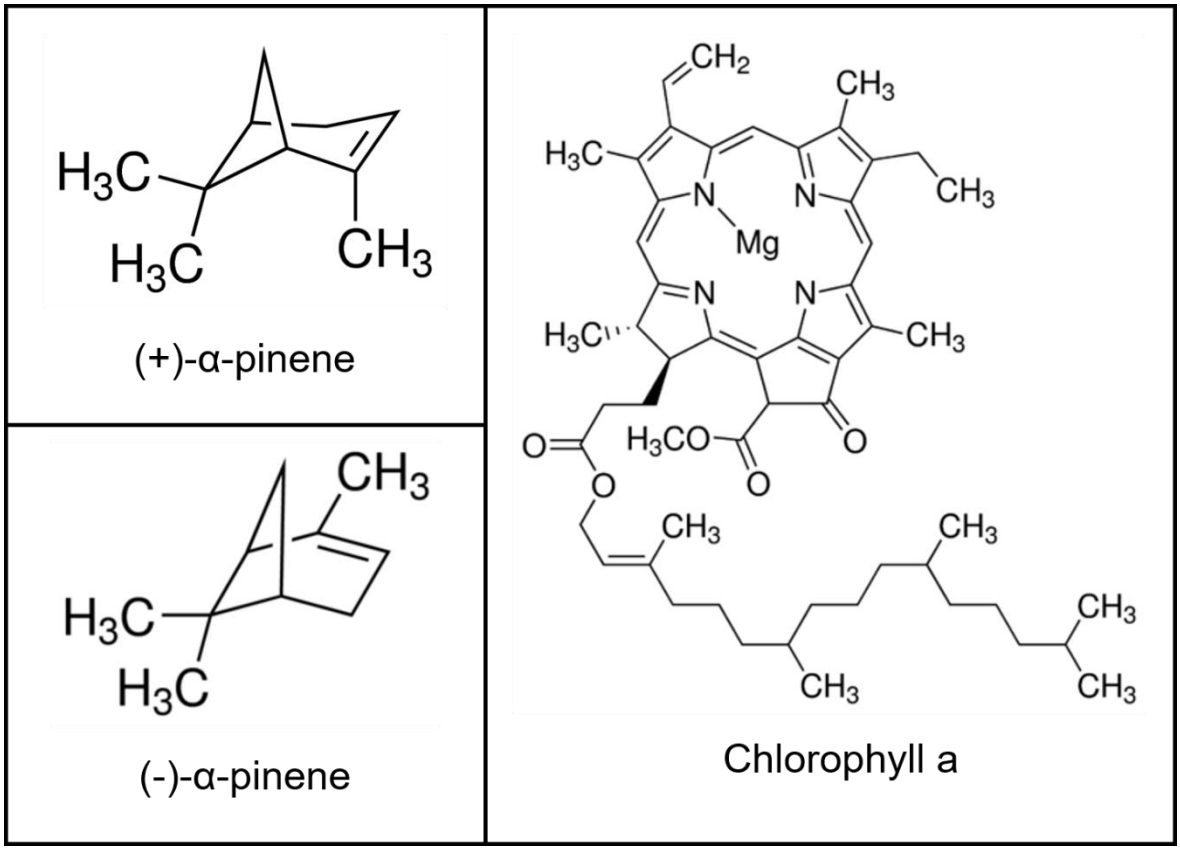

Figure 2.6. Organic Molecule Structural Formulae. Images on the left show the two enantiomers of α-pinene and on the right is chlorophyll a. All images taken from Sigma Aldrich.

Chlorophyll *a* (empirical formula $C_{55}H_{72}MgN_4O_5$, molecular weight 893.49 Da) from spinach was also purchased from Sigma Aldrich for experiments presented in chapter 3, and its structure is shown in **figure 2.6**. 1 mg of chlorophyll *a* was dissolved in ethanol to form a 10 mg ml^{-1} stock solution. Measurements with chlorophyll on the gold metamaterial surface were conducted by two different approaches.

Firstly, 10x and 100x dilutions (giving 1 mg ml^{-1} and 0.1 mg ml^{-1} solutions) of the stock were prepared in ethanol solvent. For this experiment, the sample was placed in a fluidic cell and analyte liquids were injected. Ethanol was injected and reflectivity measured, followed by the chlorophyll *a* solution. This was repeated for both concentrations of chlorophyll *a*. The second experiment involved drying chlorophyll on the gold surface. Reflectivity was first measured with 100 µl water on the surface with a microscope cover slip over the sample. The water was then dried off with a stream of nitrogen gas. To form the chlorophyll *a* layer, 1 µl of the 1 mg ml^{-1} chlorophyll a solution was dropped directly on top of the nanostructure arrays and allowed to dry out, depositing the chlorophyll onto the nanostructures in a thin layer

of around 20-50 nm. 100 µl of water was then added to the surface before having cover slip placed over the liquid and the reflectivity measured again. This second method ensured that the chlorophyll was in close contact with the structures, and within their evanescent chiral electromagnetic field.

Microscope Oil

In chapter 6, a luminescence measurement of Eu_2O_3 is conducted with microscope oil (Olympus, refractive index 1.518) on the metamaterial surface. After first taking the luminescence spectrum of the clean Eu_2O_3 surface (i.e., in air), 3 drops of the oil were added to the sample and covered with a cover slip. Luminescence of the surface with the oil could then be measured, providing a higher refractive index material than air, close to that of the polycarbonate substrate.

NTA Functionalisation and IgG

In Chapter 4, **figure 4.11**, a figure is presented showing results of measuring Immunoglobulin G (IgG) on shuriken nanostructures performed by Ryan Tullius that have been published in a paper by the author of this thesis and Ryan.[91] To enable adsorption of the IgG on the gold surface, it was first functionalised with thiolated nitrilotriacetic acid (NTA). First, the gold substrates were cleaned in an oxygen plasma asher for 20 s at 160 W before being immersed in a 95% ethanol solution and bubbled with nitrogen. A solution of thiolated NTA (Prochimia Surfaces) was then made in 95% ethanol, up to a concentration of 0.2 mM. The cleaned gold-coated samples were then placed into the thiol solution and bubbled with nitrogen gas for a further 5 minutes. Following this, the samples were left in the thiol solution to incubate overnight (~16−20 hours), during which time a self-assembled monolayer of NTA formed on the gold surface, owing to the strong thiol-gold bond.[92] The samples were then taken out of the thiol solution and rinsed with ethanol. The final step was to incubate the NTA-functionalised gold surfaces in 1 mM sodium hydroxide for 5 minutes in order to form $COO^- Na^+$ at the acid groups in the NTA. After this incubation the samples were removed and rinsed with HEPES (4-(2-hydroxyethyl)-1-piperazineethanesulfonic acid) buffered saline (pH 7.2) at concentrations of 10 mM HEPES and 150 mM NaCl in water. The samples were then rinsed with water and dried under a stream of nitrogen gas. To perform the protein measurements, IgG solutions ranging from concentrations of 0.3 mg mL^{-1} to 3 mg ml^{-1} were prepared in 10mM Tris buffer (pH 7.4). These increasing concentrations of protein solution were added consecutively to the functionalised nanostructure surface, and reflection measurements recorded for each solution.

Chapter 3 - Control of Plasmon Induced Transparency using Chiral Fields

Electromagnetically induced transparency (EIT) is a phenomenon that involves the interference of excitation pathways in atomic systems, resulting in an apparent increase in optical transparency. In this chapter the plasmonic analogue of EIT and how it can be manipulated with chiral fields will be studied using chiroptical spectroscopy. The connection between the phenomenon of EIT and Autler-Townes splitting (ATS), an effect which is similar superficially but does not involve interference, will also be examined with regards to the data collected.

In this chapter, a mathematical model will be constructed to describe the EIT-like resonances in the measured chiroptical spectra from shuriken-shaped nanostructured metamaterials. This model will then be used to quantify the effects of chiral perturbations on this system, enacted by the application of chiral (circularly polarised) light as well as the addition of chiral molecular layers to the sample surface. Some key experimental work discussed in this chapter was published by ACS Photonics in 2017 in a paper entitled “Controlling Metamaterial Transparency with Superchiral Fields”.[93]

Chiral Plasmonic Metamaterials

Choosing a Structure

In order to study the properties of chiral plasmonic metamaterials, the nanostructure shape must be chosen. Chiral nanostructures have been studied thoroughly as individual nanoparticles and assemblies[94–96] as well as metamaterial[65,66,90,97] forms, using a variety of geometries including multi-layered assemblies, planar arrangements of gammadion crosses, spirals and so on. The process described in Karimullah et al[90] in which plastic templates are created using injection moulding, was used as a high-throughput process for fabricating planar plasmonic metamaterials for this study. The diagram in **figure 3.1** demonstrates how the polycarbonate substrates are then converted into planar plasmonic metamaterials by the addition of a layer of gold to the surface. The gold layers used in this chapter are always 100 nm thick. These substrates have a variety of differently shaped indentations in their design, including the gammadion and the shuriken.

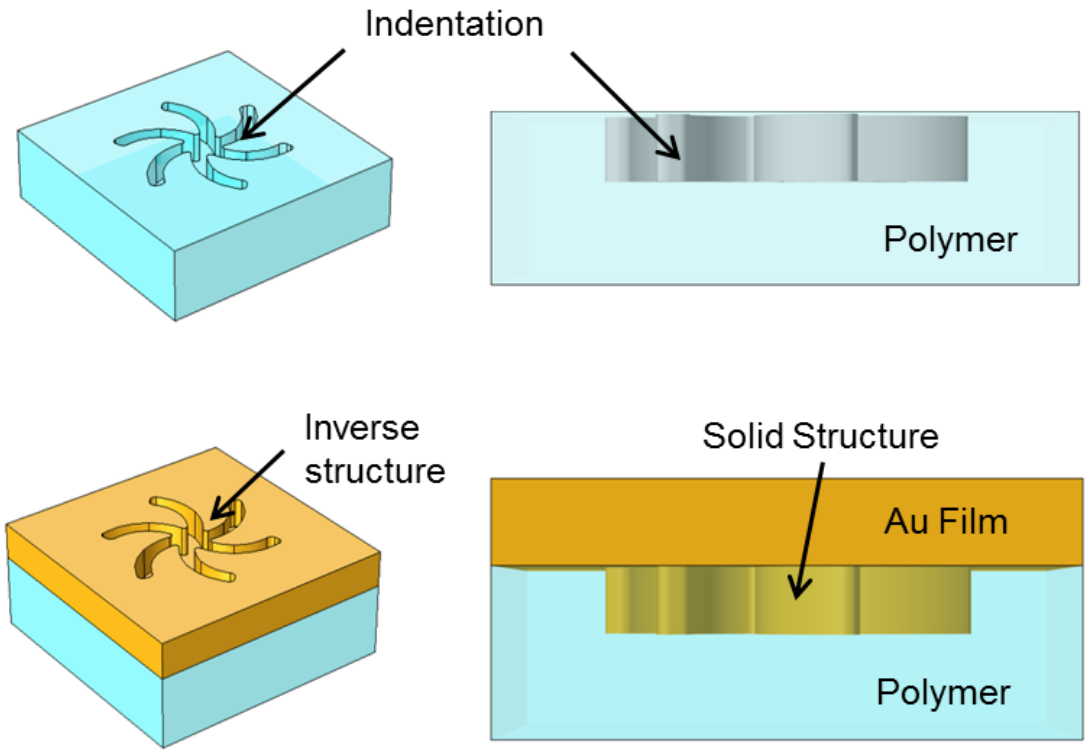

Figure 3.1. Fabrication of Plasmonic Metamaterials with Shuriken Nanostructures. Polycarbonate slides are fabricated using injection moulding over a master shim leaving the indentations in the desired shape, shown in the top row. A 100 nm layer of gold is deposited on the substrate by electron beam evaporation, forming a solid structure in the indentation and the inverse (hole) structure above it (bottom row).

Scanning electron microscope images of these two structures are shown in **figure 3.2**, in which details of their dimensions are provided.

To begin with, the shuriken structures were examined using two spectroscopy techniques – relative reflectivity and ORD. The samples were placed in an injection cell as described in chapter 2, and measured in water to simulate the conditions required for bioassays. The results of these measurements of the shuriken, for both the LH and RH structures are shown in **figure 3.3**. This finds that for this structure with 500 nm diameter and an interstitial spacing of 200 nm there appear two resonances over the measurement range possible for the light source used. In the reflectivity these resonance regions appear as reflectivity dips (absorption peaks) with a region of increased reflection at their centre. Resonances appear as bisignate shaped peaks in the ORD, in which the optical rotation reverses sign over the resonance peak.

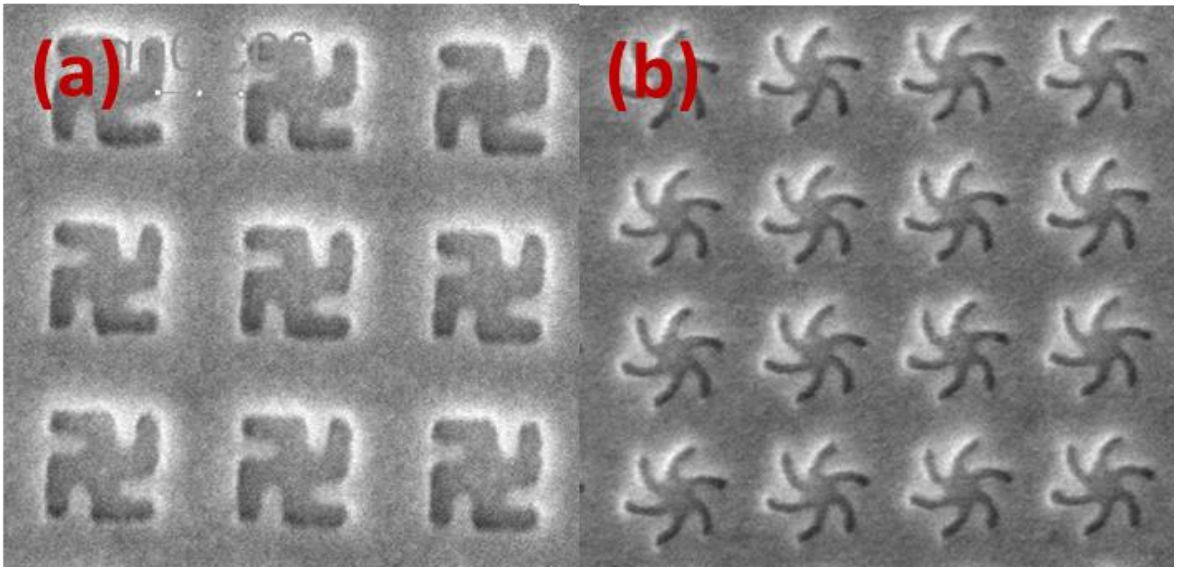

Figure 3.2. SEM Images of Chiral Metamaterials. Images of metamaterials with (a) gammadion nanostructures and (b) shuriken nanostructures taken by scanning electron microscope after gold deposition. The gammadions are 400 nm in diameter and the shuriken are 500 nm. In experiments in which linearly polarised light was used, the light would be polarised vertically along these images.

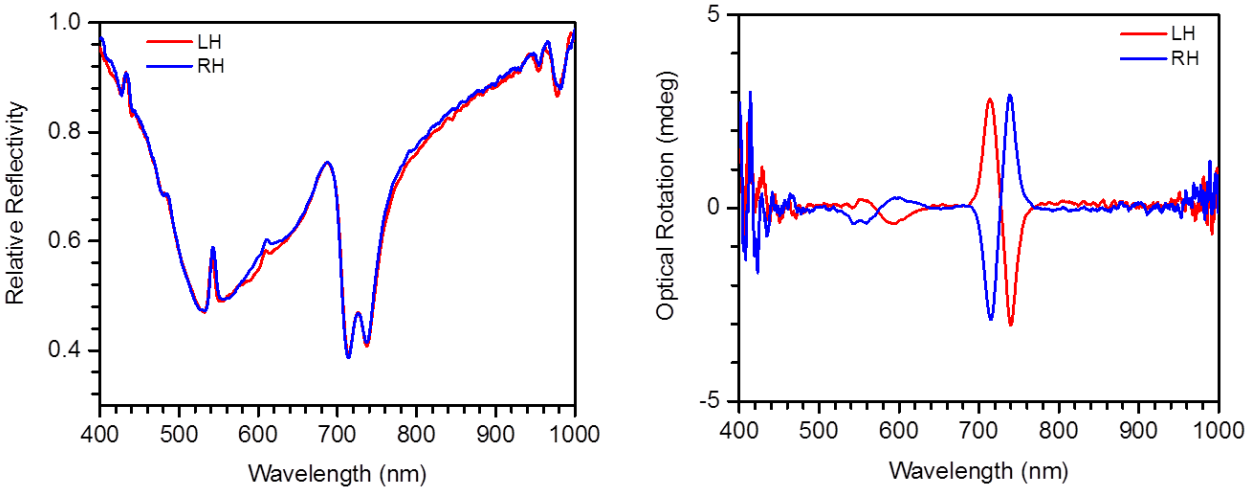

Figure 3.3. Characterisation of Shuriken Nanostructures. The relative reflectivity (left) and optical rotatory dispersion (right) are shown for the LH and RH shuriken metamaterials in water. Periodic arrays of shuriken with 500 nm diameter and 200 nm intersititial spacing were used.

Electromagnetically Induced Transparency and Autler-Townes Splitting

Phenomena Description

EIT is a quantum interference effect typically observed in atomic systems, in which two of the possible pathways for electronic excitation in a material interfere destructively. The result is that a narrow region of transparency appears within an absorption line (where ordinarily transparency is low) and has previously been leveraged to generate 'slow light', to store light and has been considered as a possible tool for cloaking in atomic vapours and solids.[98–100] The method generally used in these applications is to excite a sample with co-propagating 'probe' and 'coupling' light beams of similar frequency, allowing the coherent atomic states to couple to the light via a Raman transition. This in turn reduces the group velocity, leading to 'slow light', or the probe can smoothly be turned off to temporarily 'store' the light in the form of atomic excitations.

The observation of a transmission window within a resonance in such a system, however, is not necessarily owed to EIT. Autler-Townes splitting (ATS) involves an applied field coupling strongly to one transition in a three-level quantum system, causing that transition to split into a doublet whose constituents have similar intensity; notably ATS is not an interference effect.[101] ATS has been used for controlling spin-orbit coupling in quantum systems, measuring dipole moments and has potential for uses in quantum computing.[102,103] The absorption spectrum of a system undergoing ATS will appear visually similar to that of one experiencing EIT – two peaks with a transparency window in-between. As such distinguishing between EIT and ATS can be troublesome, and several studies have been devoted to exactly that.[98,104,105] The results of such work generally are they these can be separated according to the strength of the coupling involved – in the strong coupling regime ATS is prevalent, and EIT is observed for weak coupling – and that the Akaike Information Criterion (AIC) can be used as a tool to tell one from the other from experiment, when in the frequency domain.[104] The AIC quantifies how much information is lost when a model is fitted to experimental data, and so has previously been used to determine which of EIT and ATS was most suitable as a model for a given coupling regime.[106] A corollary of this interpretation is that an intermediate coupling regime exists, in which the coupling is equal to or only slightly higher than some threshold and the system appears to have properties indicating both EIT and ATS.[105]

An effect similar to EIT is possible in plasmonic metamaterials, in which such a transparency window arises from near-field coupling between optically bright and dark electromagnetic modes in the material.[107] In this plasmonic analogue of EIT, there may be a sharp window of increased reflectance within a strong absorption resonance (plasmon induced reflection, PIR) or increased transmission (plasmon induced transparency, PIT) i.e. a sharply decreased absorbance over a narrow region. The strength of the coupling of these modes to each other can be controlled, to an extent, with structural and geometric modifications.[108]

Mathematical model

A description of the PIR effect in a plasmonic metamaterial can be found using a coupled oscillator model, an accurate tool that can be used to mathematically replicate reflectance spectra. This model and similar methods have been documented previously, and in this work the model used will primarily be based upon that used by Tassin et al.[109,110] The two oscillators designated as $p(t)$ for the bright mode and $q(t)$ for the dark mode are described by the differential **equations 3.1** and **3.2**, and couple to one another according to complex constant $\tilde{\kappa}$:

$$\frac{1}{{\omega_r}^2}\ddot{p}(t) + \frac{\gamma_r}{\omega_r}\dot{p}(t) + p(t) = gf(t) - \tilde{\kappa}\, q(t) \qquad [3.1],$$

$$\frac{1}{{\omega_d}^2}\ddot{q}(t) + \frac{\gamma_d}{\omega_d}\dot{q}(t) + q(t) = -\tilde{\kappa}\, p(t) \qquad [3.2].$$

The two resonance modes described by these equations have central frequencies ω_r and ω_d with damping factors γ_r and γ_d. The bright mode is driven by the incident light which here is represented by an external force $f(t)$ whose coupling strength with the oscillator is described by g. This coupled oscillator model can then be modified by the inclusion of phase shifts θ and ϕ in the bright and dark mode respectively, representing retardation in the excitation process relative to the external field for these oscillators. The phase terms are included as a new addition to the model described by Tassin. These modes can represent mechanical, molecular, or electromagnetic oscillations, such that their excitation would then be understood as, for example, the displacement from the rest position, or the microscopic electric or magnetic dipole moment. The solutions of **equations 3.1** and **3.2** take the forms shown in equations **3.3** and **3.4**, and allow the coupled oscillator

to be solved in the frequency domain. The complex coupling constant $\tilde{\kappa}$ is expressed as in **equation 3.5**, depending on the coupling strength κ and the phase difference

$$p(t) = e^{-i\theta}P(\omega)e^{-i(\omega t)} \quad [3.3],$$

$$q(t) = e^{-i\phi}Q(\omega)e^{-i(\omega t)} \quad [3.4],$$

$$\tilde{\kappa} = \kappa e^{-i(\theta-\phi)} \quad [3.5],$$

where $P(\omega)$, $Q(\omega)$ and $F(\omega)$ are frequency domain equivalents of the oscillators $p(t)$, $q(t)$ and $f(t)$ respectively. Solutions [**3.3**] and [**3.4**] can then be substituted into the coupled oscillators (**equations 3.1** and **3.2**), giving:

$$P(\omega)e^{-i\theta} = \frac{gF(\omega) - \tilde{\kappa}Q(\omega)e^{-i\phi}}{D_r} \quad [3.6],$$

$$Q(\omega)e^{-i\phi} = \frac{-\tilde{\kappa}P(\omega)e^{-i\theta}}{D_d} \quad [3.7],$$

where $D_d = 1 - \left(\frac{\omega}{\omega_d}\right)^2 - i\,\gamma_d\frac{\omega}{\omega_d}$ and $D_r = 1 - \left(\frac{\omega}{\omega_r}\right)^2 - i\,\gamma_r\frac{\omega}{\omega_r}$.

Then by inserting equation 3.7 into 3.6, the following relation can be found for the electric dipole $P(\omega)$:

$$P(\omega) = \frac{g\,D_d(\omega)F(\omega)}{e^{-i\theta}(D_r(\omega)D_d(\omega) - \kappa^2 e^{-2i(\theta-\phi)})} \quad [3.8].$$

We can express the proportionality of the incident driving field and the surface electric field by the electric susceptibility of the meta-film, given by:

$$\chi(\omega) = \frac{P(\omega)}{F(\omega)} \quad [3.9].$$

Hence from **equations 3.8** and **3.9**:

$$\chi(\omega) = \frac{g\,D_d(\omega)}{e^{-i\theta}(D_r(\omega)D_d(\omega) - \kappa^2 e^{-2i(\theta-\phi)})} \quad [3.10].$$

To take into account that the metamaterial is within a metallic film, rather than separate structures on a transparent substrate, a simple effective medium approach is used by taking the average of the susceptibility of the gold, χ_{Au} and the plasmonic

metamaterial system (from **equation 3.10**).[111] Thus its refractive index n_{EIT} can be calculated:

$$\chi_{Avg}(\omega) = \frac{\chi(\omega) + \chi_{Au}}{2} \quad [3.11],$$

$$n_{EIT} = \sqrt{\chi_{Avg}(\omega) + 1} \quad [3.12].$$

From here, this model then allows us to produce reflectance spectra based on the properties of the metamaterial and n_{Sol}, the refractive index of a material on the metamaterial surface, such as a biomolecule solution or organic liquid:

$$Reflectance = \left| \left(\frac{n_{Sol} - n_{EIT}}{n_{Sol} + n_{EIT}} \right)^2 \right| \quad [3.13].$$

Process for Modelling Reflectance

In order to generate reflectance spectra using this model, values for the variables in these expressions must be found. A summary of the quantities required for a complete model are given in **table 3-1**. Values for the parameters defined by the metal used and the substance on its surface include $n_{sol} = 1.33$ (for water), $c_{gold} \approx 0.15$ and $g \approx 0.03$. The latter two parameters, c_{gold} and g are dependent on the experimental setup and properties of gold itself and only influence the background peak intensity without modifying the shape of the resonance. As such their values were set using reference data from experiment. With these in place, we can then set values for the remaining parameters such that when equation 3.13 is plotted (e.g., using Matlab), a spectrum with the recognisable EIT-like shape is produced. Then, by making small variations in each parameter in turn whilst fixing the others we can develop an understanding of how each parameter modifies the spectrum, and thus gain insight into changes in the spectrum observed in experimental results. For the remaining parameters, the effect of their variations on the reflectance spectra is shown in **Figure 3.4**, such that the differences between spectra are realistic to experimental observations**.** The resonance wavelengths ω_r and ω_d, as expected, modify the positions of the overall resonance envelope and region of increased reflection respectively, independently of one another. As such, values for these can be set directly by examination of experimental data. The damping factors

γ_r and γ_d control the plasmon extinction and PIR respectively, observed as the overall resonance and central peak intensities. Thus, the heights of the two dips and central peak can be controlled using these parameters. From there, the relative heights of the two reflectance dips can be modified with changes in θ and ϕ without any significant resonance shifts. Changes in κ affect the overall strength of the plasmon induced transparency effects, and it also increases the splitting of the two dips in reflectance. This is the final piece in enabling a complete recreation of experimental data. An example of this procedure having been applied to an experimental spectrum is given in **figure 3.5,** showing good agreement and demonstrating the usefulness of this model in comprehending the underlying physical processes in our spectroscopic measurements.

TABLE 3-1: MODEL PARAMETERS AND DESCRIPTIONS, USED TO REPRODUCE THE PLASMON INDUCED REFLECTION SPECTRA.

Parameter	Description
ω_r	Bright mode resonance frequency
ω_d	Dark mode resonance frequency
κ	Coupling strength between bright and dark modes
γ_r	Damping factor of bright mode
γ_d	Damping factor of dark mode
θ	Phase of bright mode relative to external driving field
ϕ	Phase of dark mode relative to external driving field
g	Coupling strength of external field to bright mode
n_{sol}	Refractive index of substance on metamaterial surface
c_{gold}	Multiplier accounting for Au contribution to susceptibility

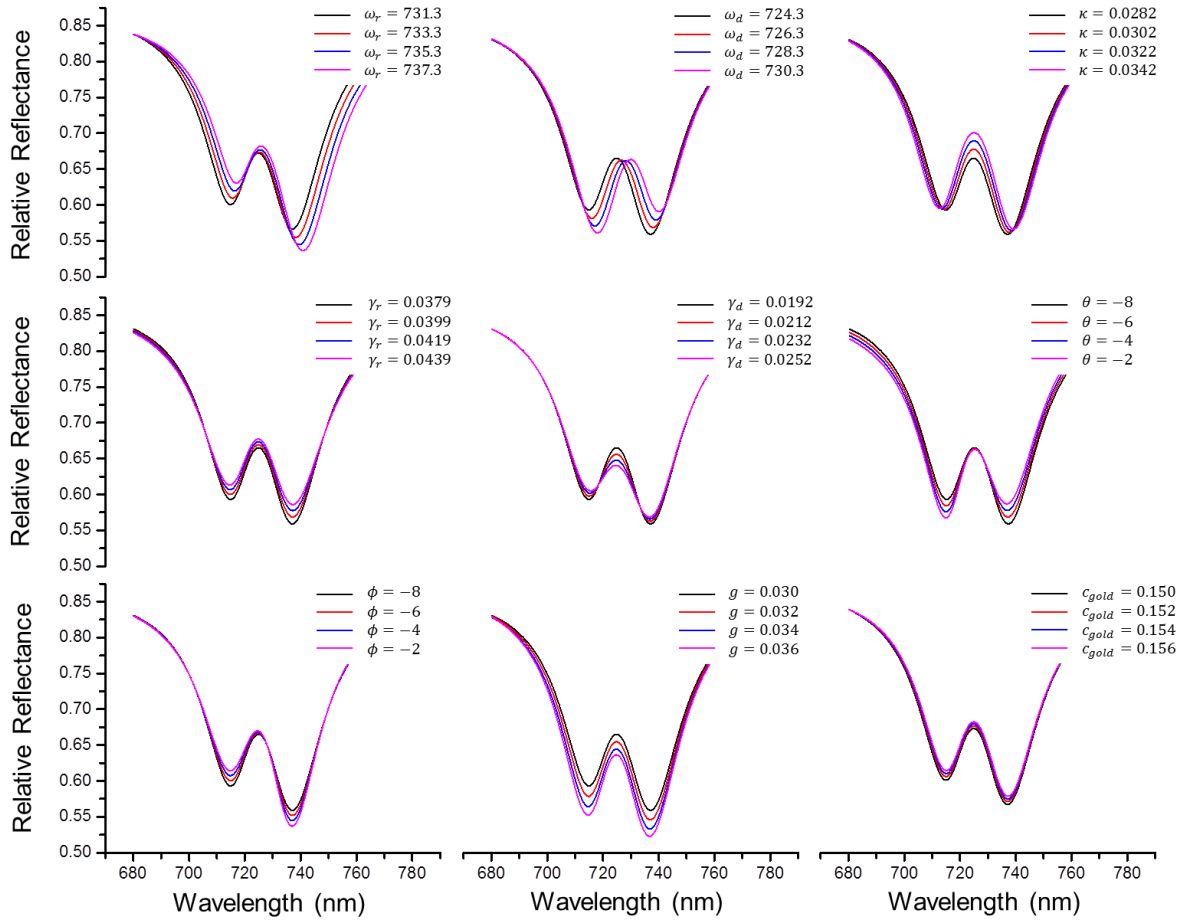

Figure 3.4. Effect of Varying Parameters in the PIR Model. Reflective reflectivity spectra were calculated from the plasmon induced reflection model and plotted using MATLAB. In each case all but one parameter was fixed whilst one was varied over four different values. The legend in each plot indicates which parameter was varied.

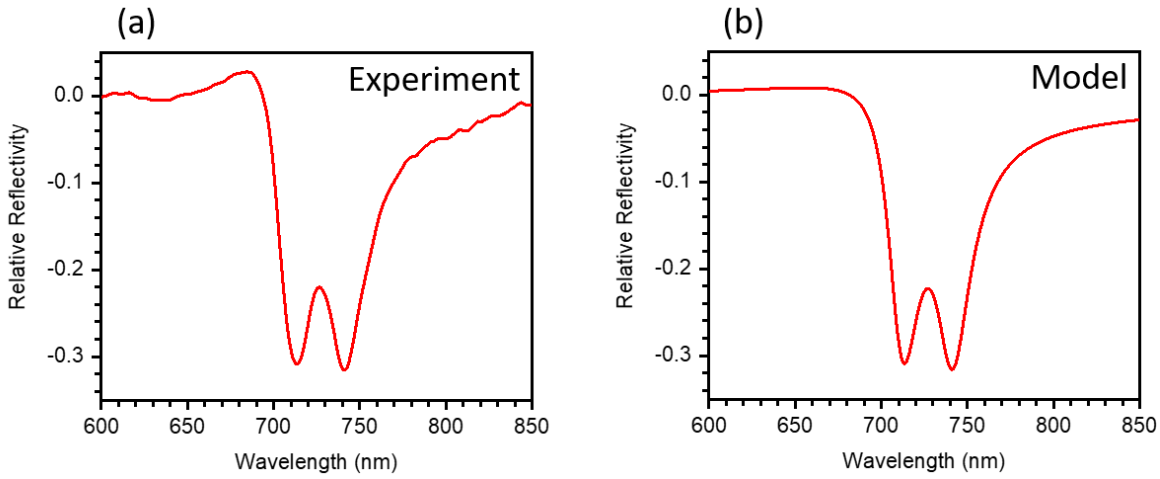

Figure 3.5. Comparison of Experimental and Modelled Reflectivity. Reflectivity spectra obtained (a) by experimental measurement with shuriken nanostructures in water and (b) by calculation with the PIR model. The model has good qualitative agreement with experiment and can replicate the resonance shape accurately.

RESULTS & DISCUSSION

With a mathematical model for the observed reflectivity established, the response of this system to the application of chiral perturbations can now be more easily understood. Illuminating the sample with circularly polarised light to establish interaction between chiral propagating light fields and the chiral electromagnetic fields at the metal surface resulting from the chiral nano structures. Based on the observations of chiral molecules in absorbing LCP and RCP to different extents, the expectation is that a chiral nanostructure will exhibit circular dichroism as well. This result has been demonstrated for a variety of chiral metamaterials.[112,113]

Equipment was set up as shown in **figure 3.6** for the reflectivity experiment similar to that in chapter 2, with the addition of a quarter wave plate (QWP) at the input. This allowed for the LPL entering from the polariser to become RCP at a +45° angle, LCP at -45° and remain linear at 0°. This convention was designated based on the setup of the rotation mount in which the QWP was contained. In an initial test, the reflectivity spectra of the LH and RH shuriken under LCP and RCP were measured and difference spectra were calculated by taking subtracting the LCP spectrum from the RCP for each structure handedness, **figure 3.7**. The sample was inserted in a cell (described in chapter 2) that was injected with water, to replicate conditions required for the biological assays that these metamaterials have been previously used for.[63,64] The difference spectra showed the expected behaviour of being equal in size but opposite in peak direction. The individual reflectivity spectra in this experiment gave a notable unexpected outcome however. It appears that in two cases – that is LH structure with LCP and RH structure with RCP – the spacing between the two reflectivity dips in the PIR spectrum appears to have increased and the central reflectivity peak is heightened.

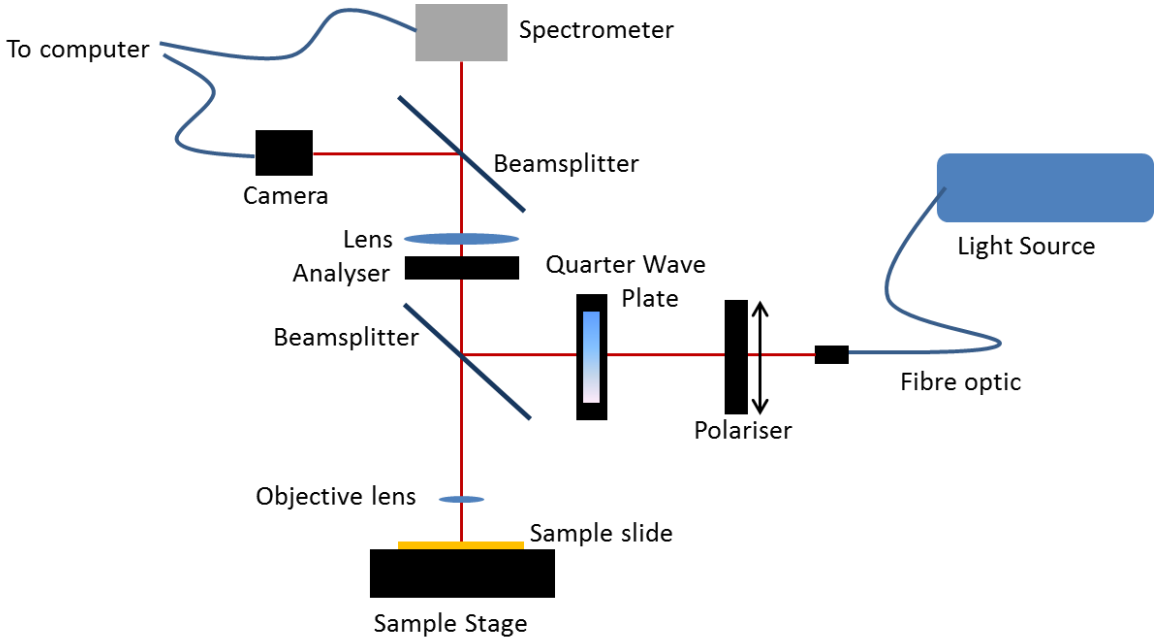

Figure 3.6. Microscope setup for CPL Experiments. This schematic is the same as for the general setup for reflectivity and ORD as shown in chapter 2, with the addition of a quarter wave plate after the input polariser. The wave-plate was attached to a rotating mount so it could be switched easily between RCP, LCP and linear light output. This modified microscope was used for the remaining measurements in this chapter.

Conversely, for the other two combinations (LH with RCP and RH with LCP) the spacing between is negligible, resolving as a shape similar to a single Fano resonance peak.[114] This observation suggests, then, that if the handedness of the chiral CPL and the chiral shuriken are 'matched', the first case with increased splitting is produced, but is reduced in the 'mis-matched' case. In order to further test this, a second set of these measurements was taken along with the corresponding reflectivity under illumination with linearly polarised light, given in **figure 3.8**. A background is subtracted from these spectra to account for the slope present in the Fano-like envelope of the resonance, seen in **figure 3.7**. Following this, the mathematical model described above was then implemented using Matlab to replicate the reflectivity spectra in **figure 3.8**. As seen before, the model is able to reproduce well the shape of the resonance, although it cannot account for slight peak at ~680 nm from the Fano character. The parameters used to do this are recorded in **table 3-2**, and so it is possible to determine the extent of the interactions between the external field, the bright mode and the dark mode of the PIR spectra.

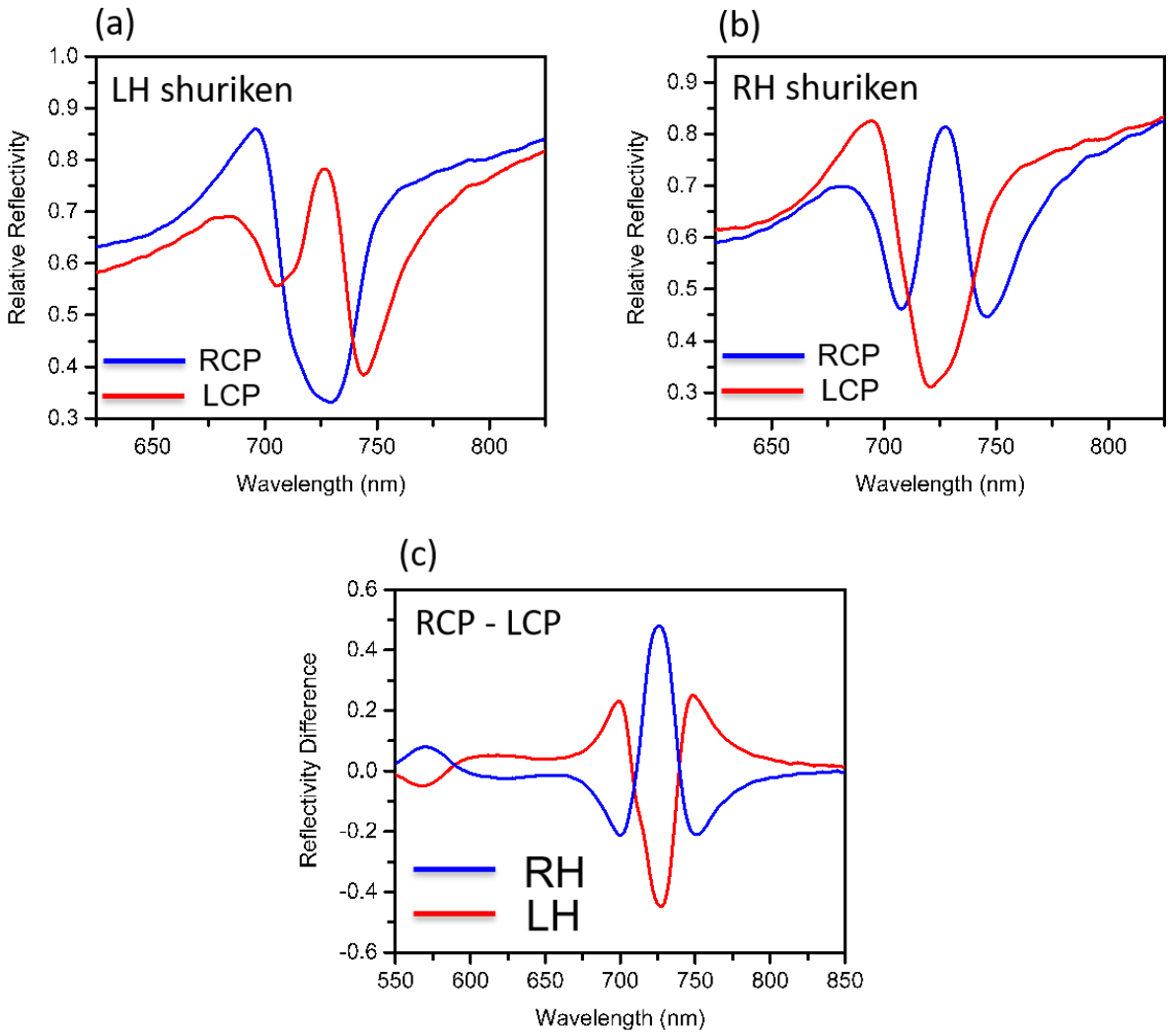

Figure 3.7. Shuriken Reflectivity under CPL Excitation. Relative reflectivity spectra for (a) LH shuriken nanostructures and (b) RH shuriken in water are shown for illumination with LCP (red) and RCP (blue). The separation between the two dips in the PIR resonance peak is opposite for the two structures with respect to the handedness of light. A difference spectrum (c) is given (calculated as the RCP spectrum minus the LCP) to demonstrate this equal but opposite behaviour for each of the LH (red) and RH (blue) nanostructures.

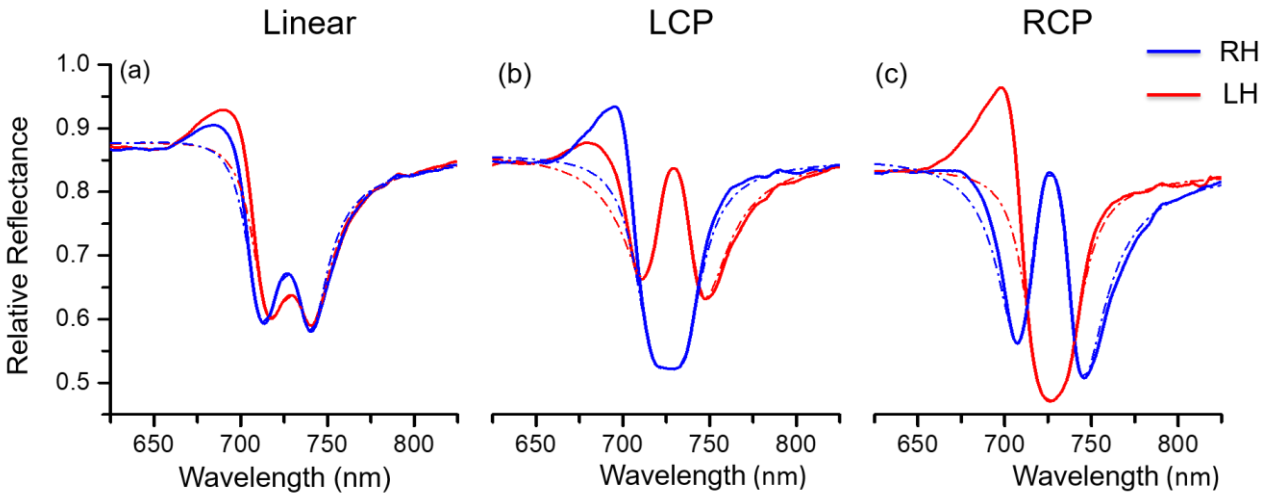

Figure 3.8. Comparison of Experiment and Model Reflectivity Spectra for Shuriken Nanostructures. Experimental data (solid lines) and curves fitted by the PIR model (dashed lines) are included for LH (red) and RH (blue) shuriken nanostructures in water. There is good agreement between experiment and the modelled spectra at the PIR resonance for all of (a) linearly polarized input light, (b) LCP and (c) RCP.

TABLE 3-2. PARAMETERS USED TO REPLICATE EXPERIMENTAL REFLECTIVITY DATA IN FIGURE 3.8

	LH nanostructures, polarisation			RH nanostructures, polarisation		
Parameter	**Linear**	**LCP**	**RCP**	**Linear**	**LCP**	**RCP**
ω_r	729.8	732.8	729.9	727.5	728.8	733.5
ω_d	729.5	726.7	729	727	726.3	723.5
κ	0.036	0.048	0.026	0.039	0.028	0.051
γ_r	0.03	0.064	0.0223	0.029	0.027	0.059
γ_d	0.036	0.008	0.045	0.0303	0.045	0.003
θ	-23	-25	-12	-24	-11.3	-20.4
ϕ	-21.2	-22.3	-10	-22.5	-10.3	-16
ϕ-θ	1.8	2.7	2	1.5	1	4.4

As previously noted in discussing these results, the most notable changes in the reflectivity spectra from LPL to CPL in in the peak intensities, controlled by γ_r and γ_d as well as the separation of the two peaks, otherwise considered as the coupling constant κ. We can see that they correspond well to the changes in separation seen in the spectra. Higher coupling – 0.048 ± 0.001 and 0.051 ± 0.001 for LH with LCP

and RH with RCP respectively - than for linear (0.036 ± 0.001 for LH and 0.039 ± 0.001 for RH) is obtained when the structure and light handedness are matched. When the structure and light are mis-matched, lower coupling constants of 0.026 ± 0.001 for LH with RCP and 0.028 ± 0.001 for RH with LCP are found. This then suggests that the strength of the coupling between the two modes in a metamaterial exhibiting PIR can be controlled by the interaction of the chirality of the incident light, i.e., that of the chiral near-field, and the chiral plasmonic modes of the nanostructure.

The near-fields of these structures exhibit a chiral asymmetry that via the choice of incident polarisation allows the coupling – the optical properties – of the metamaterial to be modified. The specifics of this interaction will be investigated in more detail using electromagnetic simulations in chapter 4. This finding has important implications for optical devices of this nature, as this enables the ability to control the optical properties of a metamaterial without the need for geometric or structural modification. In general, the properties and hence the function of such a device could then be manipulated without the requirement for the design and fabrication of a modified metamaterial.

The approach described so far is of course limited itself as the only operational types for a shuriken metamaterial of a given handedness are the linear, matched and mis-matched, as well as the potential for intermediate steps with elliptically polarised light. An approach in which the optical chirality of the nearfield and its coupling to the bright and dark modes is more finely controlled would broaden its usefulness as a sensing platform. The method chosen for this was the addition of chiral dielectric layers to the gold surface, in order to modify the local optical chirality experienced by the near-fields. Reflectivity spectra were then collected under linearly polarised light excitation for the LH and RH shuriken structures.

The first chiral molecule chosen for this was a chiral liquid layer of α-pinene. Both α- and β-pinene exist as two chiral enantiomers labelled as (+) and (-), and α-pinene was chosen as the model for this experiment owing to its availability. The results are shown in **figure 3.9**, in which the dashed lines are the measurements in water and the solid lines are in pinene. A measurement of a racemic mixture of the two pinene enantiomers is also included as a control. Note that there is a large wavelength shift between the two owing to pinene having a refractive index of 1.47 as opposed to 1.33 for water.

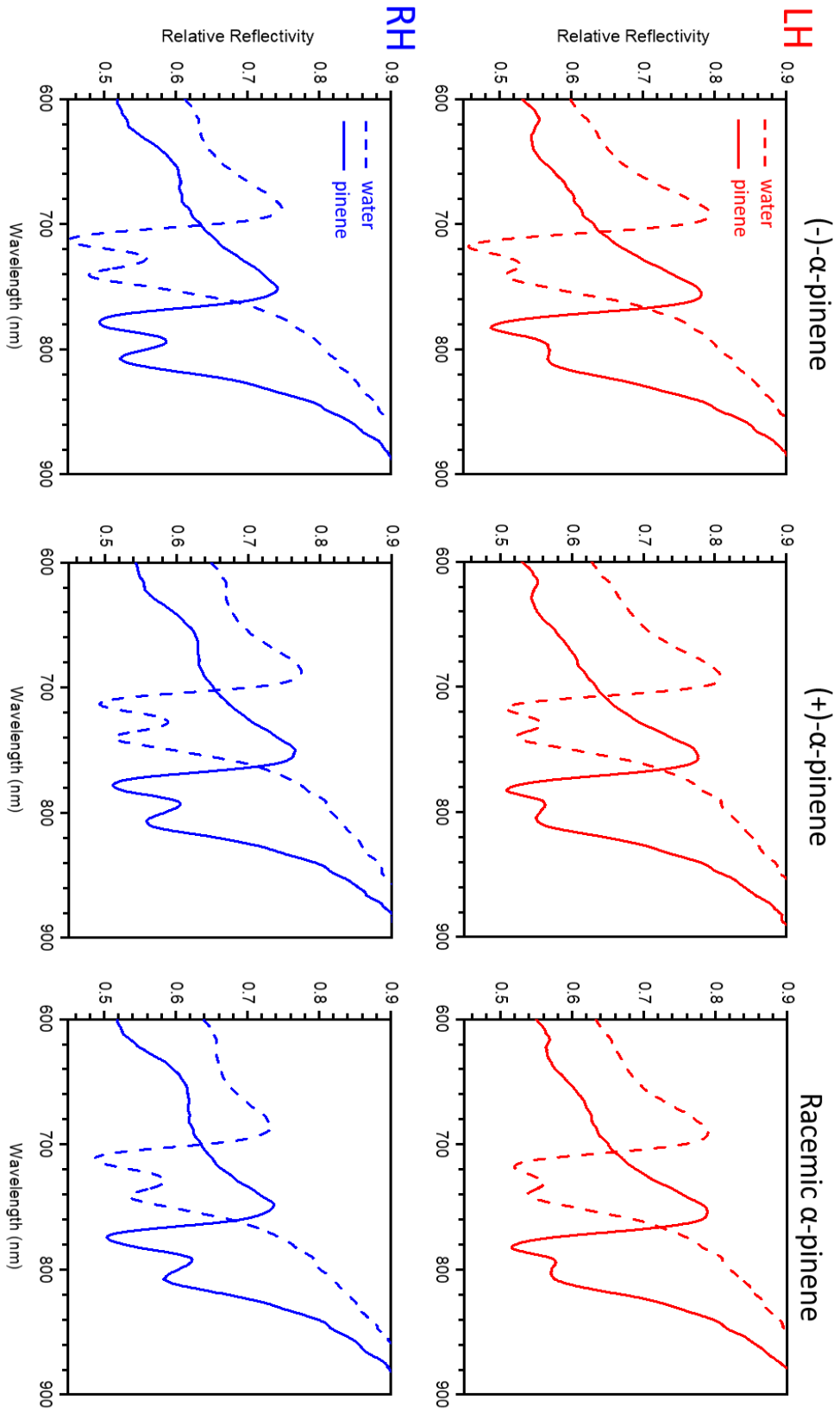

Figure 3.9. Effect of α-pinene Layer on Shuriken Nanostructure Reflectivity. Reflectivity spectra for LH (red) and RH (blue) shuriken nanostructures in water (dashed lines) and α-pinene (solid lines). Measurements of the two enantiomers (-)-α-pinene and (+)-α-pinene are shown in the top and middle rows, and for a racemic mixture of them in the bottom row.

In the experiment in which CPL was used, the coupling constant was determined from the mathematical model as a metric for the differences in the spectra, which was acceptable even given its error. However, in this case the changes may be too slight for the model to be appropriate, but as from the initial testing of the model it is known that the coupling parameter modifies the spacing between reflectivity dips in the spectra, this can be measured directly from the data, giving a more precise reading on the change in the coupling in the presence of a chiral dielectric. In **figure 3.10,** a closeup of the PIR resonance peaks is shown of the data in **figure 3.9**. The spectra collected in pinene have been shifted horizontally to overlay the water spectra at the 718 nm peak, to aid in the comparison. Vertical lines have been added at the peak positions to show the peak separation for the LH/RH shuriken in water, ${}^{water}S_{LH/RH}$ and LH/RH shuriken in the chiral liquid pinene ${}^{chiral}S_{LH/RH}$. Using these additions then, a difference ΔS (**equation 3.14**) can be defined to parameterise the change in coupling constant with an achiral dielectric to that on addition of a chiral dielectric layer to the metamaterial surface. Further, the parameter ΔΔS in **equation 3.15** will determine the asymmetry in the coupling responses of the oppositely handed nanostructures to each enantiomer and the racemic mixture,

$$\Delta S_{LH/RH} = {}^{Chiral}S_{LH/RH} - {}^{Water}S_{LH/RH} \quad [3.14],$$

$$\Delta\Delta S = \Delta S_{RH} - \Delta S_{LH} \quad [3.15].$$

Calculations of these parameters are given in **table 3-3**. The findings in **figure 3.10** and **table 3-3** are similar to those in the CPL experiment – each given handedness of nanostructure has an asymmetric response to the two enantiomers, and this asymmetry reverses for the other handedness of structure. Specifically, in the presence of the (+)- enantiomer of α-pinene, the peak separation for the RH structure increases by 1.2 nm more than it does for the LH. Conversely, with the (-)-enantiomer peak separation for the RH increases by 1.4 nm less than the LH.

TABLE 3-3. PIR PEAK SEPARATIONS AND ASYMMETRY FACTORS FOR LH AND RH SHURIKEN NANOSTRUCTURES UNDER PINENES

	(-)-α-pinene	(+)-α-pinene	Racemic α-pinene
ΔS_{LH} (nm)	2.5 ± 0.2	1.6 ± 0.2	3.3 ± 0.2
ΔS_{RH} (nm)	1.1 ± 0.2	2.8 ± 0.2	3.4 ± 0.2
$\Delta\Delta S$ (nm)	-1.4 ± 0.3	1.2 ± 0.3	0.1 ± 0.3

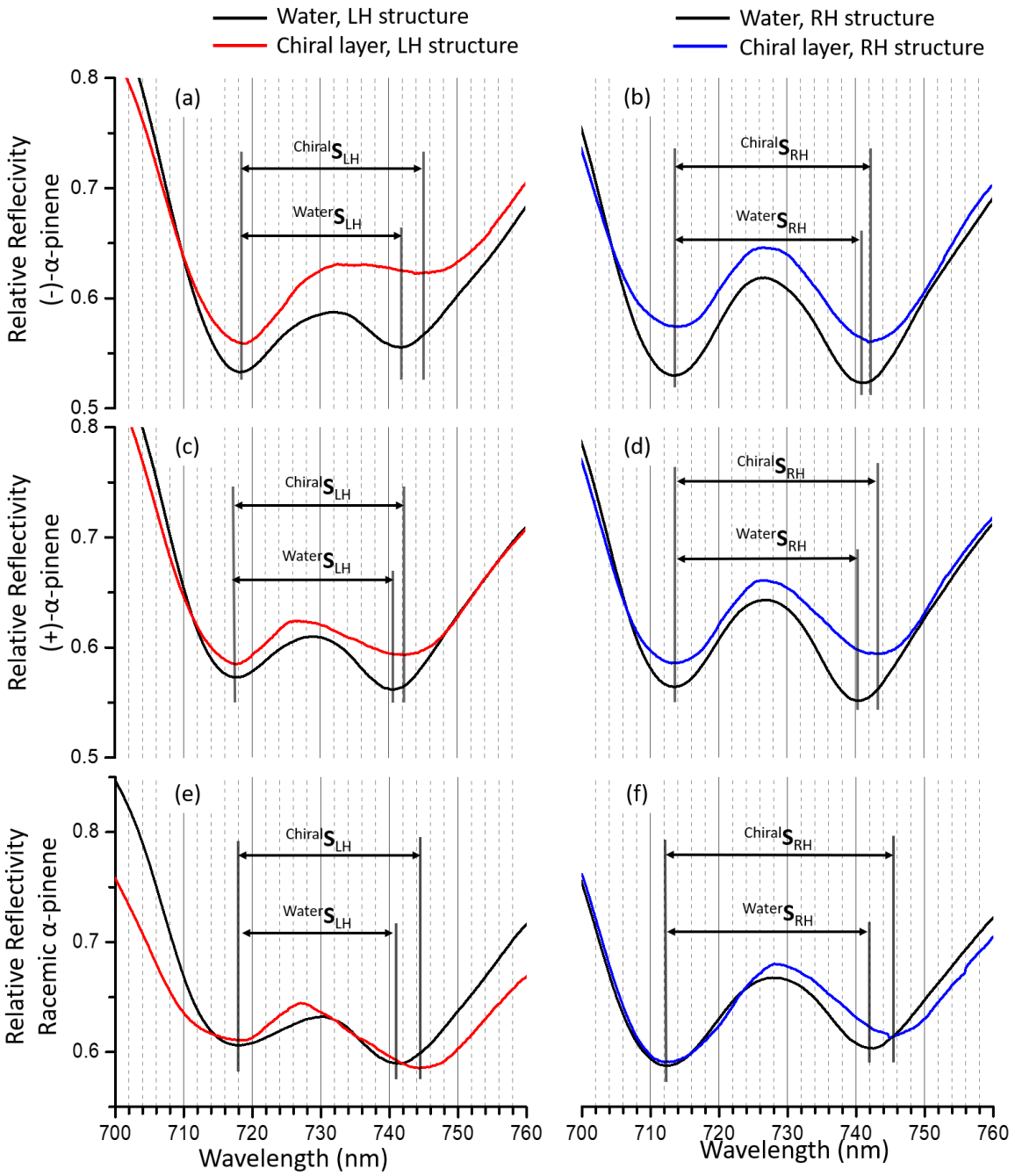

Figure 3.10. Determining PIR Coupling in the Presence of a Chiral Dielectric. Data presented in **figure 3.9** are shown here zoomed in on the PIR resonance peak, including experimental reflectivity in water (black) and chiral material for (a, b) (−)-α-pinene, (c, d) (+)-α-pinene and (e, f) racemic α-pinene. For those with pinene red lines are used for the LH structures and blue for the RH. The spectra for shuriken in pinene have been horizontally shifted to overlap with those in water to aid comparison. Black bars are added to guide the eye in the comparison of the separation between the PIR peaks. The separations are given in **table 3.3** and act as a convenient way to parameterise the coupling.

In addition, in the case in which the dielectric layer has no overall chirality (racemic mixture) there little to no change within error. This is further evidence then of the coupling of the bright and dark modes to the external field being influenced by the chiral asymmetry of the nearfield.

The ΔS values quoted in **table 3-3** signifying the difference in peak separation between water and pinene is included here given its similarity to values such as wavelength shifts often quoted in the literature. ΔS may not be reliable for the pinenes specifically as a result of wavelength being non-linear with energy, which becomes relevant due to the large difference in wavelength position between the water and pinene peaks. However, the relative difference, $\Delta\Delta S$, does not have this issue as it eliminates the comparison to the peak separation in water, so is considered to be a sound quantity to study here.

Slight differences in the initial water measurements are a result of different individual samples being used for each pinene liquid layer – the organic material leaves a residue that cannot be removed without damaging the sample. Given that the change in spacing from water to pinene and not the absolute value is our metric here, this difference is not detrimental to the results. However, it is noticeable that the overall shape of the resonance peak changes quite dramatically in the presence of pinene, and that even in the case of the racemic mixture where there is no chiral asymmetry the absolute peak separation in the resonance increases significantly. Given that the red-shift in the spectra with the pinene is a result of the higher refractive index at the structure surface than with water, it may then also be the case that this change in the resonance peak results from that as well. A viscous chiral liquid occupying the entire extent of the evanescent of the plasmonic metamaterial may be modifying the spectra more than would be optimal to detect the small changes being looked for. As such, it would be pertinent to add a chiral material with a refractive index much closer to that of water to the surface to ensure that a chiral asymmetry in the coupling could be observed without this dramatic shift in the spectra. As a check that smaller refractive index changes would not largely modify the spectra, a series of reflectivity measurements were taken for the LH and RH shuriken with linear polarisation using solutions of NaCl at concentrations varying from 0 M to 1.0 M, **figure 3.11**. These solutions gave a range of refractive indices from n=1.334 for water up to n=1.343 for 1.0 M aqueous NaCl (values measured using refractometry).

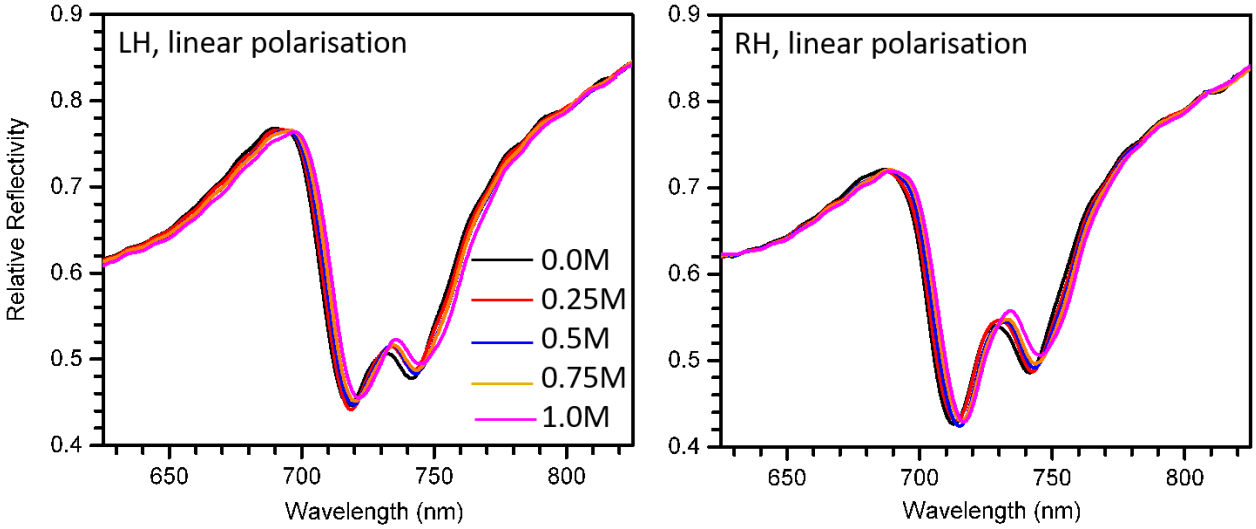

Figure 3.11. Shift in Reflectivity Spectra from Salt Solutions on Shuriken Nanostructures. Reflectivity spectra of LH and RH shuriken nanostructures with increasing concentrations of aqueous NaCl, from 0 mol L^{-1} up to 1.0 mol L^{-1} on their surface were measured. The spectra shift as a result of changes in refractive index of the salt solutions from 1.334 to 1.343 over this range. The achiral salts, as with the racemic α-pinene, show no asymmetry in the peak separation.

What can be seen is that the increase in refractive index does shift the spectra as expected as well as slightly decreasing the intensity of the peak, but the phase and coupling of the salt solution spectra remain unchanged compared to water, which is the desired result for an achiral analyte solution. In addition, a material with a stronger chiroptical response than pinene would result in higher asymmetries, or similar asymmetries for less material. The strength of the chiral response of a molecular layer on a surface can be quantified by the optical chirality parameter ξ (**equation 3.16**) that depends on its absorption frequency ω_0:

$$\xi = \beta_c \left(\frac{1}{\hbar\omega + \hbar\omega_0 + i\Gamma_{12}} + \frac{1}{\hbar\omega - \hbar\omega_0 + i\Gamma_{12}} \right) \qquad [3.16],$$

where β_c is a material-specific constant and Γ_{12} is the width of the chiral excitation resonance.

The specifics of this factor and how it can be calculated will be covered in more detail in chapter 4, in which this expression is used to create chiral dielectric layers in electromagnetic simulations. The relevant point at this stage is that the closer the absorption of the chiral analyte material is to the resonance, the higher the value of

ξ and the stronger the chiral response. With that in mind chlorophyll was chosen to act as the chiral molecular layer in the following experiments because it absorbs in the visible region at around 450 nm and 650 nm, close to the resonance around 700 nm, and thus was expected to show high chiral asymmetry. Chlorophyll is also soluble in ethanol which has a refractive index much closer to that of the salt solutions and water (n = 1.36) compared to pinene, so would shift in wavelength less than pinene as was needed.

The experiment to test this new material then, as shown in **figure 3.12**, was that the reflectivity of the shuriken structures with pure ethanol on the surface would be measured (using the injection cell as earlier in this chapter), followed by a solution of chlorophyll *a* in ethanol to check for any changes in coupling as observed with the pinene. The top row in the figure shows the pure ethanol and a 0.1 mg ml^{-1} chlorophyll *a* solution in ethanol for the LH and RH structures.

Although there does appear to be a slight difference in the phase for the RH structure when chlorophyll *a* is added, for LH and RH there is no change in coupling or indeed a shift in wavelength that was expected. As there was a possibility that this outcome was a result of the low concentration of chlorophyll *a* used, another experiment with a 1.0 mg ml^{-1} concentration was also completed in the same manner. Comparing these results in the bottom row of **figure 3.12** with the lower concentration, it can be seen that these slight observed phase changes are not consistent, and there is a complete lack of any shift or coupling change or indeed a difference in the resonance intensity as was seen with the salt solutions. It is necessary to consider here why this is the case. It would appear that the concentration of chlorophyll *a* has little influence over the reflectivity response when measured in this way. A possible reason then may arise from the difference between the two analyte layers. One is a liquid comprised entirely of chiral molecules, and the other is solution of chiral molecules in an achiral solvent. Given that the chiral plasmonic fields present at the nanostructure surface are evanescent, and as such only extend a distance from the surface on the order of hundreds of nanometres, key to the observation in the pinene experiment may be proximity to the structures.

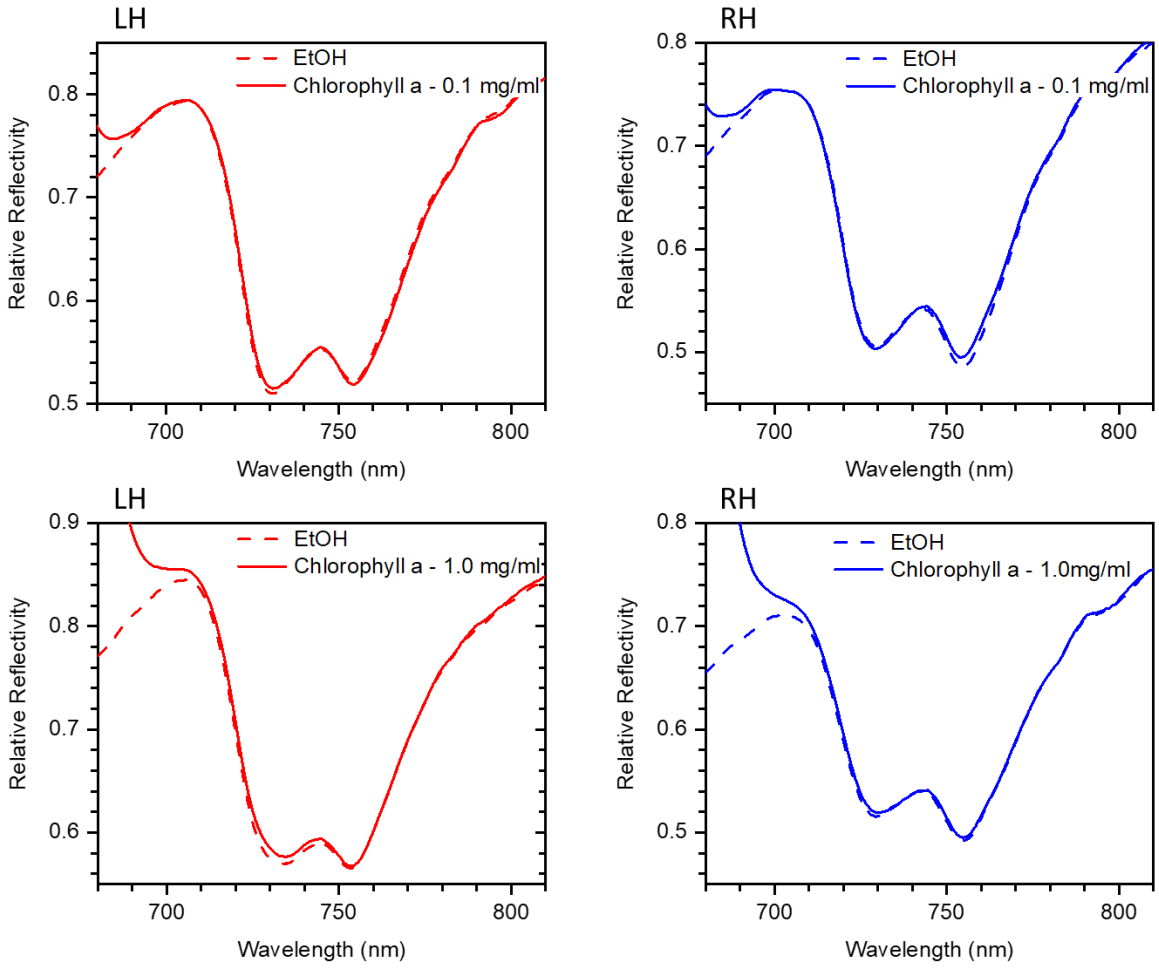

Figure 3.12. Effect of Chlorophyll a Solution on Shuriken Nanostructure Reflectivity. Comparisons of reflectivity spectra of LH (red) and RH (blue) shuriken nanostructures in different concentrations of chlorophyll a in ethanol. 0.1 mg ml^{-1} (top) and 1.0 mg ml^{-1} (bottom) concentrations are shown as solid lines, where the dashed lines are the ethanol solvent only. There are no evident changes in coupling constant from ethanol to the chlorophyll solution.

Indeed, the original chlorophyll *a* experiment has no inherent way of ensuring the chlorophyll *a* molecules are close to the surface. To solve this, a new method was developed with the intention of increasing the concentration of molecules at the surface. After first measuring the reflectivity of the structures with 100 µl water on the surface, with a microscope cover slip over the sample, the water was dried off and a 1 µl drop of the 1 mg ml^{-1} chlorophyll a solution was added to the surface, directly on top of the nanostructure arrays. The sample was then left for a short time to allow the ethanol to dry out, depositing the chlorophyll onto the nanostructures in a thin layer. 100 µl of water was then added to the surface before having cover slip placed over the liquid. Water was used in this part over ethanol used in the previous

experiment to prevent the chlorophyll from dissolving and leaving the structure surface. The reflectivity was then measured again with this setup, all of which for both the LH and RH shuriken. **Figure 3.13(a)** and **(b)** show the resonance peaks for the water and chlorophyll *a* layer in water, and **(c)** and **(d)** are zoomed in slightly with the same analysis as used for the pinene experiment – showing the separation parameter S for each measurement.

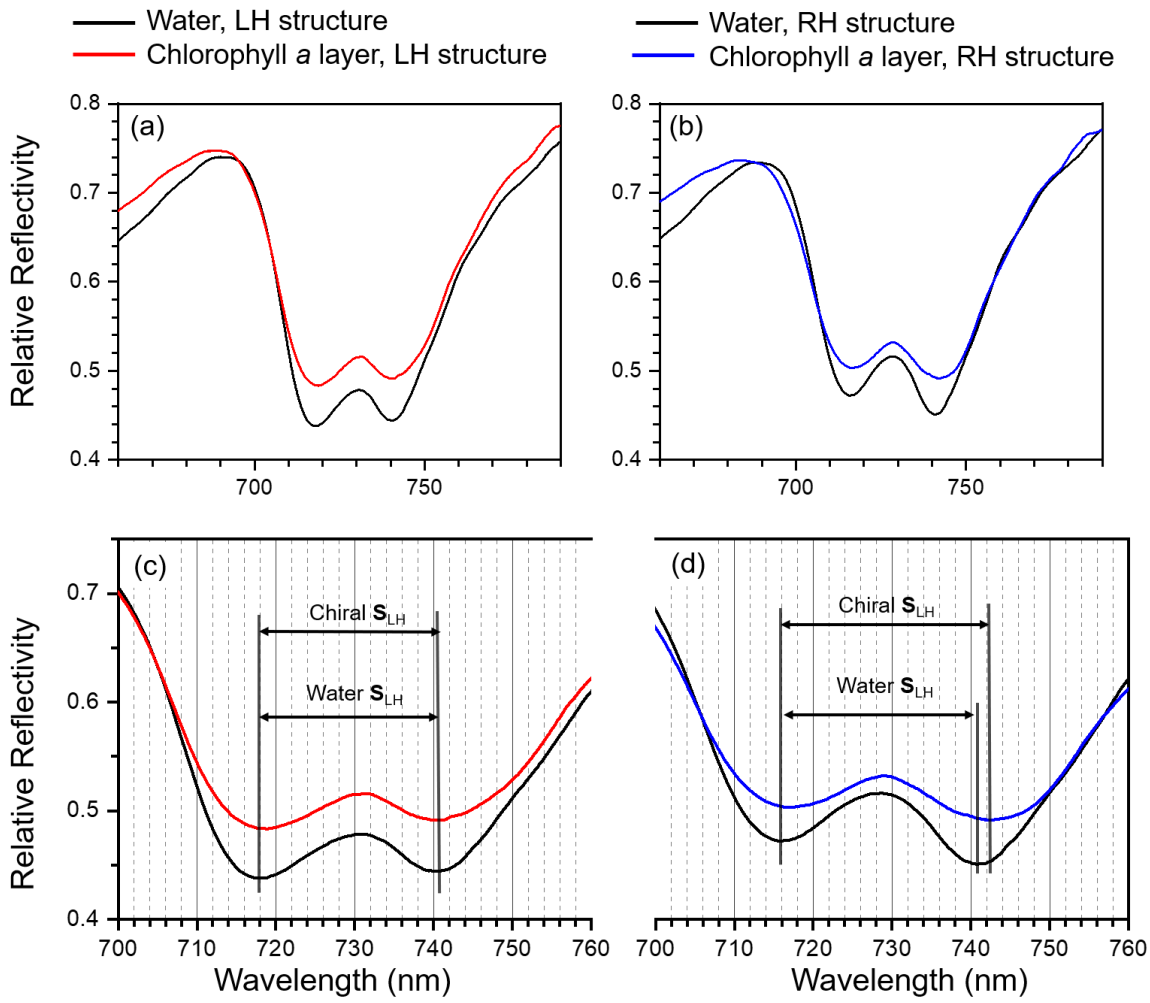

Figure 3.13. Effect of Dried-on Chlorophyll a Layers on Shuriken Reflectivity. 1 µl drops of 1 mg ml^{-1} chlorophyll a in ethanol were dried on the shuriken surface, then covered in water before having (a, b) reflectivity of LH (red) and RH (blue) structures measured. Black lines are reflectivity in water with no chiral layer. Similar to figure 3.10 with pinene, (c) and (d) show close-ups of the resonance peaks, so that the separation can be determined. The chlorophyll spectra have been shifted to overlap with water to aid comparison.

What can now be seen with this method (along with the change in resonance intensity as seen with the pinene is that one shuriken handedness – the LH – shows no change in separation of the resonance dips (a.k.a. no change in coupling) from water to chlorophyll *a* whereas the other handedness shows an increase in separation/coupling. The difference in separation between water and chlorophyll *a* as well as the asymmetry parameter $\Delta\Delta S$ are quantified in **table 3-4**, along with the values for the pinene experiments from **table 3-3**. The asymmetry parameter obtained for this method of depositing the chiral material directly onto the structures then is similar in magnitude to the chiral liquid layers, and again is indicative that an imposed chiral asymmetry in the nearfield can manipulate the coupling of the electromagnetic modes in the chiral plasmonic metamaterial to the external field and each other.

TABLE 3-4. PIR PEAK SEPARATIONS AND ASYMMETRY FACTORS FOR LH AND RH SHURIKEN NANOSTRUCTURES WITH DIELECTRIC LAYERS, INCLUDING PINENES AND CHLOROPHYLL A.

	Chlorophyll *a*	(-)-α-pinene	(+)-α-pinene	Racemic α-pinene
ΔS_{LH} (nm)	0.0 ± 0.2	2.5 ± 0.2	1.6 ± 0.2	3.3 ± 0.2
ΔS_{RH} (nm)	1.0 ± 0.2	1.1 ± 0.2	2.8 ± 0.2	3.4 ± 0.2
$\Delta\Delta S$ (nm)	1.0 ± 0.3	-1.4 ± 0.3	1.2 ± 0.3	0.1 ± 0.3

The experiments discussed in this chapter in which chiral nearfields were modified by external stimuli, namely circularly polarised light and two variations on the addition of a chiral dielectric layer, have led to key results confirming that the coupling of chiral modes can be controlled with chiral asymmetry. The plasmon induced reflection phenomenon observed in the shuriken shaped metamaterial has been used as a marker for these findings, as the coupling constant can be extracted simply using a mathematical model for such a system, or emulated by the peak separation in the reflectivity dip.

In order that full confirmation of the coupling manipulation being a result of changes to the chiral nearfield, it is necessary to measure this 'chirality' in the fields, and connect it to the spectra obtained in experiment. The method by which this will be done is with electromagnetic simulations. In chapter 4, the COMSOL Multiphysics software will be used to simulate the interactions of light with the chiral metamaterials, and the process of emulating chiral dielectric layers to imitate these experiments will be discussed.

Chapter 4 - Electromagnetic Simulations for Chiral Dielectrics

In order to further validate experimental results in this thesis, electromagnetic simulations have been performed using the COMSOL Multiphysics® software. In particular, computational results in this chapter act as a companion to the experimental results of chapter 3. COMSOL is capable of solving for a variety of problems including thermodynamics (e.g., heat flow), classical mechanics (e.g., shear stress) and electromagnetics (e.g., current flow) using the finite element method.

The finite element method (FEM) is a computational technique in which a system represented by a (3-dimensional, in this case) model is broken down into discrete objects – the 'finite elements' – connected by boundaries formed as result of the shape and size of the elements. These boundaries are called nodes, and a FEM solver is capable of numerically calculating solutions to a set of partial differential equations at the nodes, such that the solutions are continuous across these boundaries.[115] These simpler equations are then assembled into a system of more complex equations that can then allow solutions to be calculated throughout the volume between the element nodes. In this work, the wave optics module in COMSOL allows for Maxwell's equations to be solved using the FEM. With Maxwell's equations, approximate values for the electric and magnetic fields, charge density, displacement field and other such quantities can be calculated over points, surfaces and volumes within the simulated system. By adding a source of electromagnetic waves to the model, mimicking light sources used in experiment, optical problems can be solved in the frequency domain. This then provides the information necessary to calculate measured values from experiment such as reflectivity, transmission, ORD and CD, in addition to electromagnetic field intensities and optical chirality.

Results in this chapter have been published by ACS Photonics in 2017 in the paper "Controlling Metamaterial Transparency with Superchiral Fields", as well as in JACS in 2018 in the paper "Chiral Plasmonic Fields Probe Structural Order of Biointerfaces".[91,93] Some experimental work presented in the latter paper was performed by co-author Ryan Tullius, and as such will be noted in the text and figure captions where included.

BUILDING A MODEL

ELECTROMAGNETIC WAVE EQUATIONS

In the COMSOL model within the wave optics module, a set of equations must be added that are titled “Electromagnetic Waves, Frequency Domain” (EWFD). This allows the use of a FEM solver to find approximate numerical solutions to Maxwell’s equations (**equations 4.1** to **4.4**) using the form shown in **equation 4.5**.

$$\nabla \cdot \vec{D} = \rho \quad [4.1]$$

$$\nabla \cdot \vec{B} = 0 \quad [4.2]$$

$$\nabla \times \vec{E} = -\frac{\partial \vec{B}}{\partial t} \quad [4.3]$$

$$\nabla \times \vec{H} = \vec{J} + \frac{\partial \vec{D}}{\partial t} \quad [4.4]$$

$$\nabla \times \frac{1}{\mu_r}(\nabla \times \vec{E}) - \omega^2 \varepsilon_0 \mu_0 \left(\varepsilon_r - \frac{i\sigma}{\omega \varepsilon_0}\right)\vec{E} = 0 \quad [4.5]$$

Here $\vec{E}, \vec{D}, \vec{H}$ and $\vec{B}$ represent the electric field, electric displacement, magnetic field and magnetic flux density respectively, where $\vec{J}$ denotes the current density and ρ the charge density. Physical properties of materials involved in the light-matter interaction are described by the remaining parameters, including conductivity σ, vacuum and relative permittivities ε_0 and ε_r, and vacuum and relative permeabilities μ_0, and μ_r, where ω is the frequency of the electromagnetic wave incident on the modelled structure. These equations can be modified to account for the inclusion of materials with unusual properties, which will be discussed later.

THE 3D MODEL

With the necessary mathematics in place, a virtual model meant to replicate the physical system must be built. The fabricated metamaterials used in this work consist of square periodic arrays containing hundreds of thousands of nanostructures. Of course, a design as complicated as that would have an astronomically high number of elements to solve the equations for resulting in either the solution lacking the nanoscopic detail required, or the solver requiring impractically long calculation times. These issues can be worked around by instead creating a single model structure within domains of well-defined shape and size (describing the surrounding materials) and then repeating it in the x and y directions

by giving it suitable boundary conditions. In COMSOL, so-called 'Floquet' periodic boundary conditions are used, essentially converting a periodic problem into a linear one by treating paired surfaces on opposite sides of the model as if they were in contact. Work by Hakoda *et al* demonstrates how these conditions are implemented in COMSOL, for waveguides in their study.[116] A diagram showing what the full 3D model looks like in COMSOL is given in **figure 4.1**.

A 3D representation of the nanostructure, substrate and their surroundings is constructed as shown. The nanostructure is constructed using a computer-aided design (CAD) software such as Rhinoceros and designed to replicate the ideal shape (e.g., shuriken) used in the fabrication of physical samples. As in chapter 3 the metamaterial consists of a 100 nm thick solid structure with 80 nm of the solid thickness embedded into the substrate, leaving an 80nm deep hole with an identical shape directly above it. Domains (i.e., 3D regions) above and below this are added with a thickness suitable to allow for calculation such as reflectivity to be performed in the far-field. They are then assigned material properties taken from the internal library in COMSOL in order that they will act as closely to the physical materials as possible. Thus, polycarbonate is used for the domain below the gold solid structure and film, and air, water, and/or chiral dielectric are used for the domains above the gold as appropriate. The material properties defined for these domains include dielectric constant, conductivity, magnetic and thermal properties and so on.

Other planes are then defined in the model to create objects necessary to facilitate accurate calculation. 100 nm thick domains are added at the top and bottom of the model to be defined as the 'Perfectly Matched Layer' (PML), a perfect absorber that prevents the electromagnetic waves from being reflected from those surfaces. The inner surfaces of the PML are then designated as ports – the input port at the top where the waves will enter the system and the output port at the bottom where they will leave. Lastly, 50nm further in than the ports extra planes are added for calculations. These 'Integration Surfaces' can be used to calculate reflection, for example, as given in **equation 4.6**. The vertical faces are given periodic boundary conditions, as described above, to mimic the arrays of structures in the real samples. This unit cell is then entirely fragmented into a series of polyhedral finite elements called the mesh. The size of elements in this mesh can be controlled to improve precision if necessary, and defines the nodes and boundaries at which the calculations will be performed.

Typical finite element calculations performed for simulations in this chapter have about 350000 elements in the model unit cell and took around 20 hours to calculate for a full range of wavelength values in order to mimic experimental results in chapter 3.

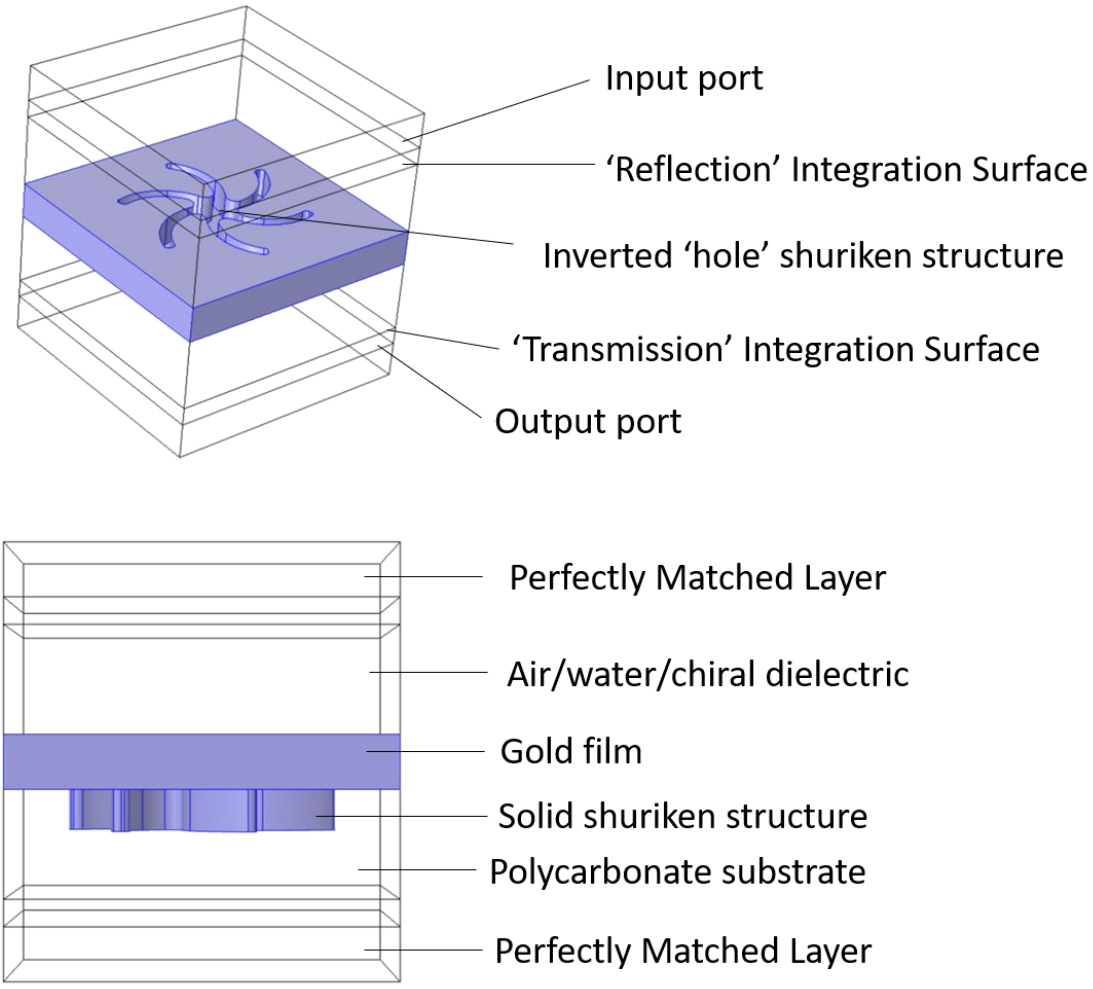

Figure 4.1. **Shuriken Metamaterial 3D Model.** The perspective view (top) and side-on view (bottom) of the shuriken metamaterial unit cell was taken directly from the COMSOL 3D model viewer. The solid-inverse shuriken model itself is constructed and imported from a CAD software, and the cuboid around it including the individual horizontal planes are defined in COMSOL. The materials used in experiment are applied to each domain in the model as shown. Features necessary for calculation are added at this stage, including the ports, integration surfaces and perfectly matched layer. Following this being built, the unit cell will then be broken down into the mesh elements, after defining the periodic boundary conditions.

RESULTS AND DISCUSSION

REFLECTIVITY SPECTRA

Having constructed the model as described in the previous section, tests must be run in order to determine both is the simulation is working and calculating at all, and if it is, if it can replicate experimental data with reasonable accuracy. For both, relative reflectivity spectra are calculated in COMSOL in the same manner as it would be for experiment, but with data collected at the input integration surface. The reflectivity can then be calculated according to **equation 4.6**:

$$\text{Reflectivity} = 1 - \left|\frac{P_{av}}{P_0}\right| \qquad [4.6],$$

where P_{av} is the average outflow power calculated at the 'Reflection' integration surface (see **figure 4.1**) and P_0 is the incident light power from the input port. This expression added into the variables in COMSOL will then allow for the reflectivity to be calculated at a single frequency (or wavelength, as our spectra will be plotted here). In order for the model to construct a full spectrum over the region of interest, a 'parametric sweep' must be created in the software. A range of wavelengths and a step size between wavelength points can be defined, giving control of the precision at the resonance wavelength, and making sure the resonance peak can be calculated with a single simulation without it taking an impractical amount of time with too many points in one model.

As an initial test for the gold shuriken nanostructure model, the reflectivity was calculated for both LH and RH shuriken, with a diameter of 500 nm and 200 nm interstitial spacing, and compared to the experimental results from chapter 3, **figure 4.2**. Incident light was linearly polarised, with the plane of polarisation oriented along the y-axis. A mirror image transform was used in the software to flip the structure to obtain an opposite handedness, ensuring the exact symmetry was maintained. To replicate experimental conditions, the domain above the gold in the model was set to be water and in the first instance the structure was illuminated with linearly polarised light. In the interest of saving on calculation time, the simulation only covers from 670 nm to 750 nm with high precision rather than the full range measured in experiment.

The expectation for this simulation was that a spectrum exhibiting the plasmon induced reflection (PIR) phenomenon would be obtained, as that would be consistent with experimental observations. After many attempts to have the model produce any reflectivity at all (a first foray into building a model from scratch can be quite complicated) the result in the left panel of **figure 4.2** was calculated. At a glance, there is obvious qualitative similarity between the simulated spectra and the experimental ones in the right panel. The characteristic double dip with a reflection peak in-between is found, and the LH and RH metamaterials are found to have exactly the same shape as each other at the resonance region. This is to be expected in the simulation, as the shuriken are both taken from the ideal fabrication shape and are illuminated with linearly polarised light, so there is no chiral asymmetry. There are some minor differences between the simulation and experiment however – the separation between the two PIR peaks and the position of the resonance are slightly lower in the simulation. The reason for this is thought to be differences in the real shuriken nanostructure and the idealised version used in the model. Indentations in the solid part of the shuriken, unforeseen thickening of the arms in fabrication or minor differences in the structure diameter could contribute to these differences. A move towards understanding these minute discrepancies and modifying the CAD models to better represent the physical structures presents possible further work in this subject that is beyond the scope of this thesis. Given the high level of agreement between the two methods, this model was chosen to be used for further simulation work using the shuriken, in order to further validate experimental results in chapter 3.

CIRCULARLY POLARISED LIGHT

Continuing on using the established 3D shuriken model, simulations were conducted using a modification to the input electromagnetic wave to make it circularly polarised. Keeping the input power from the port the same in the y-direction as for linear polarisation, a phase term of $+i$ or $-i$ was added to the x-component of the input field, depending on whether RCP or LCP was desired respectively. The simulation would then provide two crucial pieces of information – firstly whether the model designed above could replicate the same effect on the PIR peaks when illuminated with CPL as with the experiment, and also directly calculated values of optical chirality density *C,* to verify that manipulation of *C* in the nearfields by CPL results in asymmetry in the coupling between modes in the PIR system.

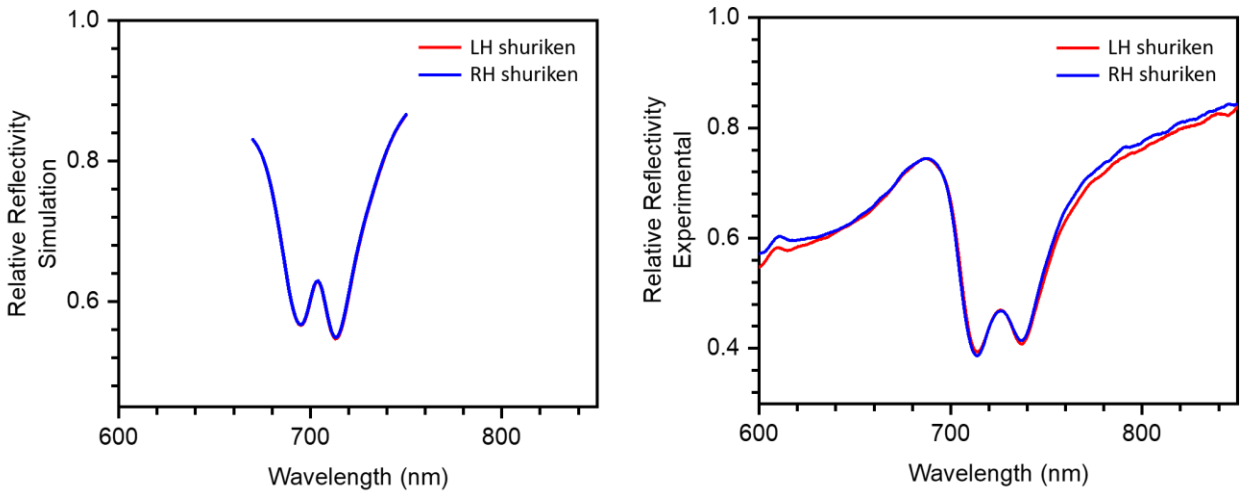

Figure 4.2. Comparison of Simulation and Experimental Reflectivity. Reflectivity spectra for the LH (red) and RH (blue) shuriken nanostructures are given for the COMSOL simulation (left) and experiment (right) performed and described in chapter 3. Both have the PIR line shape predicted by the model in the previous chapter, and the resonance appears at similar wavelengths.

As such, an additional set of four simulations, for the LH and RH metamaterials with each of LCP and RCP illumination were run, and reflectivity spectra calculated as before for each combination. This was added to the data for linearly polarised light in **figure 4.2** and produced the results shown in **figure 4.3,** mirroring the experimental results from **figure 3.8**. The separation between the two peaks is then determined from the data, as this is a good measure for the coupling between modes as has been discussed previously. This data is summarised in **table 4-1** with values to the nearest nm. It seems that for the circularly polarised light, the effect seen in the experiments is reduced in the simulations. In the experiments where the CPL and structure handedness were 'matched' (i.e., LCP light with LH structures and RCP with RH) the separation between the two PIR peaks increased by around 15nm, and the 'mis-matched' (LCP with RH and RCP with LH) decreased the separation to be too small to resolve by eye. In the simulations, the effect is the qualitatively similar but less pronounced – the matched simulations show a separation increase of about 3 nm, and the mismatched decreases by 7 nm, down to 10 nm rather than an approximate 5 nm or less. While there is some agreement, as the direction of the change in separation is consistent with experiment, the implication is that the simulations underestimate the level of coupling between the bright and dark modes in the PIR system comparatively to the experiment.

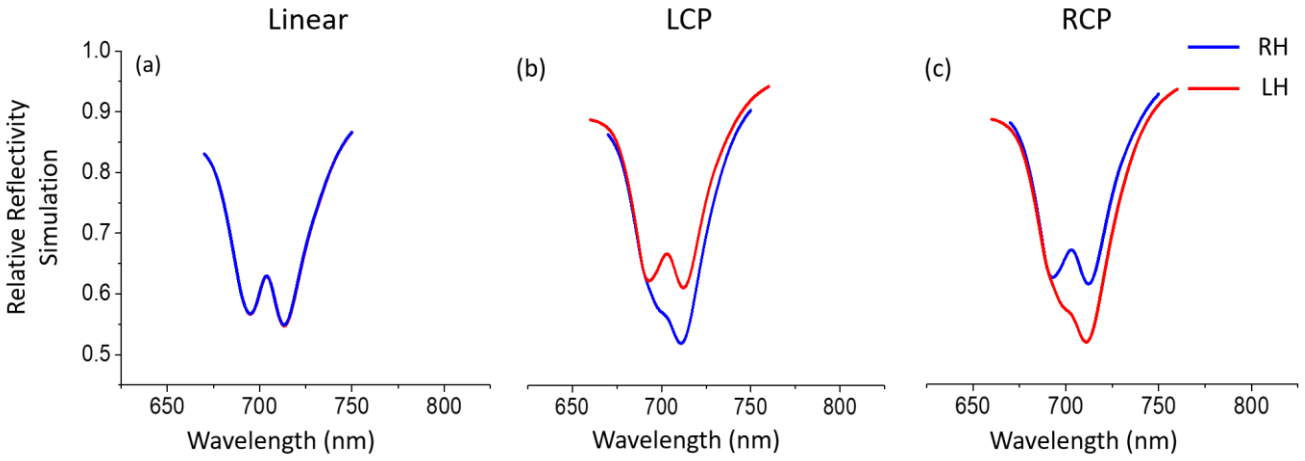

Figure 4.3. Circularly Polarised Light Simulations on Shuriken Metamaterial. Simulated reflectivity spectra are shown for LH (red) and RH (blue) shuriken nanostructures. The data for linearly polarised light illumination from figure 4.2 is included (left) along with that for LCP (middle) and RCP (right). An equal and opposite effect is found for the CPL between the LH and RH structures, as it was with experimental data.

TABLE 4-1. PIR PEAK SEPARATIONS FOR EXPERIMENT AND SIMULATION (LINEAR LCP AND RCP LIGHT) TO THE NEAREST NM

	Linear		LCP		RCP	
	Experiment	Simulation	Experiment	Simulation	Experiment	Simulation
LH peak separation	25 nm	17 nm	40 nm	20 nm	< 5 nm	10 nm
RH peak separation	29 nm	17 nm	< 5 nm	10 nm	41 nm	20 nm

The assumption here is similar to the more minor differences noted with the linearly polarised light – geometrical differences and defects in the fabricated samples that are difficult to reproduce in simulation. One example of this could be the curvature of the shuriken arms – the level of chirality induced in the nearfield could be underestimated if the shape of the shuriken in the simulation is not exact to the samples, as this is what gives the fields their intrinsic optical chirality when interacting with light. This result supports the understanding of this phenomenon by which CPL produces chiral asymmetry in the nearfields leading to changes in coupling, but is not quite conclusive. To support the claim then, calculations of optical chirality density can be carried out and given both visually as a spatially varying map over the structure, and numerically taken from points of increased chirality in these structures.

The optical chirality density *C* is a factor that can be used to parameterise the chiral asymmetry in an electromagnetic nearfield, and in some situations, e.g., at the hotspots of a chiral plasmonic nanostructure, can locally have values higher than that of CPL at the same frequency, i.e., they are superchiral. Here *C*, **equation 4.7**, has been implemented as a distinct calculation in COMSOL, taking into account the electric field strength $\vec{E}$ and magnetic flux density $\vec{B}$, allowing for the distribution of optical chirality over the structure surface to be determined at any chosen frequency ω that is one of the points in the parametric sweep.

$$C = -\frac{\varepsilon_0}{2}\omega Im\{\vec{E}^*.\vec{B}\} \qquad [4.7]$$

Based on the working understanding up to this point, the chirality in the nearfield of the metamaterial is dependent on both the input light polarisation and the handedness of the nanostructure. The spatial distributions of *C* at the top surface of the solid structures (i.e., at the bottom of the 'hole') have then been plotted for each combination of structure handedness and polarisation for which reflectivity was calculated for **figure 4.3**, at the approximate centre wavelength of the resonance peak, about 703 nm. These optical chirality maps are normalised against the absolute value of *C* for CPL at this wavelength (C_{CPL} ~ 0.0029 kg A^2 m^{-2}) and are shown in **figure 4.4** (**(a-c)** LH nanostructures, **(d-f)** RH nanostructures). The sign of *C* on the scale bars designates the handedness of the nearfield, where blue is LH and red is RH, so by looking at the plots the fields generated around each structure are a mixture of both LH and RH fields with one in excess. Qualitatively we can say that the chirality in the fields is more intense in the matched cases compared to the linear polarisation (i.e., stronger LH fields for the LCP with LH structure, and similar for the RH), and that for the mismatched combinations the LH and RH fields are more evenly distributed over the structure. There is a clear asymmetry between LH and RH structures in the chiral fields when the structure is illuminated with CPL, which reverses when the handedness of the light is changed. There are clear points at which the optical chirality is increased above the value of CPL (that would be 1 on the scale here) by at least 5, if not an order of magnitude or more (the scale bars are reduced to aid in visualisation of the minimum regions), most notably around the borders and ends of the shuriken arms.

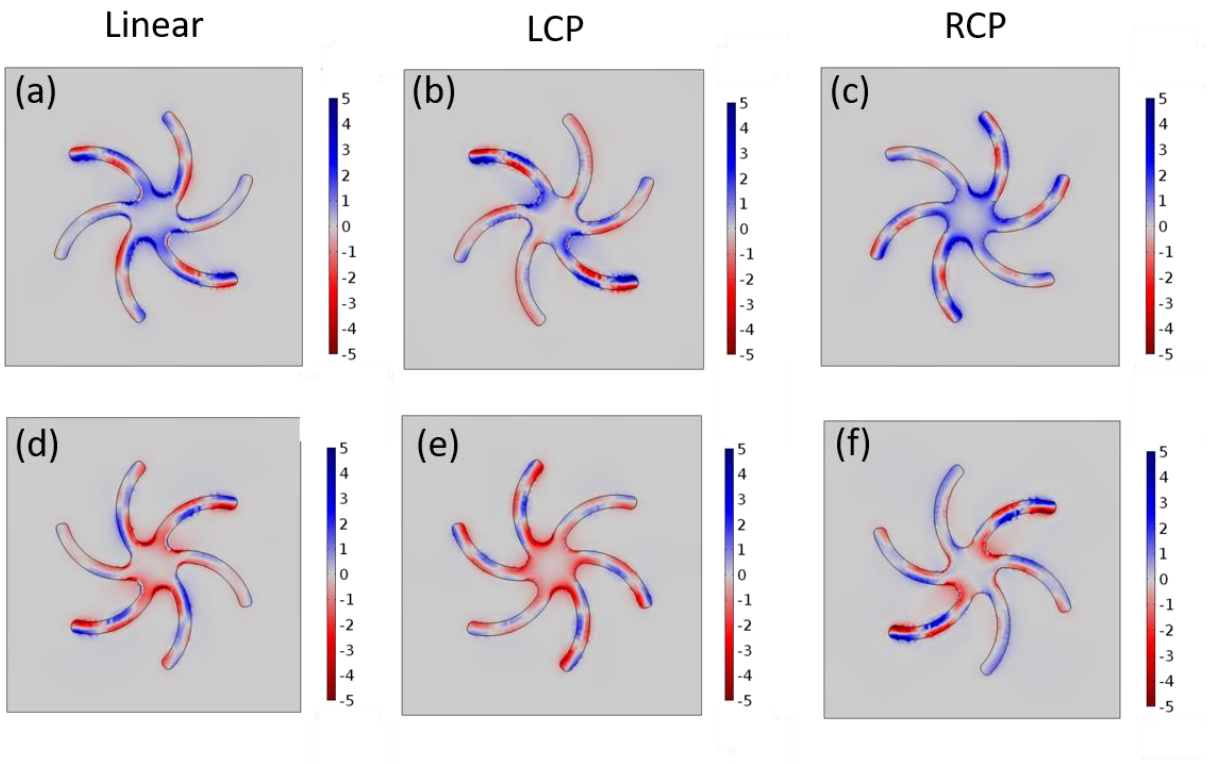

Figure 4.4. Spatial Distribution of Optical Chirality Density. The value of *C* is calculated at 703 nm and is normalised against the value for CPL. It is plotted in a plane covering the surface between the solid and inverse structure of the (a-c) LH shuriken metamaterials and (d-f) RH metamaterials. The light (a, d) linear (b, e) left circular and (c, f) right circular polarisations are included for each handedness of structure. The colour scales have been fixed at the range shown to aid in visualisation of the lower chirality values.

Given the hypothesis that the chiral asymmetry in the nearfields induced by the CPL leads to the asymmetry in the coupling – that coupling in LH structures is governed by LH fields and equivalent for RH – it can be suggested that the maximum points of LH chirality correspond to the points of strongest coupling in LH structures and similar for the RH. To test this, a parameter called C_{max} is defined for points that can be observed by eye in these chirality maps with the highest values, i.e., the most positive field for the LH structures and the most negative field for the RH. In **figure 4.5** the values of C_{max} are plotted against the coupling constant values calculated from the PIR model in chapter 3 for each combination of polarisation and structure. C_{max} values were determined by selecting the most intense areas in the chirality maps and performing a point calculation for *C* in those areas.

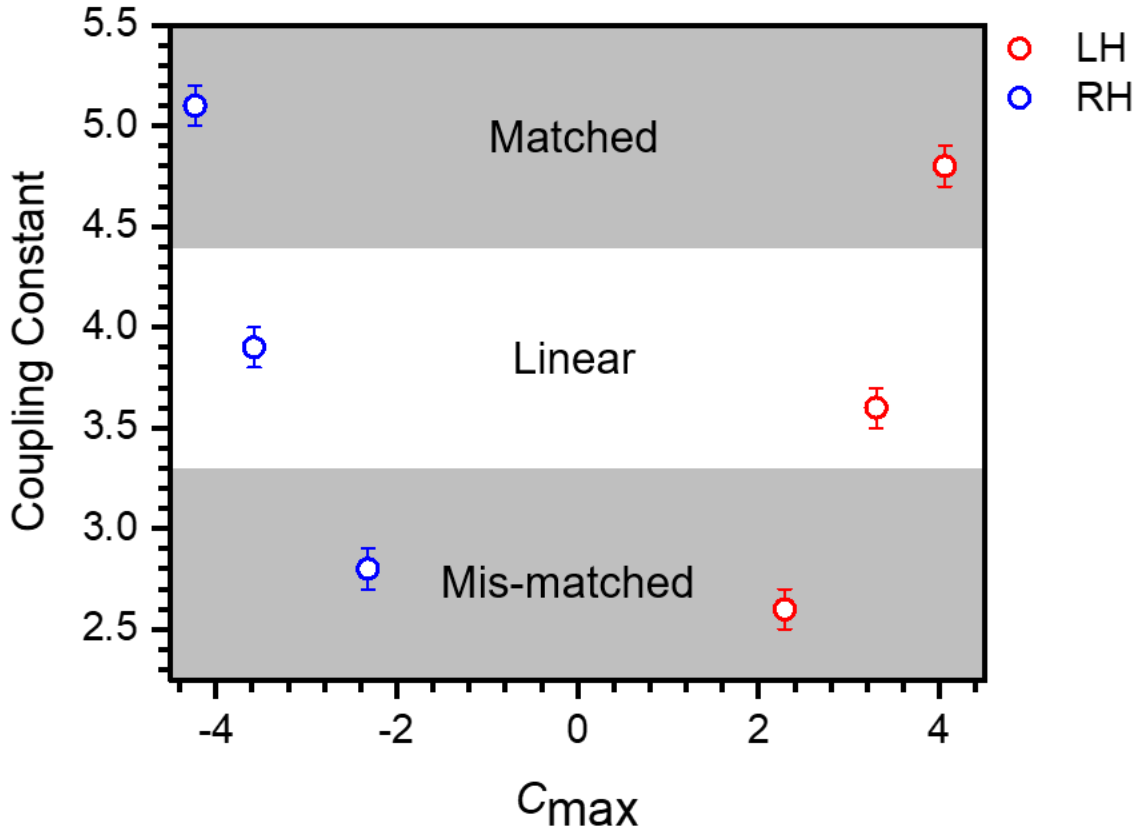

Figure 4.5. **Chiral Asymmetry from Simulation against Coupling Constant.** Points of maximum positive (LH, red points) or negative (RH, blue points) chirality are calculated from the simulations and plotted against coupling constant determined by the PIR model. Regions on the plot are marked out to show the pattern of matched, mismatched and linear structure-polarisation combinations.

The results in this figure confirm then that the magnitude of the coupling between bright and dark modes in the PIR system, and hence the extent of any induced reflection/transmission, for chiral metamaterials is dependent on the asymmetry of the chiral nearfields controlled by the incident light polarisation. The pattern of 'matched' combinations of structure and polarisation showing the largest chiral asymmetry and strongest coupling, 'mismatched' showing the lowest and the linear being between the two is maintained from experiment to simulation.

An additional point should be made here concerning a curiosity in the symmetry of the chiral distribution maps. The shuriken nanostructures are, by design, six-fold rotationally symmetric but it is obvious looking at **figure 4.4** that the chirality is not. These spatial maps instead are two-fold symmetric, which is unexpected given their shape. The explanation for this is rather simple however – the shuriken are arranged in a square lattice that has four-fold symmetry, so the only overlapping rotation axis

the structure and the lattice have is a two-fold one. In **figure 4.6 (a)** there is a chirality map taken from a structure with periodic boundary conditions, i.e., it is in a square lattice shown by the scanning electron microscope image of the metamaterial samples given in **figure 4.6 (b)**. The last image in that figure is a chirality map taken from a simulation in which the boundary conditions were removed, leaving an isolated shuriken. As was expected, the isolated structure shows a six-fold symmetrical chiral field distribution. It is not known if an isolated structure like this would have any effect on the results, but given that experimentally measuring a single nanostructure using the available equipment would prove impossible, this has not been investigated further.

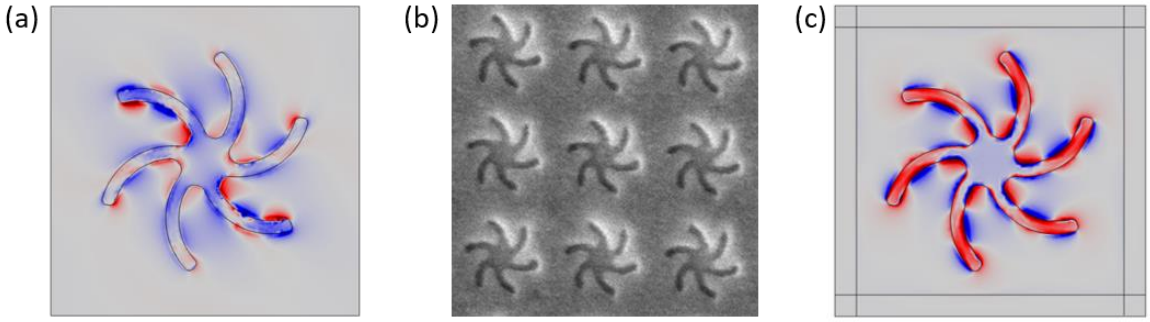

Figure 4.6. Explaining the Symmetry of the Chiral Fields. (a) The chirality for a shuriken excited by LCP is included along with (b) a scanning electron microscope image of the sample metamaterial showing the square array of shuriken, which together have C_2 symmetry. (c) The chirality of an isolated shuriken outside of the lattice has the expected C_6 symmetry.

Simulating Chiral Dielectrics

The Optical Chirality Parameter

The model and set of equations described above is able to accurately calculate electromagnetic fields and other properties of the metamaterial in isotropic, achiral environments. However, as was described by Tang and Cohen in the case where the analyte is chiral, referred to generally as a chiral dielectric in this work – be it a biological molecule bound to the structure surface, or a layer of a chiral liquid – a modification to the electric and magnetic fields equations is required.[54] Thus, an additional set of equations is added in the model to be included only in the domains which are representative of an isotropic chiral dielectric. The constitutive equations, **equations 4.8** and **4.9**, allow for the mixing of electric and magnetic fields via the

optical chirality parameter, $\tilde{\xi}$. This is a local second order tensor quantity describing the chirality of a material, which has non-zero elements for a chiral medium. In isotropic substances the elements of $\tilde{\xi}$ are equal for each of the x, y and z components of the electric and magnetic fields, and so can be utilised as a single value ξ and takes the form in **equation 4.10**.[96] The sign of ξ defines the 'handedness' of the chiral dielectric – positive is RH, negative is LH.[117]

$$\vec{D} = \varepsilon_0 \tilde{\varepsilon}_r \vec{E} + i\tilde{\xi}\vec{B} \quad [4.8]$$

$$\vec{H} = \frac{1}{\mu_0 \tilde{\mu}_r}\vec{B} + i\tilde{\xi}^T\vec{E} \quad [4.9]$$

$$\xi = \beta_c \left(\frac{1}{\hbar\omega + \hbar\omega_0 + i\Gamma_{12}} + \frac{1}{\hbar\omega - \hbar\omega_0 + i\Gamma_{12}}\right) \quad [4.10]$$

$\tilde{\varepsilon}_r$ and $\tilde{\mu}_r$ are spatially dependant relative permittivity and permeability functions, β_c is an intrinsic coefficient set at 4.1 x 10^{-4}, $\hbar$ is the reduced Planck constant ($\hbar = h/2\pi$), ω_0 is the absorption frequency and Γ_{12} is the intrinsic width of the resonance of the chiral excitation. It is then necessary for **equations 4.8** and **4.9** to be expanded mathematically, such that the x, y and z components of the electric displacement $\vec{D}$, magnetic field $\vec{H}$ and the first time-derivative of the magnetic field are implemented into this secondary set of electromagnetic equations in COMSOL. With this parameter implemented is then becomes possible that a system with no chiral nanostructures illuminated with linearly polarised light to exhibit calculable optical chirality as would be the case with a physical experiment with chiral molecules.

The observation in experiment and in previous simulations was that chiral asymmetry induced in the nearfield would modify the coupling between the bright and dark electromagnetic modes. In chapter 3, in addition to achieving this with CPL, chiral molecules were added to the metamaterial surface to manipulate the nearfields. Ultimately the aim of this section is to replicate those experiments with simulation, but before doing that a series of reflectivity spectra were calculated using COMSOL for a generic chiral dielectric with no real-life analogue, which was added above both the LH and RH shuriken metamaterial, **figure 4.7(a, b)**. The dielectric was given similar properties to how a layer of chiral liquid e.g., pinene would act on the surface, with a refractive index of 1.4, occupying the entire 200 nm thick domain above the gold layer. Starting from a ξ value of 0 to give a baseline for an achiral

material, the optical chirality parameter was gradually raised in steps up to ξ = 1.5x10^{-4}, working from the assumption that ξ = 1x10^{-3} would be an upper limit based on the work by Tang and Cohen. The key observation is that the separation between the PIR peaks (and hence the coupling, as explained by the PIR model) increases with ξ for the RH nanostructure and decreases with ξ for the LH. This is consistent with previous observations that a RH chiral perturbation, the chiral dielectric here, to a RH nanostructure will result in a strengthened coupling and a weakened coupling when applied to a LH structure. A corollary of this is that if the ξ is negative valued, the coupling would be stronger for the LH metamaterial and weaker for the RH. The asymmetry parameter $\Delta\Delta S$ defined in chapter 3 (the difference in ΔS for RH and LH structures, where ΔS is the change in separation compared to the achiral dielectric) has been calculated for each value of ξ used, as well as their negative counterparts, and plotted in **figure 4.7(c).** This result then is a demonstration of the chiral asymmetry in the nearfield, as induced by the chiral dielectric, directly modifying the coupling in the PIR resonance as parameterised by the peak separation. Finally, the C_{max} values for the shuriken with chiral dielectric are determined as before, taken at the interface between the solid and inverse structures, and plotted against the individual peak separations for each reflectivity spectrum in **figure 4.7(d)**. This shows the peak separation (and hence coupling) increasing directly with optical chirality density for the LH nanostructures, and decreasing for RH structures (the negative sign in the expression for C gives it the opposite sign dependence to ξ).

With a robust picture of how the use of chiral dielectrics can manipulate chiral asymmetry in the nearfields to control the coupling between PIR modes, the next step is to run calculations for a variety of chiral molecular layers to show that the simulation can predict the effect that such molecules will have on the metamaterial system.

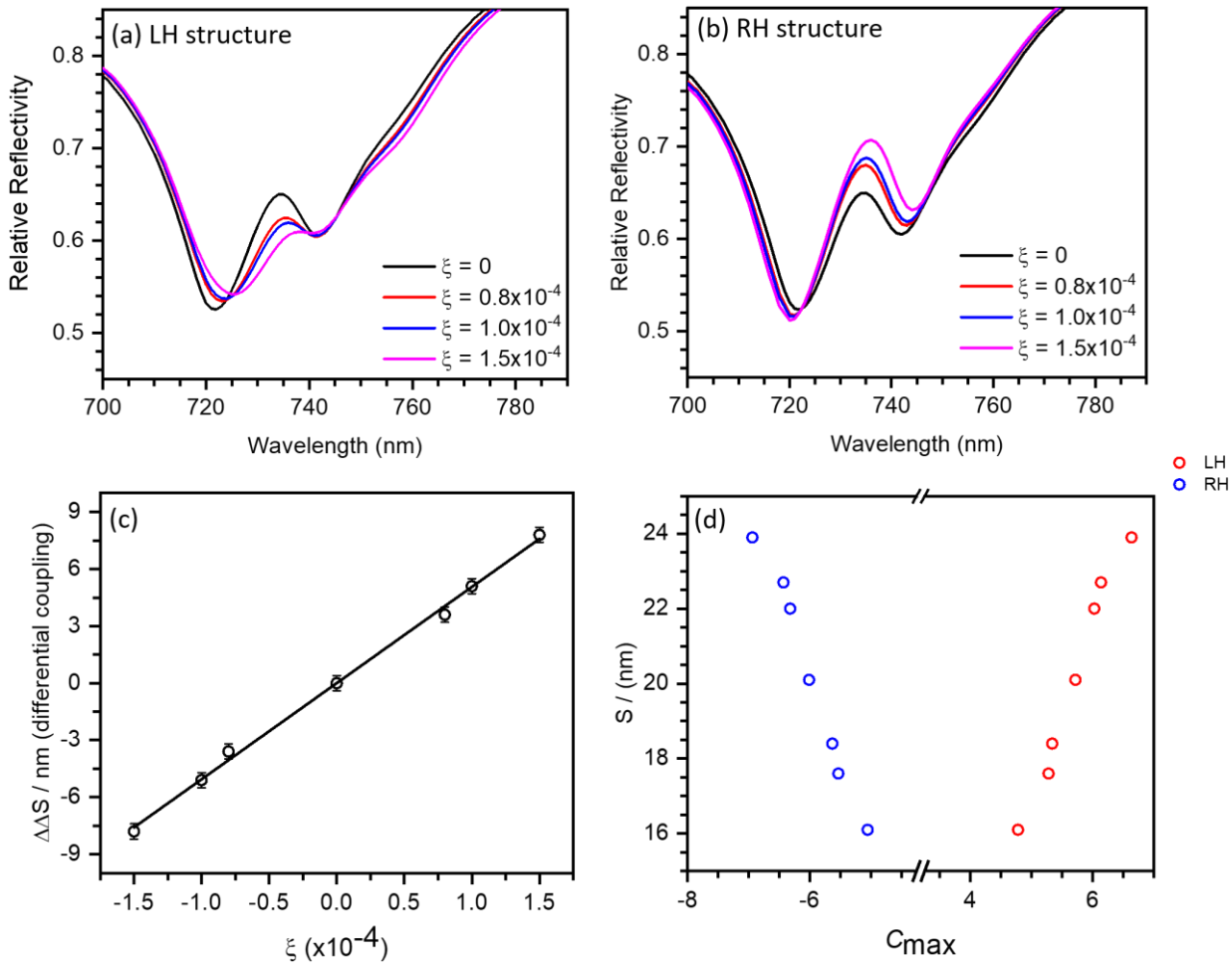

Figure 4.7. Effect of Varying Chiral Dielectrics on PIR Resonance. Reflectivity for dielectrics with increasing optical chirality parameter ξ for (a) LH shuriken and (b) RH shuriken. ξ values used are 0 (black), $0.8\text{x}10^{-4}$ (red), $1.0\text{x}10^{-4}$ (blue) and $1.5\text{x}10^{-4}$ (magenta). (c) The asymmetry parameter $\Delta\Delta S$ is then shown to have a linear variation with positive and negative ξ values in this range. (d) Peak separation is demonstrated to vary with optical chirality density for LH (red) and RH (blue) nanostructures. All simulations are for a 200 nm thick chiral dielectric layer with a refractive index of 1.4.

Simulations for Chlorophyll *a* and Pinene

Companion simulations to the experimental data for α-pinene and chlorophyll *a* in chapter 3 are achieved by keeping the 200 nm layer and refractive index of 1.4 for pinenes, and using a 20 nm layer with refractive index 1.34 (with the remaining 180nm taken up by water) to represent the adsorbed chlorophyll *a* layer covered by water. Before going ahead though, some consideration must be made to the specific ξ values that would best represent the physical properties of these molecules.

Equation 4.10 for ξ can be rewritten as in **equation 4.11** below by substituting the frequencies for the speed of light divided by wavelength:

$$\xi = \beta_c \left(\frac{1}{\mathrm{hc}/\lambda + \mathrm{hc}/\lambda_0 + i\Gamma_{12}} + \frac{1}{\mathrm{hc}/\lambda - \mathrm{hc}/\lambda_0 + i\Gamma_{12}} \right) \qquad [4.11]$$

Chiral organic molecules and biomolecules tend to have absorption in the UV region, so a first estimate will be used for absorption at about 200 nm. Chlorophyll however, as suggested by its green colour does not – it absorbs in the visible region at around 450 nm and 650 nm. Using parameters mentioned previously as well as Γ= 0.4 and setting λ_0 = 200 nm or λ_0 = 450 nm the curves of ξ against wavelength were calculated and shown in **figure 4.8** - the magnitude of ξ is plotted only, given that the imaginary part is negligible here. The 450 nm absorption for chlorophyll is used because it is generally the stronger absorption. As the resonance in the experimental data falls at ~ 700 nm we can use this figure to read off approximate values of ξ over this plasmonic region for pinene and chlorophyll. This corresponds this corresponds to ξ of ~ ±3x10^{-5} and ~3x10^{-4} respectively. The actual value used for pinene in the simulations was very close to this, at 2.6x10^{-5} providing the best representation of the experiment. Reflectivity spectra for LH and RH shuriken metamaterials with 200 nm of the facsimile of (+)-α-pinene, (-)-α-pinene and racemic α-pinene are provided in **figure 4.9**. Those for the 20 nm chlorophyll *a* layer are in **figure 4.10.**

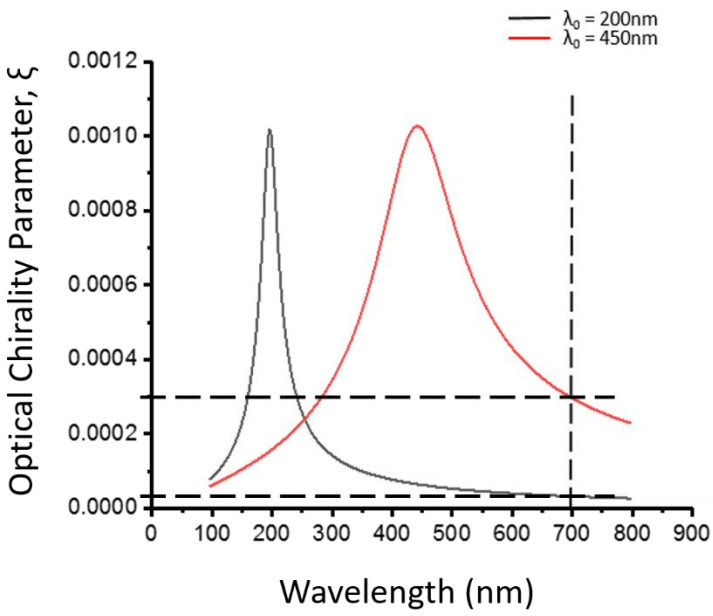

Figure 4.8. Variation of ξ with Wavelength. The black curve approximately corresponds to the pinene UV absorption, and the red curve to the chlorophyll absorption in the blue visible region. The dotted lines are then used to read ξ values for these materials off the graph, giving ~ 3x10^{-5} and ~ 3x10^{-4} respectively.

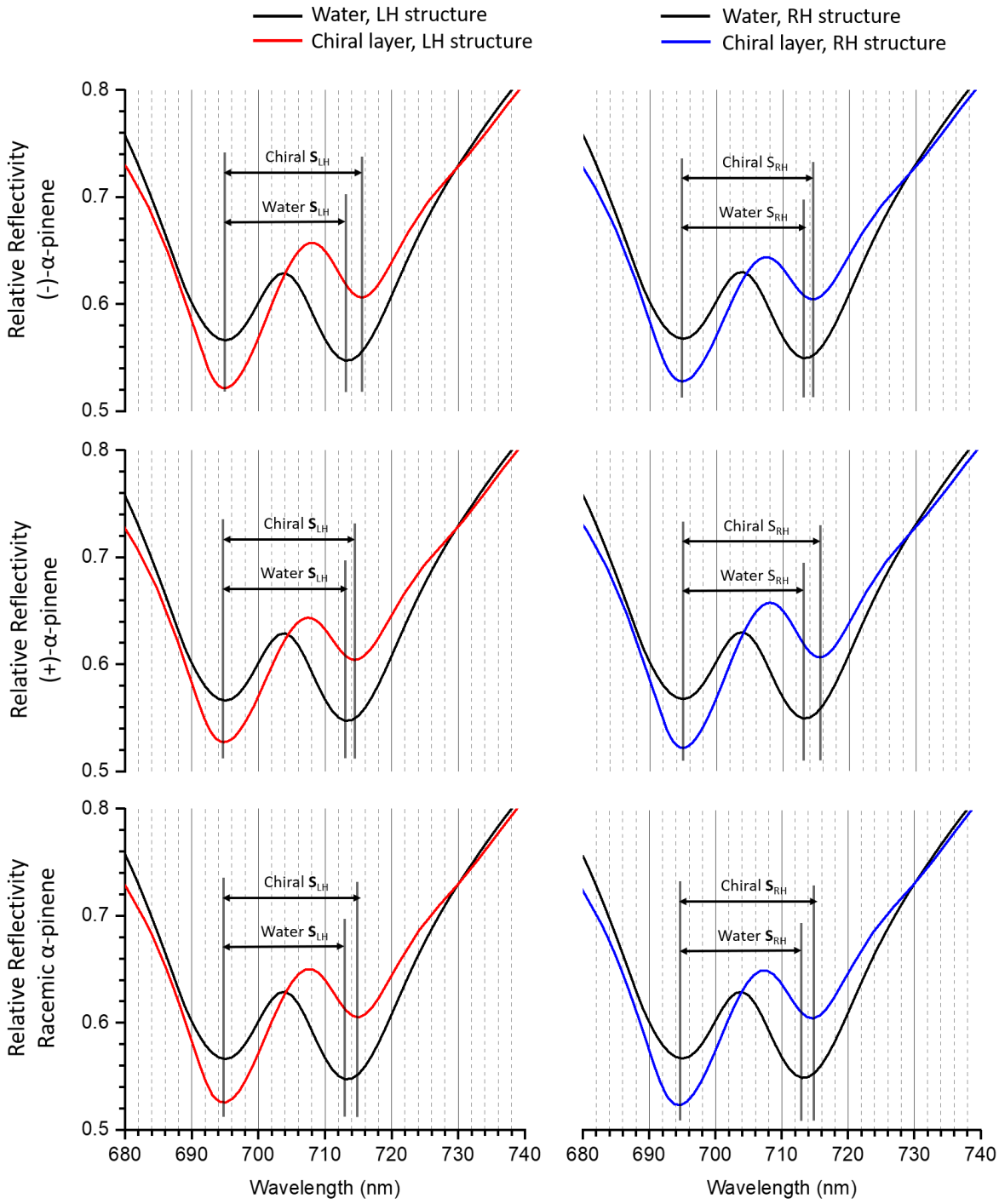

Figure 4.9. Reflectivity Simulations Representing α-pinene Liquid Layer. Each plot compares the simulated reflectivity spectrum for shuriken metamaterial with water on the surface (black lines) to that with (-)-α-pinene (top row), (+)-α-pinene (middle row) or a racemic mixture of both α-pinenes (bottom row). The reflectivity for both LH nanostructures (red lines, left column) and RH (blue lines, right column) are provided. Vertical lines have been added to guide the eye for the PIR peak separation distances, labelled as Chiral $S_{LH/RH}$ for those with the pinene layer on LH/RH structures, and Water $S_{LH/RH}$ for the equivalents with water. The spectra for pinene have been shifted horizontally to overlap at the left PIR peak with those for water, to help with the comparison. The pinene layers are all 200nm thick and have a refractive index of 1.4. ξ values are 2.6×10^{-5} for (+)-α-pinene, -2.6×10^{-5} for (-)-α-pinene and 0 for the racemic mixture.

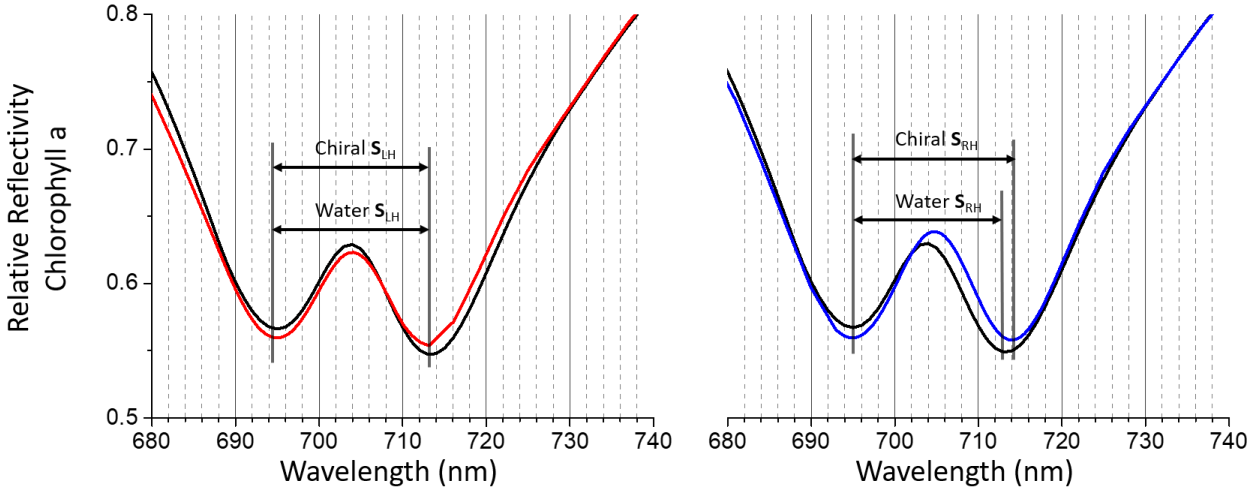

Figure 4.10. Reflectivity Simulations Representing Adsorbed chlorophyll *a* Layer in Water. Similar to figure 4.9, simulations for water (black), chlorophyll *a* on LH shuriken (red) and RH shuriken (blue) are included with vertical bars to show the peak separations. The chlorophyll *a* forms a 20 nm layer with refractive index 1.34 in the model with 180nm of water over it. The ξ value that was used for chlorophyll *a* is $3x10^{-4}$.

The peak separation values from these spectra were then calculated, as well as the differences in the separations between chiral layers and water. By subtracting the difference for LH from that for RH for each dielectric, asymmetry parameters $\Delta\Delta S$ are obtained for each. The results are summarised in **table 4-2**, along with the equivalent parameters taken form the experimental work in chapter 3 and the ξ values used in simulation. Both by inspection of the reflectivity spectra and by direct calculation of the asymmetry parameter there is very good agreement between simulation and experiment for the chiral molecular layers. There is a positive asymmetry for materials with positive ξ and the reverse for negative ξ, no asymmetry for layers with no net chirality and the asymmetry values from experiment are predicted with reasonable accuracy by simulation. It could therefore be possible to predict the behaviour of an isotropic layer of chiral molecules on a chiral metamaterial surface if there is knowledge of the absorption for that material for an accurate ξ. This also means that use of specific chiral molecules applied to the surface of a chiral metamaterial could tune its transparency properties, given their ability to modify the PIR coupling.

TABLE 4-2. ASYMMETRY PARAMETERS AND OPTICAL CHIRALITY PARAMETERS FROM EXPERIMENT AND SIMULATION

	(-)-α-pinene	(+)-α-pinene	Racemic α-pinene	Chlorophyll a
ΔΔS (nm) - Experiment	-1.4 ± 0.3	1.2 ± 0.3	0.1 ± 0.3	1.0 ± 0.3
ΔΔS (nm) - Simulation	-1.0 ± 0.3	1.0 ± 0.3	0.0 ± 0.3	1.1 ± 0.3
ξ (simulation)	-0.26×10^{-4}	0.26×10^{-4}	0.00	3.00×10^{-4}

ANISOTROPIC CHIRAL LAYERS

Up to this point the molecules that have been dealt with on the metamaterial surface have been assumed to be in isotropic layers – either in the form of a tumbling liquid or a randomly oriented solid. However, it may be the case that the chiral layer of interest for modelling is more complex than those examples, such as a layer of protein molecules on a surface to attached specific binding sites. This introduces the possibility of an anisotropic chiral material, and to make sense of that further modifications to the chiral equations in COMSOL must be made. It is now necessary to return to the description of ξ as a second-rank tensor where the sign of tensor components $\xi_{ij} \quad (i,j = x,y,z)$ is determined by the handedness of the chiral dielectric that it describes.

For an isotropic chiral medium, the values used for $\tilde{\xi}$ are spatially independent, which corresponds to only the diagonal elements of the chirality tensor $\tilde{\xi}_{iso}$ being non-zero, with:

$$\tilde{\xi}_{iso} = \begin{bmatrix} \xi_{xx}^{iso} & 0 & 0 \\ 0 & \xi_{yy}^{iso} & 0 \\ 0 & 0 & \xi_{zz}^{iso} \end{bmatrix} \qquad [4.9],$$

$$\xi_{xx}^{iso} = \xi_{yy}^{iso} = \xi_{zz}^{iso} \qquad [4.10].$$

This is because optical activity is determined from electric-dipole – magnetic dipole interactions for an isotropic medium. This interpretation was used in the previous section where, because the tensor is diagonal and all values are the same, it was treated as if it were scalar. In order to modify this tensor to suit anisotropic media, the form in **equation 4.11,** proposed by Theron and Cloete, will be utilised, making it possible to consider the influence of a quadrupolar moment on the chiral field and measured spectra.[118]

$$\tilde{\xi}^{aniso} = \begin{bmatrix} \xi_{xx}^{ani} & \xi_{xy}^{ani} & 0 \\ -\xi_{xy}^{ani} & \xi_{yy}^{ani} & 0 \\ 0 & 0 & \xi_{zz}^{ani} \end{bmatrix} \quad [4.11].$$

The diagonal elements of this tensor bear the same definition as in the isotropic version – they are a result of electric-dipole – magnetic dipole interactions. However, for an anisotropic medium the three diagonal elements are no longer equal, and for a molecule that is oriented perpendicularly to the metal surface, the diagonal z-direction tensor element becomes much higher than the other two. As such, in this work, we will say that $\xi_{xx}^{ani} = \xi_{yy}^{ani}$ but ξ_{zz}^{ani} is much larger than both of them. Indeed, proteins aligned with an electric field were found to exhibit much stronger circular dichroism than otherwise in work by Burck et al.[119] This then allows for a relationship to be formed between the tensor elements of an anisotropic layer of oriented molecules and those of an equivalent isotropic layer of disordered molecules. The diagonal elements of an isotropic chiral dielectric are given by:

$$\xi_{xx}^{iso} = \xi_{yy}^{iso} = \xi_{zz}^{iso} = \frac{1}{3}\left[2\xi_{xx}^{ani} + \xi_{zz}^{ani}\right] \quad [4.12]$$

An estimation from this is that ξ_{zz}^{ani} is larger than ξ_{xx}^{ani} and ξ_{yy}^{ani} by approximately an order of magnitude. As well as the difference in magnitude of the diagonal elements of the anisotropic tensor compared to the isotropic, there are also non-diagonal elements present that are not on the isotropic form. These components of the tensor represent the electric dipole – electric quadrupole contribution to optical activity in anisotropic media.[118] The magnitude of this contribution is lower the smaller the molecule is with respect to the extent of the electromagnetic field it lies within, as suggested by the work by Zhang and Govorov.[120] An estimate of the non-diagonal elements then is that they are approximately an order of magnitude smaller than the large diagonal element ξ_{zz}^{ani}.

The next step before applying this to a physical example is to understand how this modification must be implemented in COMSOL, so that anisotropic layers can also be simulated. Of course, there are now six tensor elements that must be taken into account rather than just three identical ones, which changes the form of the constitutive equations significantly. The x and y components of the electric displacement and magnetic field become dependent upon each other, although the expression for the z-component will remain the same. These field components and

the time derivative of the magnetic field are included in the equation set for chiral dielectrics, but now take anisotropy into account. The new form of the x and y components of the constitutive **equations 4.8** and **4.9** are:

$$\vec{D}_x = \varepsilon_0 \tilde{\varepsilon}_r E_x + i\left(\xi_{xx}^{ani} B_x + \xi_{xy}^{ani} B_y\right) \quad [4.13]$$

$$\vec{D}_y = \varepsilon_0 \tilde{\varepsilon}_r E_y + i\left(\xi_{yy}^{ani} B_y - \xi_{xy}^{ani} B_x\right) \quad [4.14]$$

$$\vec{H}_x = \frac{1}{\mu_0 \tilde{\mu}_r} B_x + i\left(\xi_{xx}^{ani} E_x - \xi_{xy}^{ani} E_y\right) \quad [4.15]$$

$$\vec{H}_y = \frac{1}{\mu_0 \tilde{\mu}_r} B_y + i\left(\xi_{yy}^{ani} E_y + \xi_{xy}^{ani} E_x\right) \quad [4.16]$$

Note here that $\xi_{xy}^{ani} = \xi_{yx}^{ani}$, so only ξ_{xy}^{ani} is shown for the sake of simplicity. Thus, the contribution from the quadrupole interaction can be seen by comparison with the original equations, as it mixes x and y components of the fields together.

With that in place, an example protein will be examined experimentally and with simulated counterparts to determine if the anisotropic modification to the optical chirality tensor can predict its behaviour, and to see what else it can tell us about such a system.

IgG Surface Adsorption

The structure of interfaces between biomolecules and their relative orientation is a crucial factor in biological systems as it governs their functionality. Chiral plasmonic metamaterials have been shown to be extremely sensitive to the presence of adsorbed biomolecules, such that spectroscopic techniques can detect them even in extremely low concentrations.[121,66] It was thought then that such a metamaterial could be sensitive enough to probe structural order of protein assemblies by leveraging the asymmetry of the chiral nearfields. Experimental work (the isotherms and experimental reflectivity) to that end was conducted by Ryan Tullius in 2016 using the highly abundant serum antibody IgG as a model protein assembly, and was published along with associated electromagnetic modelling in the JACS paper "Chiral Plasmonic Fields Probe Structural Order of Biointerfaces" in 2018.[91]

The assemblies consist of a self-assembled monolayer of NTA adsorbed onto the gold surface terminating in carboxylate groups, COO^-, to which layers of IgG molecules are strongly bound owing to its net positive charge, a system that has been extensively studied experimentally and theoretically.[122,123] As IgG is adsorbed onto the surface, it can be monitored by shifts in the wavelength of the plasmonic

resonance – a well-documented property of plasmonic systems, useful for quantifying adsorption.[124] If the analyte protein (which is chiral) is adsorbed onto a chiral plasmonic metamaterial, the wavelength shift recorded for the LH structure, $\Delta\lambda_{LH}$, and that for the RH structure, $\Delta\lambda_{RH}$, may well not be equal as they would be if the analyte material was achiral. In **figure 4.11 (top)** an adsorption isotherm has been measured for increasing concentrations (in mgml^{-1}) of IgG, using the average of the wavelength shifts of the LH and RH shuriken, $\Delta\lambda_{AV}$, (accounting for the shifts not being equal) to quantify the amount of protein that has adsorbed to the metamaterial surface. This average is relative to the resonance position in buffer.

$$\Delta\lambda_{AV} = \frac{\Delta\lambda_{LH} + \Delta\lambda_{RH}}{2} \qquad [4.17]$$

The red curve in the adsorption isotherm plot is a fit to the Langmuir model of adsorption in heterogeneous environments, showing that as concentration is increased towards saturation, the ability of the protein molecules to bind to the surface decreases.[125] This plot however does not contain any information as to the orientation of the proteins molecules or how the structure of the biolayer changes with concentration.

To complement the adsorption isotherm then, a plot that will be referred to as a 'structural isotherm' has been included in **figure 4.11 (bottom)** in which the variation of the asymmetry parameter $\Delta\Delta S$ with concentration is shown. $\Delta\Delta S$ has been selected as a parameter for this as it is inherently sensitive to chirality rather than thickness of the molecular layer, and hence it will be zero if the analyte is achiral. By comparison with the Langmuir isotherm, the structural isotherm has a maximum point that then exhibits a decrease in $\Delta\Delta S$ as it moves to saturated protein coverage at and above 1 mg ml^{-1} concentration.

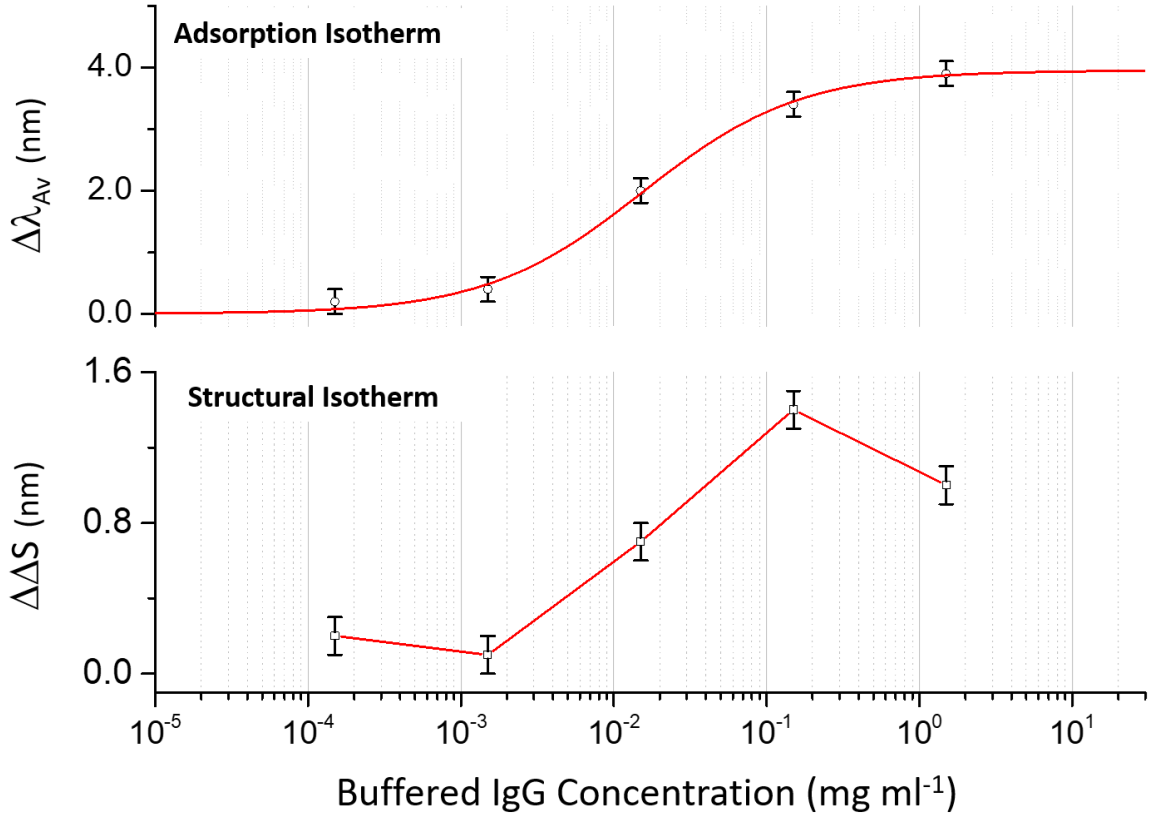

Figure 4.11. Isotherms for Adsorption of IgG onto Chiral Metamaterial. Adsorption isotherm (top) is presented with a Langmuir model fit (red line) quantified by the average wavelength shift $\Delta\lambda_{AV}$ and structural isotherm (bottom) with a guide for the eye added (red line) derived from the asymmetry parameter $\Delta\Delta S$. Both are for buffered IgG solutions. This data is taken from published work by myself and Ryan Tullius, the experiments were performed by Ryan.[91]

A microscopic understanding of structural changes with concentration has previously been proposed based on modelling, suggesting that orientational order increases as the most favourable binding sites are filled.[123] However, as the concentration increases towards saturation, less energetically favourable sites become occupied and the orientations of protein molecules become less uniform leading to decreased structural order. Thus, the findings from the structural isotherm with a maximum point and a decrease are consistent with the microscopic picture.

This understanding of changing structural order with concentration can now be related back to the different models of chiral dielectric used in simulation. It can be assumed based on the microscopic picture discussed that at the highest concentration of 1.5 mg ml^{-1}, the IgG layer has become saturated and completely

disordered, and so conforms to the original isotropic dielectric model used for the chlorophyll and pinene. Reflectivity spectra for the saturation point in experiment and the accompanying isotropic simulation are found in **figure 4.12**. The value of the isotropic optical chirality parameter tensor elements $\tilde{\xi}_{iso}$ have an optimum value of 1.7×10^{-4} for IgG both by experiment and the same method as for the chlorophyll and pinene but using a central wavelength $\lambda_0 = 280$ nm. The asymmetry parameter found in experiment at saturation, 1.00 nm is found to be accurately predicted by the simulation with an isotropic dielectric (0.92 nm).

A second set of reflectivity spectra, this time taken in experiment at the point of highest structural order as dictated by the structural isotherm, is given in **figure 4.13**. For this data set the anisotropic modification to the equations for a chiral dielectric was utilised in the simulations in an attempt to account for the protein layer at this concentration having a specific orientation, assumed to be approximately perpendicular to the gold surface. With the previous estimations of the anisotropic optical chirality parameter tensor elements, $\tilde{\xi}^{aniso}$, being that ξ_{zz}^{ani} is at least ten times the value of both ξ_{xx}^{ani} and ξ_{yy}^{ani} along with **equation 4.12** it is found that ξ_{zz}^{ani}= 5x10^{-4} and ξ_{xx}^{ani} = ξ_{yy}^{ani} = 1x10^{-5} is equivalent to the isotropic case with ξ_{iso} = 1.7×10^{-4}. A value for ξ_{xy}^{ani} can be calculated using the ratio below, where r_{mol} is the size of the protein molecule and D is the spatial extent of the nearfield.[120,126]

$$\frac{\xi_{xy}^{ani}}{\xi_{zz}^{ani}} = \frac{{r_{mol}}^2}{D^2} \qquad [4.18]$$

Equation 4.18 yields a ratio of about 0.1, so that ξ_{xy}^{ani} = 5x10^{-5}. Applying these values again provides simulations with good agreement to experiment, with 1.33 nm being the modelled asymmetry parameter with 1.40 nm obtained in the experiment for highly ordered IgG layers. All asymmetry and chirality parameter values for experiment and simulation for **figures 4.12** and **4.13** are summarised in **table 4-3**. In addition, simulations were run without the non-diagonal elements in the anisotropic tensor, and an asymmetry parameter of 1.30 nm was calculated, suggesting the dipole-quadrupole interaction only has a minor contribution to the asymmetry compared to the dipole-dipole interaction. Based on the form of **equation 4.18**, it might be expected that the quadrupolar elements would have a larger effect if the molecule size was closer to the size of the nearfield or the nanostructure than it is in this case.

The results in **figures 4.12** and **4.13** together reinforce the idea that the coupling between modes in a PIR system, as parameterised by asymmetry in the peak separation, in a chiral plasmonic metamaterial is sensitive to the structural order of a biomolecular layer. This is shown by the increase of chiral asymmetry at points of high orientational uniformity in the protein layer, and is supported by electromagnetic simulation. There is also found to be a lot of versatility in the chiral dielectric tensors in the simulations, being able not only to predict chiral asymmetries for simple organic molecules, but also structural changes in more complex biological systems by the application of the anisotropic tensor.

TABLE 4-3 VALUES FOR COMPONENTS OF THE OPTICAL CHIRALITY PARAMETER TENSOR USED FOR THE ISOTROPIC AND ANISOTROPIC CHIRAL LAYERS IN SIMULATIONS AND THEIR ASSOCIATED ΔΔS VALUES. THE EXPERIMENTAL ΔΔS VALUES FOR BUFFERED IGG ARE INCLUDED. ΔΔS FOR THE ANISOTROPIC LAYER WITH AND WITHOUT THE QUADRUPOLE CONTRIBUTION IS GIVEN FOR THE SIMULATIONS.

	Dipole-dipole (ξ_{xx} , ξ_{yy} , ξ_{zz})	Dipole-quadrupole (ξ_{xy} , ξ_{yx})	$\Delta\Delta S$ (nm) Simulation	$\Delta\Delta S$ (nm) Experiment
Isotropic	$\xi_{xx} = \xi_{yy} = \xi_{zz} = 1.7 \text{ x } 10^{-4}$	$\xi_{xy} = \xi_{yx} = 0$	0.92 ± 0.30	1.00 ± 0.30
Anisotropic	$\xi_{xx} = \xi_{yy} = 1\text{x}10^{-5}$ $\xi_{zz} = 5\text{x}10^{-4}$	$\xi_{xy} = \xi_{yx} = 0$	1.30 ± 0.30	1.40 ± 0.30
	$\xi_{xx} = \xi_{yy} = 1\text{x}10^{-5}$ $\xi_{zz} = 5\text{x}10^{-4}$	$\xi_{xy} = \xi_{yx} = 5\text{x}10^{-5}$	1.33 ± 0.30	1.40 ± 0.30

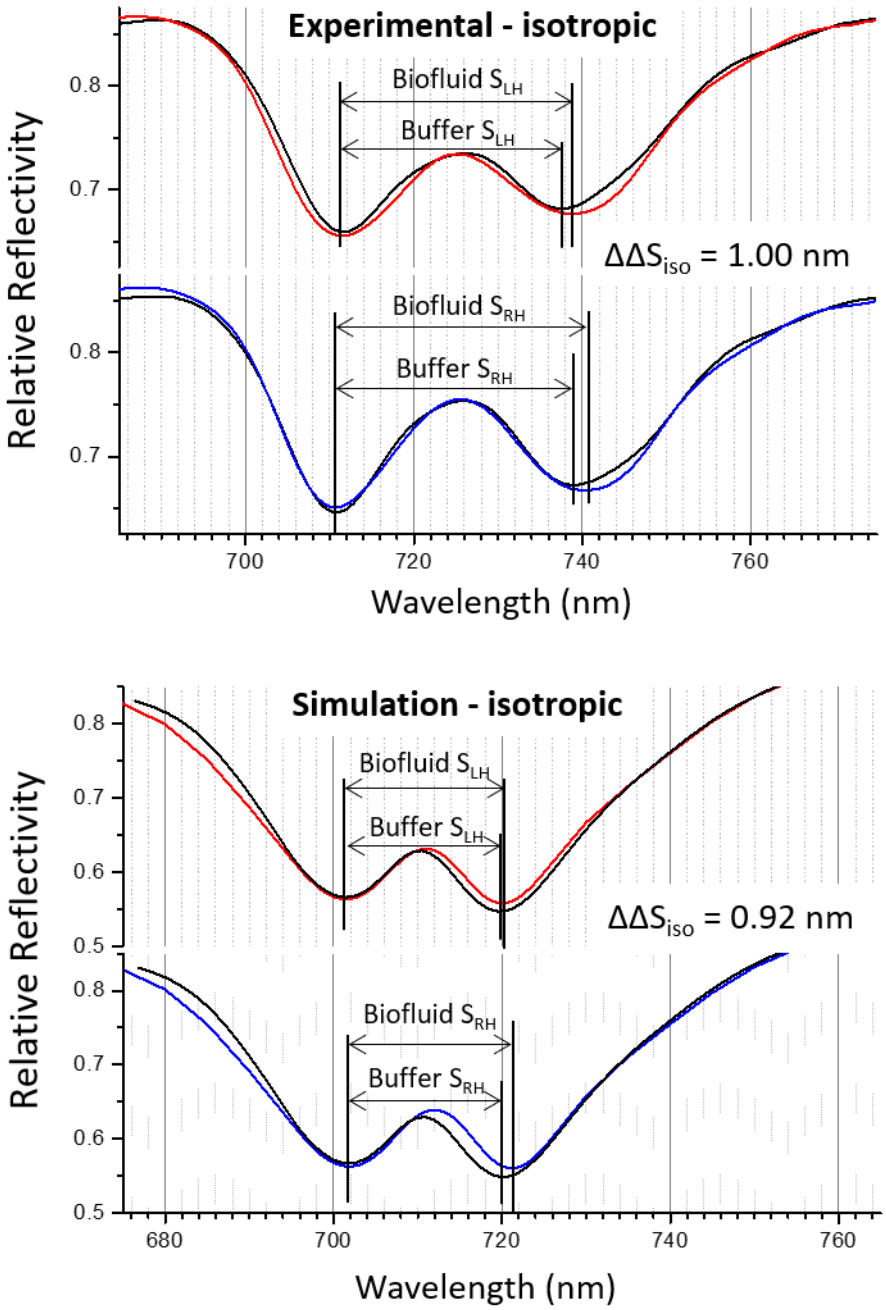

Figure 4.12. Reflectivity for Isotropic, Low Structural Order IgG Layers. Experimental reflectance spectra (top) taken for LH and RH chiral nanostructures with layers of buffer (black lines) and 1.5 mg ml^{-1} buffered IgG (LH structures are red lines, RH are blue) that has saturated, and become disordered. Electromagnetic simulations (bottom) of a system that mimics the experiment, implementing an isotropic chiral dielectric with $\xi_{xx} = \xi_{yy} = \xi_{zz} = 1.7 \times 10^{-4}$ acting as the IgG layer. ΔΔS is 1.00 nm for experiment and 0.92 nm for simulation, as shown on the plots. To aid in the comparison, IgG spectra have been shifted so the first peak overlaps those collected from buffer.

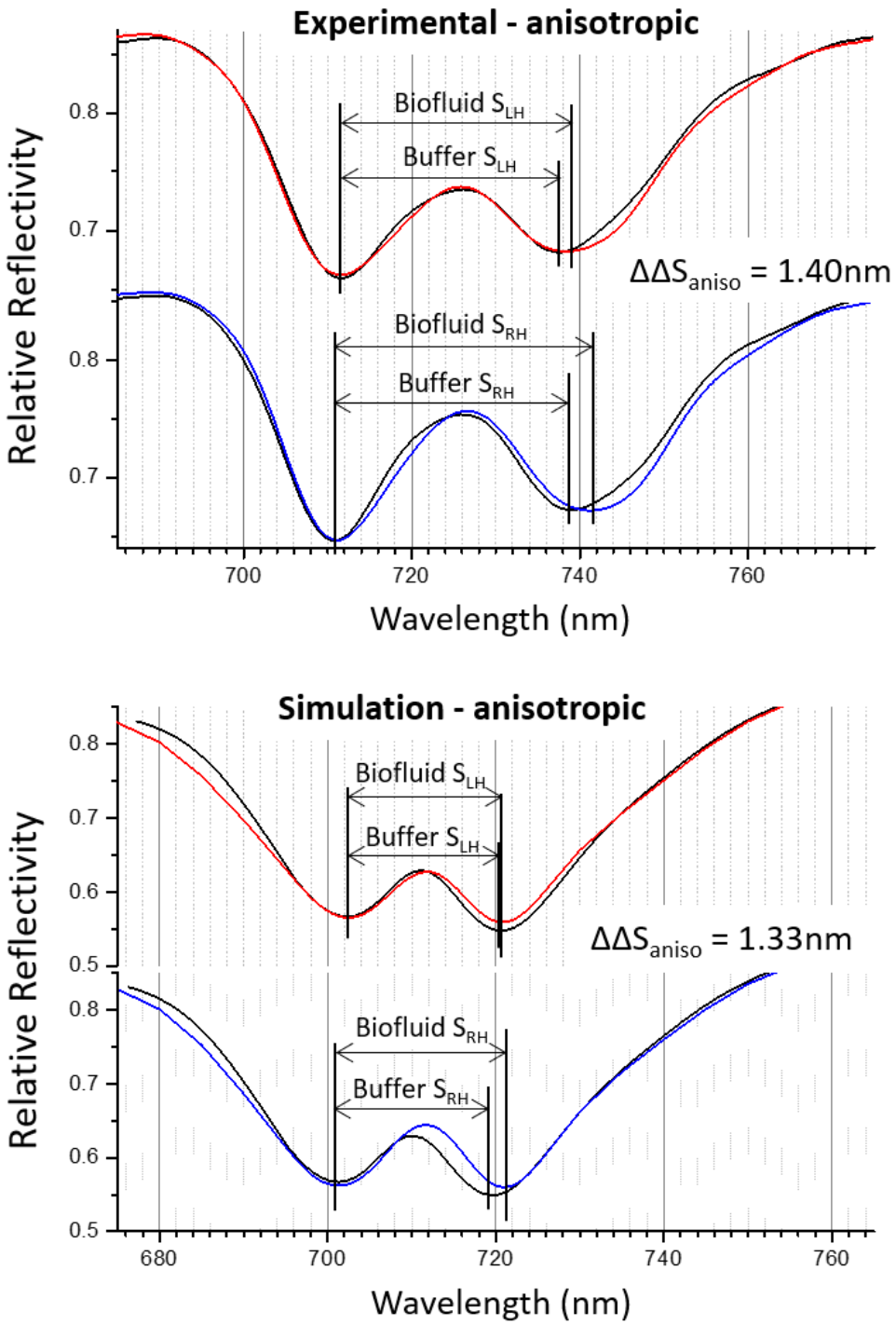

Figure 4.13 . Reflectivity for Anisotropic, High Structural Order IgG Layers. Experimental reflectance spectra (top) taken for LH and RH chiral nanostructures with layers of buffer (black lines) and 1.5 mg ml^{-1} buffered IgG (LH structures are red lines, RH are blue) in a highly ordered structure. Electromagnetic simulations (bottom) of a system that mimics the experiment, implementing an anisotropic chiral dielectric with $\xi_{xx} = \xi_{yy} = 1\text{x}10^{-5}$, $\xi_{zz} = 5\text{x}10^{-4}$ and $\xi_{xy} = \xi_{yx} = 5\text{x}10^{-5}$ acting as the IgG layer. ΔΔS is 1.40 nm for experiment and 1.33 nm for simulation, as shown on the plots. To aid in the comparison, IgG spectra have been shifted so the first peak overlaps those collected from buffer.

Chapter 5 - Building And Testing a Luminescence Microscope

Inorganic films can be used to construct devices with tuneable properties in the same way as has been previously discussed with metals like gold, forming so-called all-dielectric metamaterials.[127] Gold metamaterials leverage the interaction between light incident on the material and its plasmonic resonance, creating strong chiral fields necessary for sensing techniques in the cases where there are chiral nanostructures or chiral light. However, the energy loss inherent in the use of metals for this purpose can hinder their effectiveness, as in the visible region this leads to a broadening of the resonance and an overall lowering of its sensitivity to the local environment. Therefore, it would be beneficial to use materials such as dielectric films that do not suffer from the same ohmic losses as metals, as this would improve the performance of the sensing device. An example of such a material is europium (III) oxide (Eu_2O_3), which has two properties that will be useful for evaluating its usefulness as a sensing platform – it has strong luminescence bands in the visible region, and its emission is exquisitely sensitive to the local environment of the Eu^{3+} ion. These properties lead to this material being used as the dielectric of choice in chapter 6, as a probe of symmetry breaking in inorganic films by chiral perturbations.

In this chapter the process for the construction and testing of a luminescence microscope will be described, following the process as undertaken as a basis for further experimental work in this thesis. The equipment will be tested with samples bearing Eu_2O_3 thin films, which is introduced here as an alternative material to gold in order to form an all-dielectric metamaterial. The injection moulded plastic substrates used previously will enable the gammadion and shuriken shaped nanostructures to be studied as well as the unstructured surface. This setup will then be developed to allow for a variety of experiments to be performed with this microscope, including measurements of the power dependence of the emission and experiments with circularly polarised incident light.

The Microscope

Design Process

A major distinction to be made for the equipment used for the luminescence studies is that here the light source should be monochromatic, as opposed to the broadband

light used for the plasmonic spectroscopy. This is because rather than attempting to find an overlap of the light frequency with that of the excitations in the material to create a resonance, the light needs to be absorbed at a wavelength specific to the dielectric in order for photoluminescence to occur. According to Binnemans, there are strong transitions in the absorption spectra of europium (III) compounds in the near-UV and blue visible regions, particularly at 390-410 nm.[83] As such, a 404 nm diode laser was selected for the excitation of Eu_2O_3. Note that the design wavelength was 404 nm but actual measured wavelength was 407 nm, which is within the error in the specifications. Other than that, a basic version for the microscope was built using the modular cage and rod system available from Thorlabs, Inc with a similar design to that used for the plasmonic spectroscopy experiments. In this case though the laser diode was mounted and affixed directly to the microscope rather than being fed in by fibre optic as for the broadband light source. In addition, it was necessary to add a filter to block out the laser light to make photoluminescence easier to observe. A longpass filter, which is designed to attenuate shorter wavelengths and allow longer wavelengths through, with a cut-on wavelength of 450 nm was added directly beneath the fibre connected to the CCD camera for this purpose. This position was chosen so that the input light could still be seen with the optical camera, allowing the sample to be viewed by eye so the laser spot could be positioned precisely during experiment, either over the nanostructures or a designated spot on the unstructured surface. The polariser that acted as an analyser at the output was set orthogonal to the input linear polarisation, to further reduce the intensity of the background laser light. A diagram and accompanying photograph of the microscope are provided in **figures 5.1(a)** and **5.1(b)** respectively, showing the stage that the samples would be placed on and raised to the working distance of 1 cm to the objective lens.

Alignment

Once this microscope had been physically built, alignment steps were taken to ensure the laser beam would be properly focussed and the beam adjusted to be central within its path to the sample and to the cameras. To ensure the beam was central, a transparent plastic plate with a reticle printed on its surface was placed at the end of the microscope to the right of the lower beamsplitter (see **figure 5.1a**). The laser diode was adjusted in its housing until the beam passed through the centre of the reticle. Pinholes that could be opened and closed in situ were then placed at regular intervals throughout the beam path, to check that if closed the beam would

still reach the sample, both cameras, and the reticle centrally. The lenses located before the lower beamsplitter and the optical camera were also adjusted in position to ensure the light would be properly focussed onto their associated component, each lens having a focal length of 30 mm. Finally, the fibre optic collection point for the light to be directed to the CCD camera (seen in **figure 5.1(b)** at the very top of the microscope column, as a square plate with a small hole at its centre) needed to be adjusted so that as much of the signal was being collected as possible. To do this, the output intensity was lowered using the control unit, by decreasing the driving current of the laser from 180 mA to 120 mA and narrowing the slit at the collection point in the CCD from 300 µm to 50 µm. This allowed the laser peak to be observed with the spectrometer without it saturating. An example of the measured peak is shown in **figure 5.2** for both a fully reflective mirror and the unstructured Eu_2O_3 film. From there, the relative position if the fibre optic plate and the lens beneath it was varied until the maximum signal was achieved. Whilst doing this however, it was noticed that the temperature of the laser (fixed at a desired temperature of 20 °C by a temperature control unit) would fluctuate when the power output was varied by changing the driving current. Given this would result in an unstable intensity and measured signal during experiment, another Glan-Thompson polariser was added just after the laser diode (see in **figure 5.1(a)**). The polariser could be turned to increase or decrease the power reaching the sample without affecting the input polarisation (which is fixed by the secondary input polariser) or the stability of the laser temperature.

PHOTOLUMINESCENCE SPECTROSCOPY OF Eu_2O_3

Eu^{3+} EMISSION SPECTRA

Eu^{3+} can absorb light in the near-UV and visible blue regions of the electromagnetic spectrum as mentioned in the microscope setup, and several emission bands can be seen in the visible and near-IR as a result. In Eu^{3+}, f-f transitions give rise to this emission spectrum and so in Eu_2O_3 being measured there are seven possible transitions $^5D_0 \rightarrow {}^7F_J$ where J ranges from 0 to 6. For brevity from this point on the transitions will be referred to only by their final state, e.g., the $^5D_0 \rightarrow {}^7F_2$ transition will be written only as $^7F_2$.

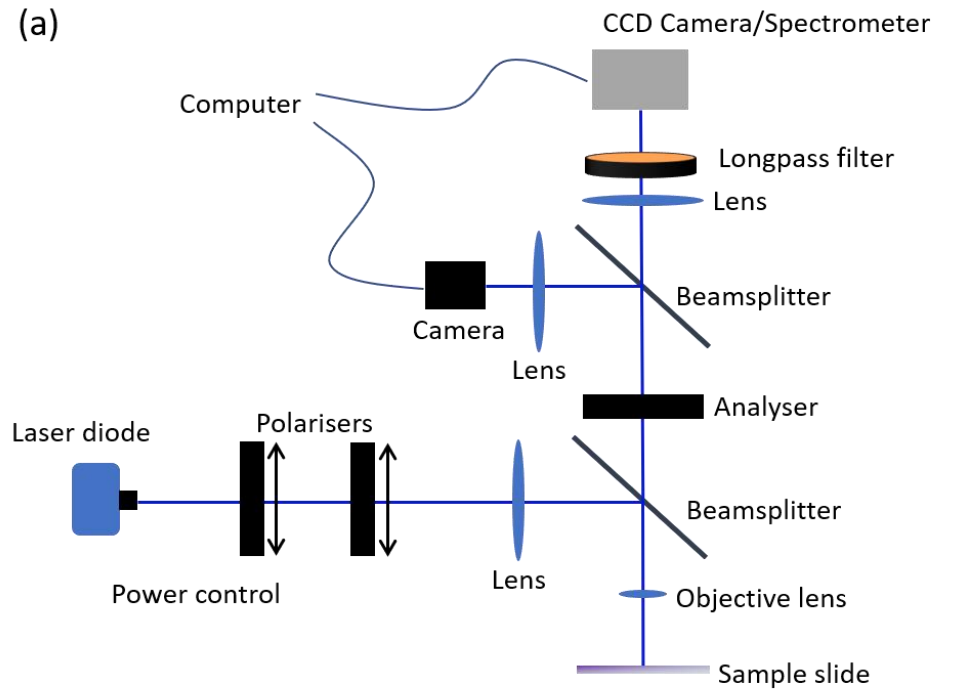

(b)

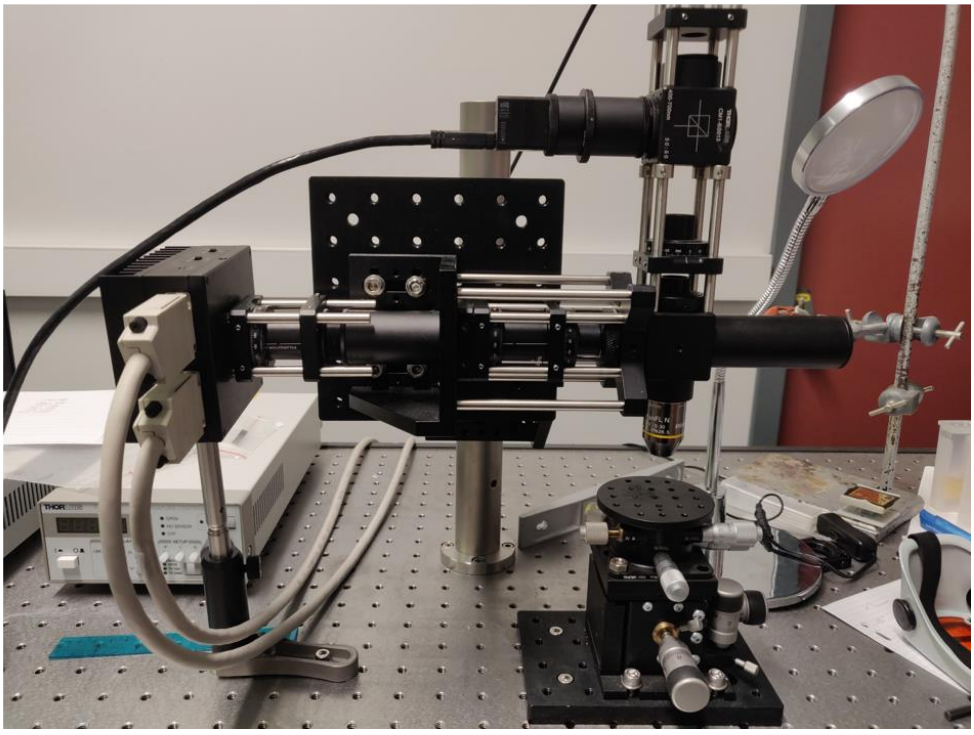

Figure 5.1. General Microscope Setup for Measuring Luminescence of Eu_2O_3. (a) Diagram showing the laser path, including polariser for controlling the input laser power, sample position, filter for removing laser light to collect emissions and the cameras for collecting data and viewing the sample. (b) A photograph of the microscope, showing the circular stage on which the sample is placed at the bottom right with the laser diode in the casing at the left.

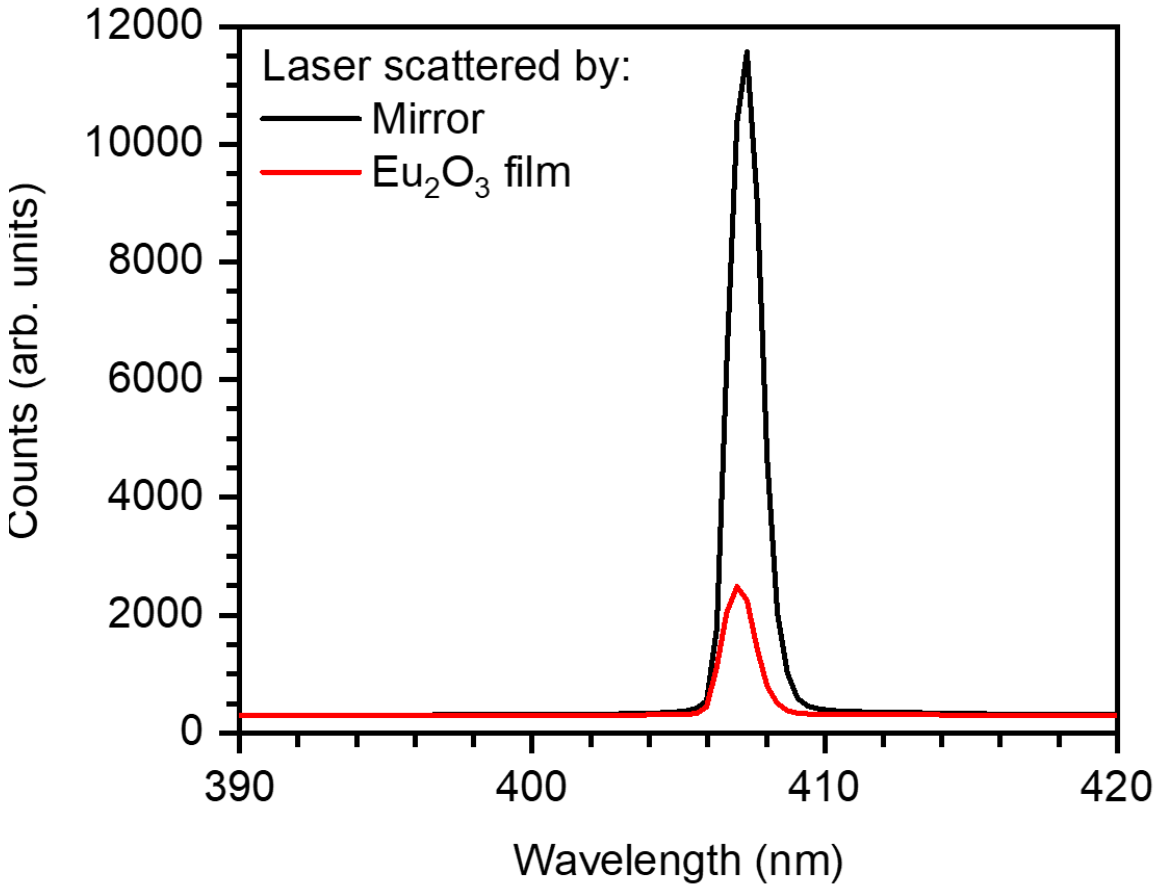

Figure 5.2. 407 nm Diode Laser Peak Collected for Optimising Measurement Signal. This laser scattering peak was measured using both a silver mirror and a Eu_2O_3 sample to reflect it, that could then be used to check that optical components were positioned correctly to collect the highest signal for the given input power.

For several of these transitions, their relative prominence in the emission spectrum is dependent on the co-ordination geometry around the Eu^{3+} ion. This is the primary reason for this material being chosen to be made into a film on the sample, as its luminescence provides a probe for its structure.

Measuring the Luminescence

With the microscope setup built it was ready to be used to measure luminescence of Eu_2O_3 and to optimise the recorded spectra. **Figure 5.3** shows spectra collected on the flat Eu_2O_3 film i.e., that without nanostructures. In both measurements shown in the figure, the $^7F_5$ and $^7F_6$ peaks were not detected with this setup, so these regions are not included. In **figure 5.3(a)** what was measured as a first attempt after the setup is given. It is clearly very noisy resulting in the luminescence peaks not being well-defined, and the intensity counts are quite low.

However, even in this spectrum the $^7F_1$, $^7F_2$ and $^7F_4$ peaks can be distinguished at 590 nm, 615 nm and 705 nm respectively. This experiment was designed with the Eu^{3+} luminescence sensitivity to changes in structural geometry in mind and given that external stimuli applied to the sample might only result in small changes in the spectrum, it would be necessary to improve this signal. This included repeats of the optimisation steps described previously to ensure that on the experimental samples the signal was being optimised, as well as some changes to the spectrum acquisition settings in the software used with the spectrometer. The number of spectra being accumulated for each measurement was increased from 100 to 2400 before being averaged to reduce the noise, and the current driving the laser was set back at 180 mA (equivalent of 18 mW power hitting the sample) to ensure a reasonably high emission signal. The electronic gain of the CCD camera was also set at the highest value possible without the signal becoming saturated. After these steps along with many small adjustments of the sample stage were made (to align the sample properly with the laser beam), the improved spectrum in **figure 5.3(b)** was eventually obtained. The figure has been labelled with the positions of the peaks that were detected. The hypersensitive peak is clear and is again the most intense emission, but the other peaks can be more easily distinguished due to the reduction in the noise. Note that the $^7F_0$ peak is seen in this spectrum as a small shoulder to the left of the $^7F_1$, as they are so close in wavelength they overlap. In addition, the $^7F_3$ peak that is forbidden by the Judd-Ofelt selection rules for Eu^{3+} is observed in this experiment, as the rules are relaxed when the ion is the Eu_2O_3 structure.

With the luminescence for the unstructured Eu_2O_3 film optimised, it was necessary to look at the structured metamaterial film to ensure that luminescence from the nanostructures could be measured with this microscope for future experiment. As with previous chapters, the nanostructures are arranged on the substrate in periodic square arrays, where each array has a length of about 300 μm. Each sample has a variety of different arrays, with a range of nanostructure sizes and interstitial spacings. The nanostructures are formed in the substrate as indentations, such that when the Eu_2O_3 layer is added by pulsed laser deposition on the surface, hybrid structures containing a solid structure with an identically shaped hole above them are formed. An example of this process for a gammadion showing the composition is given in **figure 5.4**.

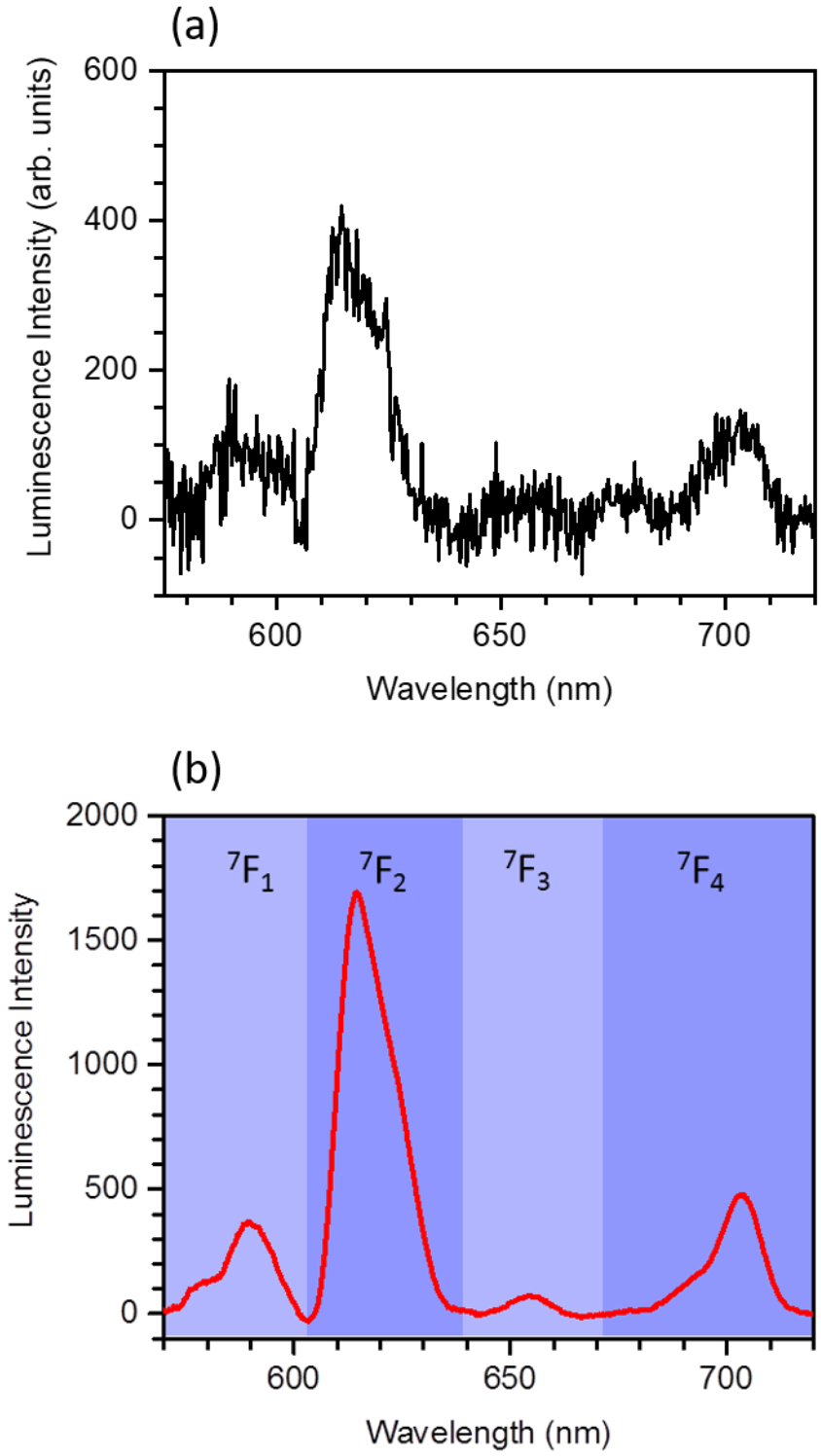

Figure 5.3. Luminescence Spectra of Unstructured Eu_2O_3 film. (a) An early first attempt to measure luminescence and (b) a spectrum collected after the experiment was refined. This shows the $^5D_0 \rightarrow {}^7F_J$ luminescence peaks that are observed in the experiments. The $^7F_0$ peak is not labelled but can be seen as the small shoulder to the left of the $^7F_1$ peak. The $^7F_2$ peak is hypersensitive to its environment and was reliably the most intense peak in the spectra measured. The example given here is for the unstructured Eu_2O_3 film illuminated with linearly polarised light at 407 nm.

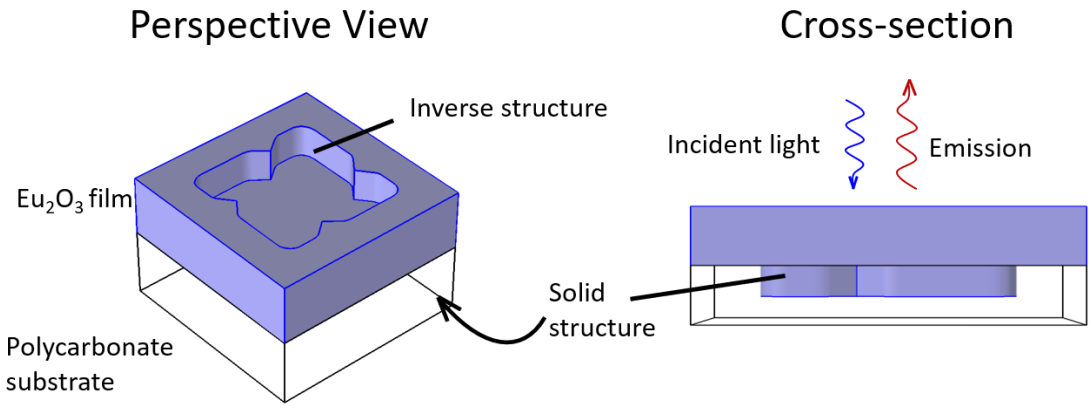

Figure 5.4 Composition of Hybrid Gammadion Nanostructures in a Eu_2O_3 Film. Example of a gammadion shaped hybrid chiral nanostructure fabricated by injection moulding. The indentation for the structure is formed in the polycarbonate substrate. A 150 nm layer of Eu_2O_3 is deposited on the substrate, forming a solid structure in the indentation and the inverse (hole) structure above it. Light is shown to be incident normal to the structure surface and light emitted at the normal is what is measured.

A scanning electron microscope (SEM) image of the array of 400x300 gammadion nanostructures (meaning 400 nm structure width and 300 nm interstitial spacing between the structures in the array, horizontally and vertically) is shown in **figure 5.5(a)**. The image was collected from a polycarbonate template slide coated in gold, identical to the slides used for the Eu_2O_3 experiments, as the surface must be conductive for SEM. Before recording any luminescence spectra for the nanostructures, it was noticed that when the arrays of structures were illuminated with the laser, the light scattered throughout the sample slide creating internal reflection patterns. Photographs were taken to document this curiosity, an example of which is given in **figure 5.5(b)**. A filter was used to remove the blue laser light leaving just the background emissions from the polycarbonate (yellow) and the red dots at the top surface from the thin Eu_2O_3 layer. These polycarbonate peaks are observed in the spectra in the region 500-560 nm, but are removed as a background in the presented spectra so as not to interfere with the measurements of the Eu_2O_3. The luminescence spectrum for the 400x300 gammadion array was measured and is shown in **figure 5.6**, using the same techniques to gain a high-quality spectrum as were used for the spectrum in **figure 5.3(b).** This spectrum has the same general trends as that for the unstructured surface, with the hypersensitive peak being the most intense and the normally forbidden $^7F_3$ peak being present weakly.

(a) 400x300 Nanostructured film

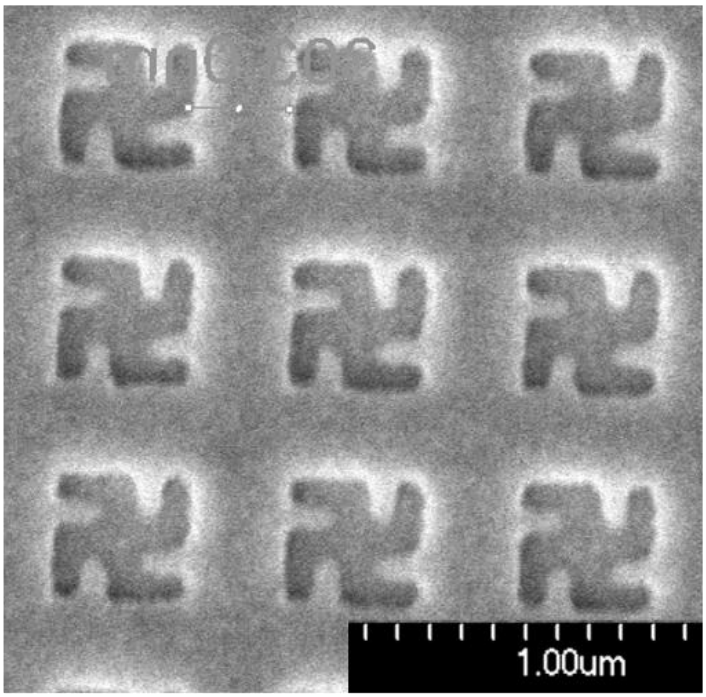

(b) Sample Luminescence

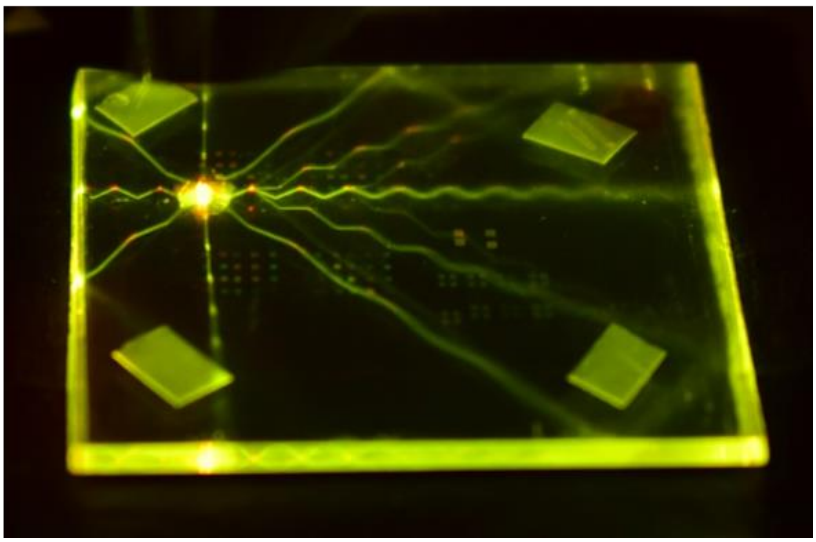

Figure 5.5 Nanostructured Eu_2O_3 Films for Luminescence Experiments. (a) A SEM image of part of an array of gammadion nanostructures. The label of 400x300 refers to the dimensions of the array, i.e., the gammadions have a width of 400 nm and the array has an interstitial spacing of 300 nm. A 1µm scalebar is included. (b) A photograph taken of the sample slide under illumination with the 407 nm laser on an array of gammadions, with a filter lens to remove the blue laser light. When the light is scattered from a nanostructure array, internal reflections in the sample slide and the background emissions from the polycarbonate can be seen. At the peaks of these reflections there are red dots, which are emissions from the thin layer of Eu_2O_3 at the top surface of the substrate.

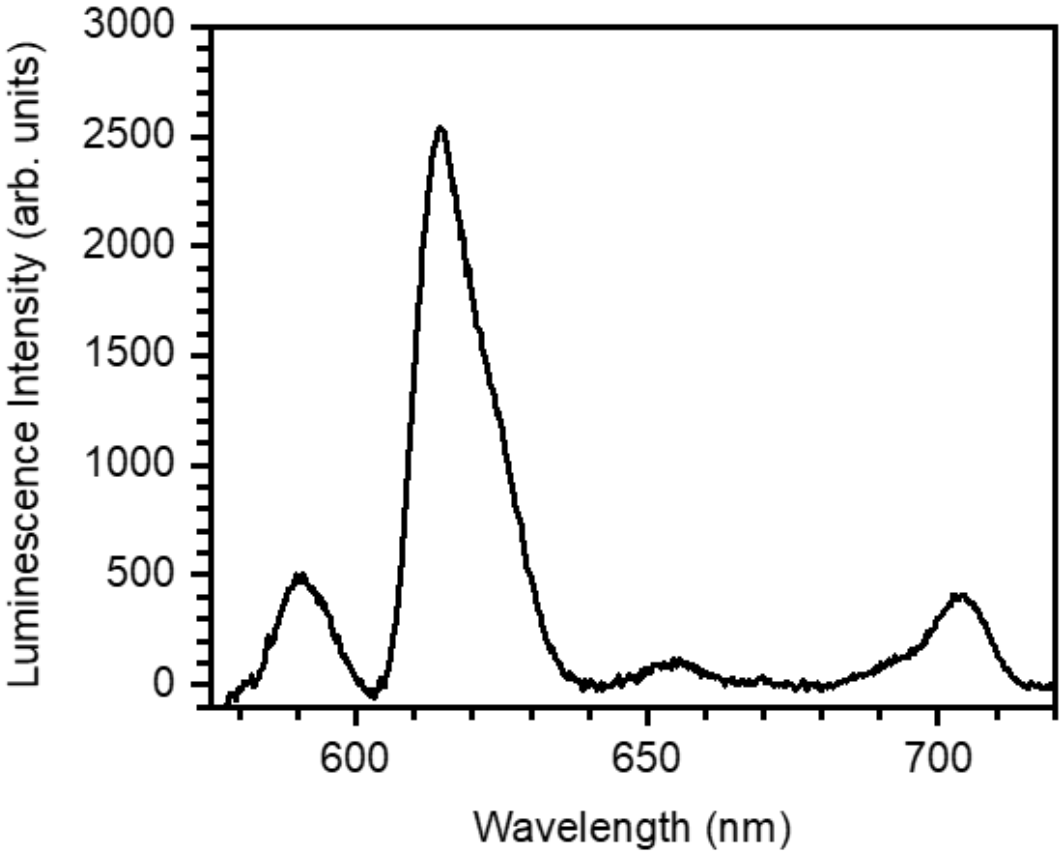

Figure 5.6. Luminescence of Eu_2O_3 Nanostructure Array. The luminescence spectrum here is measured for the 400x300 gammadion nanostructure array (400 nm structure diameter, 300 nm interstitial spacing) pictured in figure 5.5(a) under illumination with linearly polarised light at 407 nm.

However, slight differences in the relative intensities of the peaks can be seen between films with and without nanostructures. For example, for the gammadions the $^7F_4$ peak (705 nm) is lower in intensity compared to the insensitive $^7F_1$ peak than it is for the flat film, whereas the hypersensitive $^7F_2$ peak is more intense comparatively. This is a good first indication of the sensitivity of the luminescence to larger scale structure, and confirms that the nanostructures can indeed be included in further experimental work.

Power Control Setup

It was desirable with this equipment to have the ability to control the power of the input laser, both for studies on the effect of laser power on any structural changes in the sample and for easier viewing of the surface in the optical camera. In early trials in measuring the emissions from the sample the power was changed often

using the variable current from the external controller for the laser diode, for optimising the operation power and to mitigate the chance of damage to the sample. However, it was noticed that changing the power in this manner would cause the laser output to temporarily lose stability, seen as fluctuations in its temperature and emission output from the spectrometer. The temperature stabilising again could take a long time, an hour or even longer. In order to remove this problem, as already mentioned, the secondary polariser was added at the input, and sits before the birefringent plate that determines the input polarisation. By rotating this secondary polariser, the laser power reaching the sample and cameras could be modulated without destabilising the laser. As a final step in preparing the equipment for experiment, a series of measurements were taken to determine how the power changes with the angle of the power control polariser with respect to the other input polariser. Power was measured in the position at which the samples would be placed during experiment. This could then be converted into a percentage of the maximum input power of 18mW at that position. It is known that light intensity I on passing through a polariser is given by Malus' Law, $I = I_0 \cos^2 \theta$, where I_0 is the initial intensity and θ is the angle of the polariser plane with respect to the light polarisation. As the laser light leaving the diode is elliptically polarised and so itself has a direction, with this setup the expectation then is that there would be a $\cos^4 \theta$ intensity profile. The power measurements taken at each angle, where 0° is the polariser planes set parallel to each other, are given in **figure 5.7** along with a $\cos^4 \theta$ fit to that data. There is clearly good agreement between the fit and the collected data, confirming this as mathematical description of the how the laser power reaching the sample changes as the power control polariser is rotated.

In this chapter a microscope was built, tested and aligned, and has been shown to be viable for measuring the luminescence of Eu_2O_3 films. This has been demonstrated for both unstructured and nanostructured films, with improvements made to measured signals ensuring small changes to the luminescence in subsequent experiments can be detected. This work can now be progressed in order to determine if Eu_2O_3 luminescence can be used as a probe of changes in local co-ordination in an inorganic material under chiral perturbation, using this microscope to perform the necessary experiments.

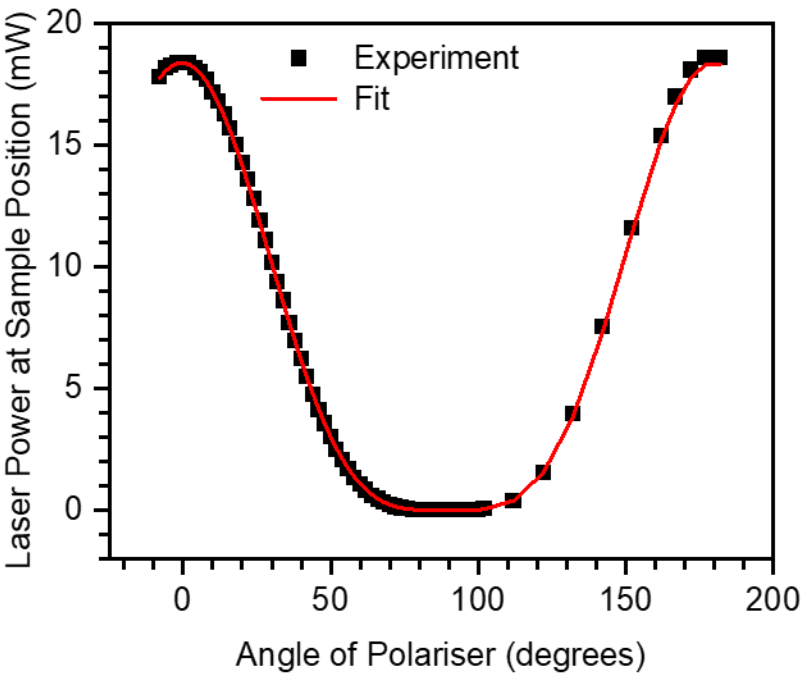

Figure 5.7. Power Control of Laser using Two Polarisers. Black dots represent experimental data for the laser power at varying relative angles between the two input polarisers in the luminescence microscope. The red line is a $\cos^4\theta$ fit to this data showing good agreement.

Chapter 6 - Luminescence Probes Symmetry Breaking In Eu_2O_3

The chemical environment of a metal ion modifies its properties, causing changes to its symmetry, electronic arrangement and magnetic character. The symmetry environment contributes to the function of inorganic materials, which can be tuned by choice of ligand or crystal structure bound to the constituent metal ions. For example, the Jahn-Teller distortion causes often octahedral complexes that might be expected to behave as if they were centrosymmetric to display reduced symmetry and energy. The ability to dynamically drive changes of symmetry in established inorganic materials can be achieved by putting strain on a lattice, physically altering the relative positions of the atoms in the material. This allows for the creation of devices that exploit these symmetry changes, such as the reconfigurable optical components described by Wang et al.[128] This strain can be created in a controlled way through light-matter interactions, enabling access to states of matter that could not be otherwise achieved by thermodynamic processes. However, these processes require highly specific properties to work, limiting the range of materials whose symmetry can be manipulated this way.

In this chapter, an attempt will be made to find more a generic technique to modify symmetry in an inorganic film that does not rely on phase transitions, bound chemical layers or other specific material properties. To do this, the nature of the interaction between light with angular momentum and an inorganic material, namely Europium (III) Oxide, will be investigated. Much of the work in this chapter is contained in a manuscript that has been published by Nature Communications entitled “Controlling the symmetry of inorganic ionic nanofilms with optical chirality”.[129] The author would like to thank Stephen Barnett, Sonja Franke-Arnold, Frances Crimin and Jörg Götte from the School of Physics and Astronomy, University of Glasgow, for work on the derivation of the continuity equation for optical chirality.

Spin and Conservation of Optical Chirality

It is well known that light-matter interactions involving chiral metamaterials can result in changes to the chiral nearfields and light polarization as discussed earlier in this work, as well as giving enhanced CD, circularly polarized luminescence and optical

rotatory dispersion.[130–133] In 1936 Beth demonstrated the ability of CPL to impart a torque on a birefringent material suspended in air, such that the angular momentum gained by that wave plate was offset by a change in the handedness of the CPL.[134]

In contrast to atomic length scales, spin angular momentum can be transferred in longer dimensions, manipulating objects by imparting a sense of physical twist. CPL can induce of change in angular momentum in materials with which it interacts via the application of a torque, as is seen for optical tweezers and other opto-mechanical devices.[135–137] CPL can also cause symmetry reduction in photoactive materials by the manipulation of chemical environments, in cases where a component of the system is either chiral or has the potential to be.[138–140] These processes can be thought of as the twisting of the light being transferred to another material, breaking its symmetry, a phenomenon associated with the chirality of CPL – its sense of handedness. This movement in a material and the torque which causes it result from the intrinsic spin angular momentum of CPL being transferred to it, as described in the Beth experiment. However, the torque that can be imposed by light with angular momentum is much too weak to physically distort chemical bonds and break symmetry in that manner. As such chiral light has found difficulty being established as a tool for breaking chemical symmetry in materials with no intrinsic chirality. In order understand any effects that occur in the proceeding experiments in this work, it is important that the transfer mechanism for optical chirality in light-matter interactions is properly discussed.

In free space optical chirality density, like energy, must be conserved.[60,141] When light-matter interactions are considered, then it is possible for there to arise sources and sinks of optical chirality. Unlike energy, optical chirality density is pseudoscalar, given its sense of handedness confers meaning on its direction, and so it is the interfaces between materials where light reflects and refracts that act as these sources and sinks. From this analogy with energy, it is pertinent to construct a continuity equation describing the conservation and exchange of optical chirality, in which the interfacial interactions are taken into account. As such, in the following section a derivation of a continuity equation is presented for optical chirality density in the presence of a medium, i.e., specifically not in free space. A continuity expression has previously been described by Poulikakos *et al*, however here the equation is derived from first principles rather than by analogy to energy and

Poynting's theorem. In this case the chirality is not split into electric and magnetic parts; the complex electric permittivity and magnetic permeability are worked from directly and splitting them is not required.[141]

The Continuity Equation for Optical Chirality

To begin with, the optical chirality density *C* is used to quantify the spin angular momentum in the system, and is written in **equation 6.1** in a more general from than how it has been used previously in this thesis. Here, $\boldsymbol{D}$ is the electric displacement field, $\boldsymbol{B}$ is the magnetic flux density and $\dot{\boldsymbol{D}}$ and $\dot{\boldsymbol{B}}$ are the time-derivatives of the two fields respectively.

$$C = \frac{1}{2}\left(\boldsymbol{B}\cdot\dot{\boldsymbol{D}} - \boldsymbol{D}\cdot\dot{\boldsymbol{B}}\right) \quad [6.1]$$

To use substitutions from Maxwell's equations (that are restated in **equations 6.2-6.5**), this expression for *C* is then differentiated with respect to time, in the absence of charges and currents, resulting in **equation 6.6.**

$$\nabla\cdot\vec{D} = \rho \quad [6.2]$$

$$\nabla\cdot\vec{B} = 0 \quad [6.3]$$

$$\nabla\times\vec{E} = -\frac{\partial\vec{B}}{\partial t} \quad [6.4]$$

$$\nabla\times\vec{H} = \vec{J} + \frac{\partial\vec{D}}{\partial t} \quad [6.5]$$

$$\dot{C} = \frac{1}{2}\left(\boldsymbol{B}\cdot\nabla\times\dot{\boldsymbol{H}} + \boldsymbol{D}\cdot\nabla\times\dot{\boldsymbol{E}}\right) \quad [6.6]$$

From here, a few triple product identities are required to construct the continuity equation. These are given in **equations 6.7** and **6.8** below, and have been modified to include the parameters being used here. Note that the third term in each of these can be found in **equation 6.6**. So, by combining **equations 6.6-6.8**, an initial form of the continuity equation for optical chirality is found, **equation 6.9**, of which the left-hand side is assigned as the chirality flux, and the right as chirality source/sink terms.

$$\nabla \cdot \left(\boldsymbol{D} \times \dot{\boldsymbol{E}}\right) = \dot{\boldsymbol{E}} \cdot (\boldsymbol{\nabla} \times \boldsymbol{D}) - \boldsymbol{D} \cdot \left(\boldsymbol{\nabla} \times \dot{\boldsymbol{E}}\right), \quad [6.7]$$

$$\nabla \cdot \left(\boldsymbol{B} \times \dot{\boldsymbol{H}}\right) = \dot{\boldsymbol{H}} \cdot (\boldsymbol{\nabla} \times \boldsymbol{B}) - \boldsymbol{B} \cdot \left(\boldsymbol{\nabla} \times \dot{\boldsymbol{H}}\right), \quad [6.8]$$

$$\dot{C} - \frac{1}{2}\nabla \cdot \left[\dot{\boldsymbol{E}} \times \boldsymbol{D} + \dot{\boldsymbol{H}} \times \boldsymbol{B}\right] = \frac{1}{2}\left[\dot{\boldsymbol{E}} \cdot (\boldsymbol{\nabla} \times \boldsymbol{D}) + \dot{\boldsymbol{H}} \cdot (\boldsymbol{\nabla} \times \boldsymbol{B})\right] \quad [6.9]$$

To justify this assignment, an understanding of the material contribution must be considered. Given that this equation will deal with interaction between light and materials at interfaces, a complex permittivity, $\varepsilon = \varepsilon' + i\varepsilon''$, and complex permeability, $\mu = \mu' + i\mu''$ are necessary. These properties are assumed to be independent of frequency, as they will vary very little over the sufficiently narrow band incident light, but are otherwise quite general. With these in mind, the electromagnetic fields that are of interest here can be written as combinations of a field of that type and its complex conjugate:

$$\boldsymbol{E} = (\boldsymbol{\mathcal{E}} + \boldsymbol{\mathcal{E}}^*) \quad [6.10]$$

$$\boldsymbol{H} = (\boldsymbol{\mathcal{H}} + \boldsymbol{\mathcal{H}}^*) \quad [6.11]$$

$$\boldsymbol{D} = (\varepsilon\, \boldsymbol{\mathcal{E}} + \varepsilon^* \boldsymbol{\mathcal{E}}^*) \quad [6.12]$$

$$\boldsymbol{B} = (\mu \boldsymbol{\mathcal{H}} + \mu^* \boldsymbol{\mathcal{H}}^*) \quad [6.13]$$

These fields can then be substituted into the flux term from **equation 6.9** (the other term on the left-hand side and the divergence of the bracketed term will be dealt with later) giving **equation 6.14,**

$$\frac{1}{2}\left[\dot{\boldsymbol{E}} \times \boldsymbol{D} + \dot{\boldsymbol{H}} \times \boldsymbol{B}\right] = \frac{1}{2}\left[\left(\dot{\boldsymbol{\mathcal{E}}} + \dot{\boldsymbol{\mathcal{E}}}^*\right) \times (\varepsilon\, \boldsymbol{\mathcal{E}} + \varepsilon^* \boldsymbol{\mathcal{E}}^*) + \left(\dot{\boldsymbol{\mathcal{H}}} + \dot{\boldsymbol{\mathcal{H}}}^*\right) \times (\mu \boldsymbol{\mathcal{H}} + \mu^* \boldsymbol{\mathcal{H}}^*)\right], \quad [6.14]$$

Adding in the approximation that each of the field components $\boldsymbol{\mathcal{E}}, \boldsymbol{\mathcal{H}}$ and their complex conjugates vary with time according to an exponential $e^{-i\omega t}$ such that, for example $\dot{\boldsymbol{\mathcal{E}}} = -i\omega \boldsymbol{\mathcal{E}}$**,** and so on along with the previously mentioned narrow-band light assumption (i.e. $\Delta\omega << \omega$), **equation 6.14** can be modified to the give **equation 6.15** by the process shown, starting from the right-hand side of **6.14**.

$$\frac{1}{2}[(-i\omega\boldsymbol{\mathcal{E}} + i\omega\boldsymbol{\mathcal{E}}^*) \times (\varepsilon\,\boldsymbol{\mathcal{E}} + \varepsilon^*\boldsymbol{\mathcal{E}}^*) + (-i\omega\boldsymbol{\mathcal{H}} + i\omega\boldsymbol{\mathcal{H}}^*) \times (\mu\boldsymbol{\mathcal{H}} + \mu^*\boldsymbol{\mathcal{H}}^*)],$$

$$= \frac{1}{2}[-i\omega\varepsilon^*\boldsymbol{\mathcal{E}} \times \boldsymbol{\mathcal{E}}^* - i\omega\varepsilon\boldsymbol{\mathcal{E}} \times \boldsymbol{\mathcal{E}}^* - i\omega\mu^*\boldsymbol{\mathcal{H}} \times \boldsymbol{\mathcal{H}}^* - i\omega\mu\boldsymbol{\mathcal{H}} \times \boldsymbol{\mathcal{H}}^*],$$

$$= \frac{-i\omega}{2}[(\varepsilon^* + \varepsilon)\boldsymbol{\mathcal{E}} \times \boldsymbol{\mathcal{E}}^* + (\mu^* + \mu)\boldsymbol{\mathcal{H}} \times \boldsymbol{\mathcal{H}}^*] \quad \Rightarrow$$

$$\frac{1}{2}\left[\dot{\boldsymbol{E}} \times \boldsymbol{D} + \dot{\boldsymbol{H}} \times \boldsymbol{B}\right] = -i\omega[\varepsilon'(\boldsymbol{\mathcal{E}} \times \boldsymbol{\mathcal{E}}^*) + \mu'(\boldsymbol{\mathcal{H}} \times \boldsymbol{\mathcal{H}}^*)], \qquad [6.15]$$

Thus, given that only real parts of the permittivity and permeability are found in **6.15**, this part from the left side of **6.9** is justifiably designated a flux as there is no connection to losses (i.e., the imaginary parts of ε and μ), and so will remain constant for lossless materials. Following this, a similar justification must be found to call the right side of **equation 6.9** source/sink terms. By the application of **equations 6.10-6.13** and the approximation for the time derivatives mentioned, the right side of **6.9** can be written as shown in **equation 6.16**, and expanded to the form in **equation 6.17**.

$$\frac{1}{2}[(-i\omega\boldsymbol{\mathcal{E}} + i\omega\boldsymbol{\mathcal{E}}^*) \cdot \boldsymbol{\nabla} \times (\varepsilon\,\boldsymbol{\mathcal{E}} + \varepsilon^*\boldsymbol{\mathcal{E}}^*) + (-i\omega\boldsymbol{\mathcal{H}} + i\omega\boldsymbol{\mathcal{H}}^*) \cdot \boldsymbol{\nabla} \times (\mu\boldsymbol{\mathcal{H}} + \mu^*\boldsymbol{\mathcal{H}}^*)] \qquad [6.16]$$

$$= \frac{1}{2}[(-i\omega\boldsymbol{\mathcal{E}} + i\omega\boldsymbol{\mathcal{E}}^*) \cdot (\varepsilon\,\boldsymbol{\nabla} \times \boldsymbol{\mathcal{E}} - \boldsymbol{\mathcal{E}} \times \boldsymbol{\nabla}\varepsilon + \varepsilon^*\boldsymbol{\nabla} \times \boldsymbol{\mathcal{E}}^* - \boldsymbol{\mathcal{E}}^* \times \boldsymbol{\nabla}\varepsilon^*) +$$

$$+ (-i\omega\boldsymbol{\mathcal{H}} + i\omega\boldsymbol{\mathcal{H}}^*) \cdot (\mu\boldsymbol{\nabla} \times \boldsymbol{\mathcal{H}} - \boldsymbol{\mathcal{H}} \times \boldsymbol{\nabla}\mu + \mu^*\boldsymbol{\nabla} \times \boldsymbol{\mathcal{H}}^* - \boldsymbol{\mathcal{H}}^* \times \boldsymbol{\nabla}\mu^*)] \qquad [6.17]$$

To continue, the terms in **6.17** containing only the curls of $\boldsymbol{\mathcal{E}}$ and $\boldsymbol{\mathcal{H}}$ and their complex conjugates are considered, taking into account that, as a result of Maxwell's equations, the expressions $\nabla \times \boldsymbol{\mathcal{E}} = i\omega\boldsymbol{\mathcal{B}} = i\omega\mu\boldsymbol{\mathcal{H}}$ and $\nabla \times \boldsymbol{\mathcal{H}} = -i\omega\boldsymbol{\mathcal{D}} = -i\omega\varepsilon\boldsymbol{\mathcal{E}}$ are true given the approximations already taken**.** Thus, these terms can be written as

$$(-i\omega\boldsymbol{\mathcal{E}} + i\omega\boldsymbol{\mathcal{E}}^*) \cdot (\varepsilon\,\boldsymbol{\nabla} \times \boldsymbol{\mathcal{E}} + \varepsilon^*\boldsymbol{\nabla} \times \boldsymbol{\mathcal{E}}^*) + (-i\omega\boldsymbol{\mathcal{H}} + i\omega\boldsymbol{\mathcal{H}}^*) \cdot (\mu\boldsymbol{\nabla} \times \boldsymbol{\mathcal{H}} + \mu^*\boldsymbol{\nabla} \times \boldsymbol{\mathcal{H}}^*)$$

$$= (-i\omega\boldsymbol{\mathcal{E}} + i\omega\boldsymbol{\mathcal{E}}^*) \cdot (i\omega\varepsilon\mu\boldsymbol{\mathcal{H}} - i\omega\varepsilon^*\mu^*\boldsymbol{\mathcal{H}}^*) + (-i\omega\boldsymbol{\mathcal{H}} + i\omega\boldsymbol{\mathcal{H}}^*) \cdot (-i\omega\varepsilon\mu\boldsymbol{\mathcal{E}} + i\omega\varepsilon^*\mu^*\boldsymbol{\mathcal{E}}^*)$$

$$= \omega^2(\varepsilon\mu - \varepsilon^*\mu^*)(\boldsymbol{\mathcal{E}} \cdot \boldsymbol{\mathcal{H}}^* - \boldsymbol{\mathcal{E}}^* \cdot \boldsymbol{\mathcal{H}})$$

$$= 2i\omega^2(\varepsilon'\mu'' + \varepsilon''\mu')(\boldsymbol{\mathcal{E}} \cdot \boldsymbol{\mathcal{H}}^* - \boldsymbol{\mathcal{E}}^* \cdot \boldsymbol{\mathcal{H}}) \qquad [6.18]$$

Unlike the flux part of **equation 6.9**, this part does include the imaginary parts of the permittivity and permeability, and so is considered to be the term associated with loss in the material – the chirality sink. The remaining terms in **equation 6.17** are those containing the gradients of ε and μ and their complex conjugates. In a similar fashion, they can be simplified (here the scalar triple product is used) to give **equation 6.19.**

$$(-i\omega\boldsymbol{\mathcal{E}} + i\omega\boldsymbol{\mathcal{E}}^*)\cdot(-\boldsymbol{\mathcal{E}}\times\boldsymbol{\nabla}\varepsilon - \boldsymbol{\mathcal{E}}^*\times\boldsymbol{\nabla}\varepsilon^*) + (-i\omega\boldsymbol{\mathcal{H}} + i\omega\boldsymbol{\mathcal{H}}^*)\cdot(-\boldsymbol{\mathcal{H}}\times\boldsymbol{\nabla}\mu - \boldsymbol{\mathcal{H}}^*\times\boldsymbol{\nabla}\mu^*)$$

$$= +i\omega(\boldsymbol{\mathcal{E}}\times\boldsymbol{\mathcal{E}}^*)\cdot\boldsymbol{\nabla}\varepsilon^* - i\omega(\boldsymbol{\mathcal{E}}^*\times\boldsymbol{\mathcal{E}})\cdot\boldsymbol{\nabla}\varepsilon + i\omega(\boldsymbol{\mathcal{H}}\times\boldsymbol{\mathcal{H}}^*)\cdot\boldsymbol{\nabla}\mu^* - i\omega(\boldsymbol{\mathcal{H}}^*\times\boldsymbol{\mathcal{H}})\cdot\boldsymbol{\nabla}\mu$$

$$= +i\omega(\boldsymbol{\mathcal{E}}\times\boldsymbol{\mathcal{E}}^*)\cdot\boldsymbol{\nabla}(\varepsilon^* + \varepsilon) + i\omega(\boldsymbol{\mathcal{H}}\times\boldsymbol{\mathcal{H}}^*)\cdot\boldsymbol{\nabla}(\mu^* + \mu)$$

$$= i2\omega[\nabla\varepsilon'\cdot(\boldsymbol{\mathcal{E}}\times\boldsymbol{\mathcal{E}}^*) + \nabla\mu'\cdot(\boldsymbol{\mathcal{H}}\times\boldsymbol{\mathcal{H}}^*)] \qquad [6.19]$$

Here only the gradients of the real parts of the permittivity and permeability are included. However, interfaces can act as sources of chirality even in this case as the signs of helicity and hence chirality change upon reflection. This part of **equation 6.9** can therefore be thought of as a description of the exchange of chirality between light and materials at an interface where the real parts of the permittivity or permeability changes, and will be referred to from this point as the 'interface-exchange' term (*IE*). This is in contrast to the optical helicity which is conserved when interaction at an interface preserves the duality symmetry of the free electromagnetic field.[142,143] For nonmagnetic or weakly magnetic systems such as that being used in this chapter, $\nabla\mu'$ can be ignored, with the focus put on the electric properties.

Putting this all together then, the source/sink on the right-hand side of **equation 6.9** can be written as

$$i\omega^2(\boldsymbol{\mathcal{E}}\cdot\boldsymbol{\mathcal{H}}^* - \boldsymbol{\mathcal{E}}^*\cdot\boldsymbol{\mathcal{H}})(\mu'\varepsilon'' - \mu''\varepsilon') + i\omega[\nabla\varepsilon'\cdot(\boldsymbol{\mathcal{E}}\times\boldsymbol{\mathcal{E}}^*) + \nabla\mu'\cdot(\boldsymbol{\mathcal{H}}\times\boldsymbol{\mathcal{H}}^*)], \qquad [6.20]$$

and so, by combining equations **6.9**, **6.15** and **6.20** together, the full narrow bandwidth optical chirality continuity equation can be found, given by

$$\dot{C} - i\omega\nabla\cdot\underbrace{[\varepsilon'(\boldsymbol{\mathcal{E}}\times\boldsymbol{\mathcal{E}}^*) + \mu'(\boldsymbol{\mathcal{H}}\times\boldsymbol{\mathcal{H}}^*)]}_{\text{chirality flux}} = +i\omega^2\underbrace{(\boldsymbol{\mathcal{E}}\cdot\boldsymbol{\mathcal{H}}^* - \boldsymbol{\mathcal{H}}\cdot\boldsymbol{\mathcal{E}}^*)(\mu'\varepsilon'' + \varepsilon'\mu'')}_{\text{loss term}} + \qquad [6.21]$$

$$i\omega\underbrace{[(\nabla\varepsilon')\cdot(\boldsymbol{\mathcal{E}}\times\boldsymbol{\mathcal{E}}^*) + (\nabla\mu')\cdot(\boldsymbol{\mathcal{H}}\times\boldsymbol{\mathcal{H}}^*)]}_{\text{interface-exchange term }(IE)},$$

in which the identities of each part of the equation are shown. This provides a mathematical description of how chiral light interacts with matter, and will be used

in rationalising experimental results. The *IE* term tells us that for CPL propagating through a film with two interfaces with unequal gradients in the permittivity and/or permeability there can be a net non-dissipative transfer of chirality to the medium.

Results and Discussion

Unstructured Inorganic Surface

To begin with, the simplest form of chiral light will be used to excite the samples – CPL. Experimental work in this chapter involves luminescence spectroscopy of 150 nm thick europium (III) oxide (Eu_2O_3) films on plastic substrates. This section will be concerned only with the regions of solid, unstructured Eu_2O_3, rather than nanostructures. The nanofilms were illuminated with monochromatic laser light at 404 nm, which was filtered allowing the emissions from the Eu ions to be collected by a CCD camera. A diagram of the microscope setup and a description are given in **figure 6.1**. The quarter wave plate on a rotation mount made it possible to switch quickly between linear and circular polarisations of light, and so in each experiment all of linear, LCP and RCP input light were measured; the luminescence spectra for the three different polarisations are in **figure 6.2(a).** For these measurements there were no additional layers added to the surface (e.g., water or chiral molecules), as depicted in the inset showing a simple diagram of the three-layer system – air, Eu_2O_3 and polycarbonate substrate. The spectra are zoomed in to show only the insensitive peak (590 nm, $^5D_0 \rightarrow {}^7F_1$ emission) and the hypersensitive peak (615 nm, $^5D_0 \rightarrow {}^7F_2$ emission), as relative changes in these peaks will be used to identify alterations to the luminescence. The spectra for LCP and RCP are identical, and shown to have a decreased hypersensitive peak intensity relative to linear polarisation, by about 5%. As the Eu_2O_3 layer is achiral and the only difference between the spectra is the polarisation of the input light, the justification for this change could be an exchange of angular momentum or optical chirality between the light and the inorganic dielectric, as described by the *IE* term in the continuity equation. A further series experiments and numerical simulations were then devised to test this claim, and to aid in understanding the mechanism of this exchange and the chiral perturbation it causes.

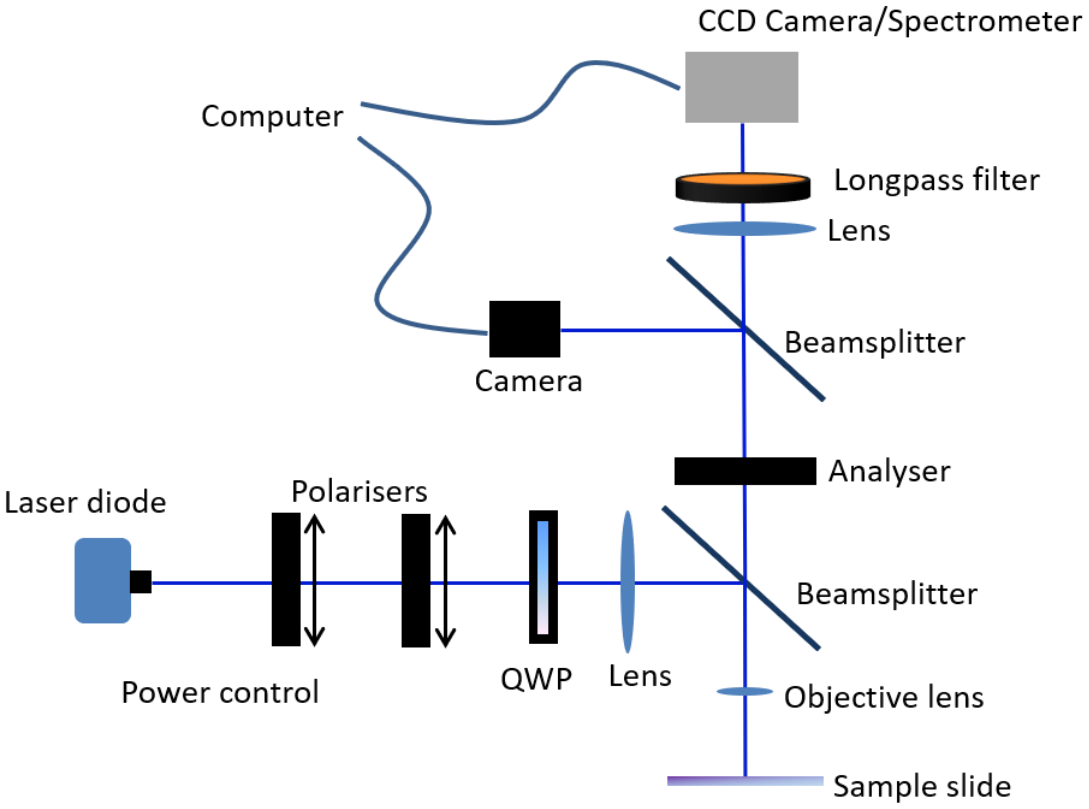

Figure 6.1 Diagram of the microscope setup for luminescence measurements. The quarter-wave plate allows for CPL to be generated, and can be easily switched to linear polarisation by rotating its mount. The two linear polarisers at the input labelled as 'power control' were used to control the input laser power. The first polariser after the laser diode would be rotated to raise and lower power, whilst the second remained fixed to define the input polarisation. An optical camera with a direct view of the sample slide, labelled as 'Camera' was used to ensure that the laser was aligned to the required point on the samples. The analyser was positioned cross-polarised with respect to the input to reduce the amount of laser light entering the camera as much as possible, to help with observing the sample and to reduce background in the emission spectra.

As we equate the decrease of luminescence intensity with exchange of chirality with the dielectric, luminescence intensity was measured with increasing input laser power, thereby increasing the total angular momentum of the beam interacting with the Eu_2O_3. The two polarisers at the input of the microscope situated after the laser diode were operated as a power control as described in chapter 5.

The plots of luminescence intensity against power (which is given as a percentage of the maximum, 18 mW) are shown in **figure 6.3(a)** and **(b)** for CPL and linear polarisation respectively. Red lines on these graphs are linear fits to the data and allow for gradients to be calculated.

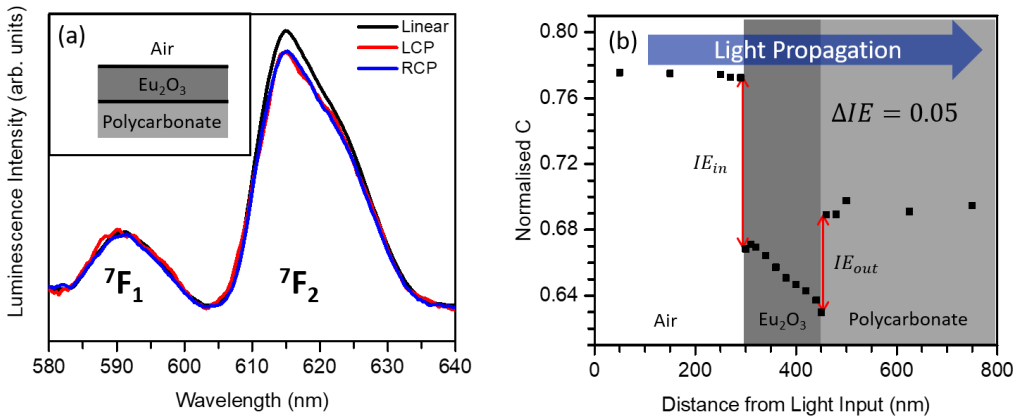

Figure 6.2 Transfer of Optical Chirality from CPL Changes Eu_2O_3 Luminescence. (a) The intensity of the hypersensitive $^7F_2$ luminescence peak is lower when excited by CPL (red for LCP, blue for RCP) compared to linear (black) polarisation. By comparison to **figure 6.4** it is evident this is only the case if the two interfaces in the sample (air-Eu_2O_3 and Eu_2O_3-polycarbonate in this case, shown in (a) and (b)) have different gradients in their dielectric properties. (b) Electromagnetic simulation calculating *C* as it changes with distance from the input port on passing through air, Eu_2O_3 and polycarbonate, using thicknesses of 300 nm, 150 nm and 350 nm respectively in the model for the three films. The magnitudes of the interface-exchange (*IE)* terms for each interface are highlighted by the red arrows, and the net exchange of *C*, *ΔIE* is given.

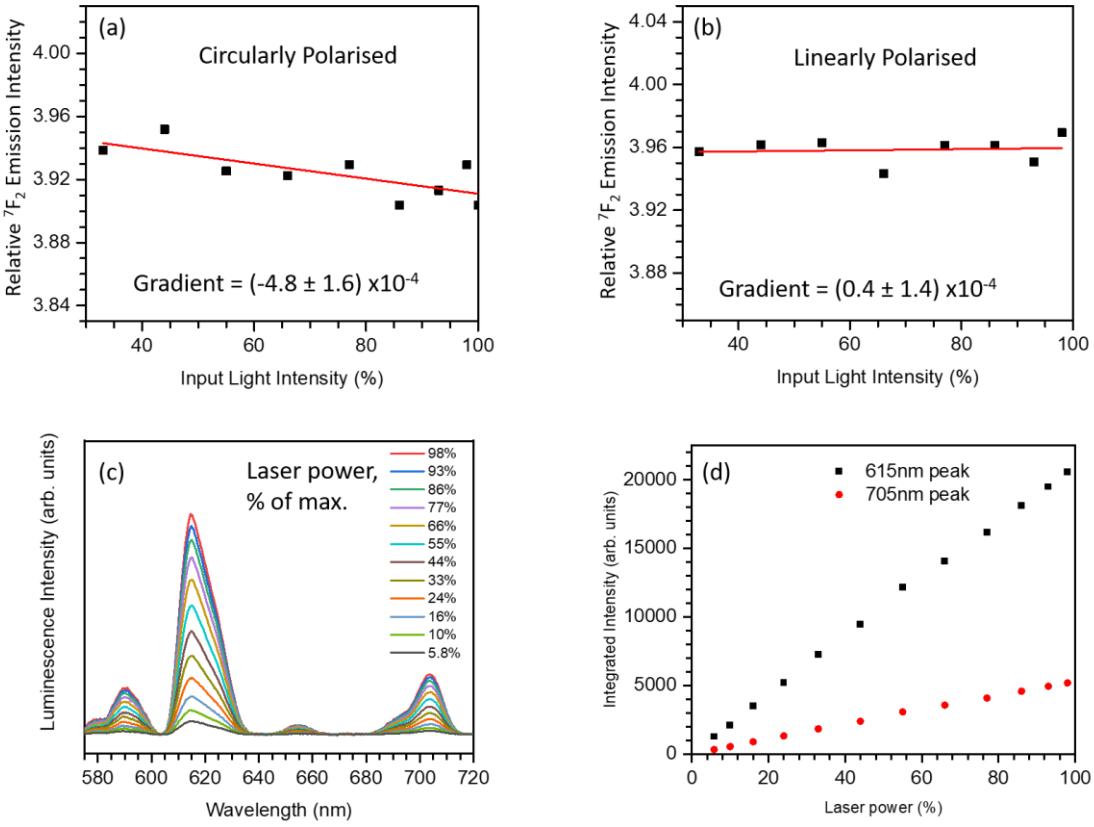

Figure 6.3. Relative Luminescence Peak Intensity Dependence on Laser Power. The luminescence intensity ratio (relative intensity) decreases for (a) CPL with input light power owing to increasing transfer of optical chirality, but remains constant for (b) linear light that has no angular momentum or chirality. The data is fitted to straight lines (red) in (a) and (b) to help visualise the dependence of *C* on laser power. (c) Luminescence spectra for laser power decreasing from maximum to minimum and (d) The individual components of the luminescence ratio for CPL for the $^7F_2$ (615 nm) and $^7F_4$ (705 nm) peaks.

The emission intensity is calculated as a ratio against a peak insensitive to structural changes, and so it was found that at lower laser powers of < 35% the intensity ratio for CPL is slightly lower than for linear, as expected from the result in **figure 6.2(a)**.

As the power is increased from there towards 100% the behaviour diverges – the intensity of emission for samples excited by CPL decreases but does not change for linear within error, as demonstrated by the gradients shown in **figure 6.3**. Based on the deductions from the initial experiment, this linear dependence is consistent with a greater rate of exchange of optical chirality (optical spin angular momentum), creating a larger chiral perturbation with increasing laser power. Optical chirality transfer might well be non-linear for much higher intensity laser light pulses when higher order terms of the electronic permittivity begin to influence the exchange process.

The luminescence ratios for power dependency of the flat surface (and later, for the nanostructures) are calculated by dividing the integrated $^7F_2$ (615 nm) peak by the integrated $^7F_4$ (705 nm) peak, to demonstrate relative changes with power for the meta-film. The 705 nm peak is chosen as it remains significantly less sensitive to its environment than the 615 nm peak, and provided more stable calculations than for the $^7F_1$ owing to less prominent background from the polycarbonate substrate compared to at the 590 nm peak. The luminescence spectra for the power dependency for CPL are shown as an example in **figure 6.3(c)**. The integrated intensity values in **figure 6.3(d)** are shown before being divided for the flat surface, as an example to demonstrate that the signal is not saturating and this is not the source of the effects seen.

Simulating Chirality Exchange at Interfaces

The previous two experiments (**figures 6.2(a)** and **6.3(a, b)**) have demonstrated that illuminating the Eu_2O_3 film with circularly polarised light reduces the emission compared to linear, concluding this as a consequence of optical chirality being exchanged at the interfaces. To confirm that this exchange was indeed happening, electromagnetic, finite element simulations were built using COMSOL (wave optics module) to replicate the experiment numerically, such that the optical chirality density, *C*, could be calculated directly for those with CPL input.

For the unstructured Eu_2O_3 film, a simple 3-layer unit cell was created (700 nm diameter to be consistent with most nanostructure-based models), with a 150 nm

layer of the oxide in the centre, polycarbonate below it to act as the substrate with the region above set as air to emulate the experiment setup. This will henceforth be referred to as the 'three-layer' model. Periodic boundary conditions in the x and y directions were used to approximate a continuous film, and perfectly matched layers were added at the top and bottom to absorb light exiting the cell. Finally input and output ports were added to introduce CPL into the model. Air and polycarbonate are relatively simple to implement in the software since they are premade, whereas for the Eu_2O_3 layer it was necessary to construct its properties manually. Interpolations for the real and imaginary parts of refractive index as a function of wavelength were created by using data from two sources[144,145], and its relative magnetic permeability was set at 1.01 to replicate the paramagnetic behaviour of Eu_2O_3. As per the finite element method, this unit cell was then broken down into discrete mesh elements to define the nodes at which the electromagnetic calculations would be performed.

Following the setup, the simulation was then run to solve for Maxwell's equations in the above system. After completion, individual horizontal planes were inserted into the model at regular spacings between the input and output ports, such that the optical chirality density at those slices could be determined by integration using **equation 6.1**. The same series of calculations is then repeated, but with modified variants of this model that contain only one of the three-layer materials being studied – air, Eu_2O_3 or polycarbonate only. The values of *C* calculated in these variants provide normalisation factors against free moving CPL for *C* in each material in the three-layer model. With the assumption that the chiral perturbation is dependent only on the magnitude of the net chirality transferred and not its sign, and as these normalisations use the same handedness of CPL as the three-layer model, the result is that the *C* parameter quoted will always be positive. Thus, a picture of how the chirality in the system changes as the light propagates through it is created, **figure 6.2 (b).** This figure shows that at the two interfaces, air-Eu_2O_3 and Eu_2O_3-polycarbonate, the value of *C* shifts dramatically. With reference to **equation 6.21**, we designate these changes as the interface-exchange terms IE_{in} and IE_{out} respectively. The overall chirality transferred to a film, ΔIE, from an incident CPL beam is defined as

$$\Delta IE = IE_{inc} - IE_{out} \qquad [6.22]$$

As shown in the figure, ΔIE = 0.05 for the unstructured Eu_2O_3 film with both LCP and RCP excitation. This exchange is consistent with the understanding of the continuity equation – at the interface optical chirality can be exchanged if there is non-zero gradient in the permittivity from one material to the next. At the 'top' interface, there is a change from air (refractive index = 1.00) to Eu_2O_3 (refractive index = 2.05), resulting in a larger *IE* than at the 'bottom' interface where there is a change from Eu_2O_3 to polycarbonate (refractive index = 1.62). Note that in the calculations there is a decrease in *C* within the Eu_2O_3 as a result of absorption in the film – this has been accounted for in the calculations of ΔIE and so does not affect the value quoted.

As a check for the validity of these observations, another experiment and set of simulations were performed, in which microscope oil (refractive index 1.518) is added to the sample surface, effectively replacing the air layer and changing the permittivity gradient at the top interface to be very similar to at the bottom. In **figure 6.4(a)** are luminescence spectra collected in the same manner as for **figure 6.2(a)**, with a layer of microscope oil (see inset), for all of LCP, RCP and linearly polarised light. In this case we find that there is no discernible difference in the intensity of the hypersensitive luminescence peak between the different polarisations – either there is no change at all or most likely it is too small to be separable from the noise. In addition, numerical simulations to replicate this effect were run as per **figure 6.2(b)** with a higher refractive index layer added at the top, **figure 6.4(b)**. In this case by contrast to **figure 6.2**, it is found that $\Delta IE \approx 0$ for both LCP and RCP. As such, in cases where the gradients in permittivity at the interfaces are approximately the same, there is no net optical chirality transfer to the film and no change to the luminescence spectra.

Meta-Crystal Field Model of Optical Chirality-induced Symmetry Breaking in Eu_2O_3

It is proposed that the transfer of optical chirality from CPL to the dielectric by the interfacial mechanism imposes an electronic torque on the Eu_2O_3, resulting in a chiral, symmetry reducing perturbation that decreases the luminescence intensity observed from the Eu^{3+} ions in the film. This torque distorts the electron density around the metal ions in the film so that this chirality transfer physically manifests as a bulk polarisation within the material, which has a sense of direction about the incident beam.

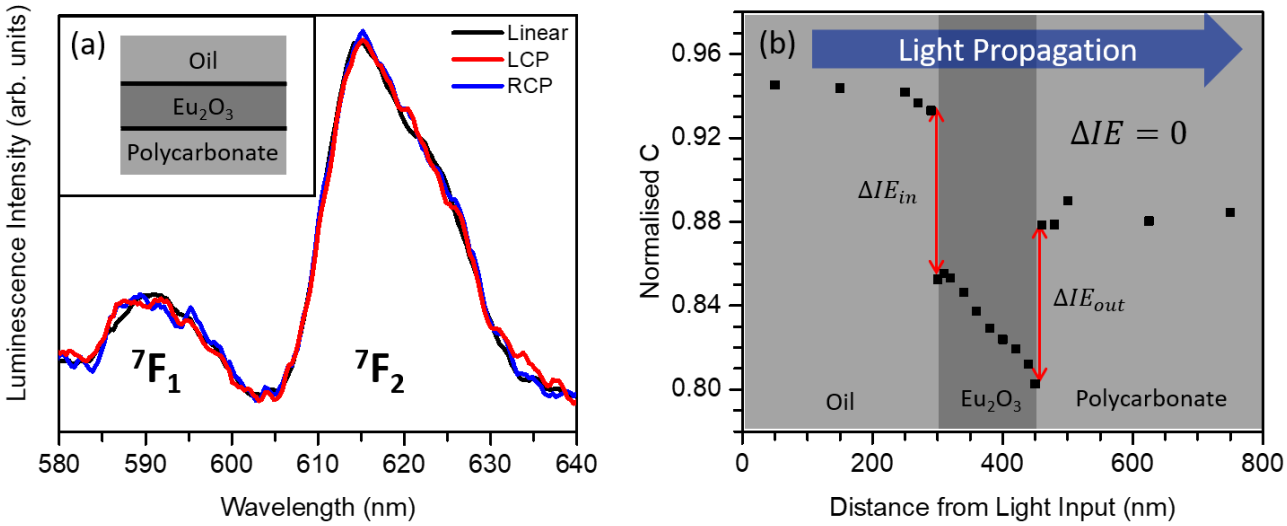

Figure 6.4 No Net *C* Transfer with Equivalent Interfaces Studied using Microscope Oil. (a) Luminescence spectra normalized to the insensitive peak ($^7F_1$) for LCP (red), RCP (blue) and linearly polarised light (black) with a thin layer of microscope oil on the sample surface. (b) The equivalent numerical simulation to that shown in **figure 6.2(b)** for the oil-Eu2O3-polycarbonate three-layer system, using thicknesses of 300 nm (oil), 150 nm (Eu2O3) and 350 nm (polycarbonate) for the three films.

The circulation of the electrons caused by the chirality of the incident light is the cause of the symmetry reduction in the chemical environment of the ion, in a similar manner to bound ligands forming a crystal field, creating an electrostatic potential that acts as a chiral perturbation. The symmetry reduction is also reversible, as the electronic torque causing the perturbation is removed when the laser is switched off. This phenomenon that will be termed a 'meta-crystal field' has been established to occur in the Eu_2O_3 films studied so far in this chapter. Eu^{3+} is known to be extremely sensitive to its co-ordination environment, which has made Eu_2O_3 a good model system to test for the meta-crystal field given its luminescence properties are highly dependent on the local symmetry of the ion. This is not to say that the creation of a meta-crystal field is specific to those inorganics that exhibit luminescence, just that it can be easily detected in Eu_2O_3 owing to its emission and sensitivity to local symmetry.

The proposed mechanism for the formation of the bulk polarisation in Eu_2O_3 is a collective distortion of the array of O^{2-} ions bound to the Eu^{3+} in the film. These larger anions are far more polarisable than the smaller cations, and this distortion reduces the effective symmetry of the co-ordination environment of the metal ion. In **figure**

6.5, the graphics illustrate the physical realisation of this phenomenon. The electronic torque provided by the transferred chirality or spin angular momentum is suggested to be a macroscopic effect occurring over the whole area illuminated by the laser beam, a spot size of about 150 μm diameter. In **figure 6.5(a)** this is demonstrated to cause a polarisation that precesses in a circle, according to the sense of twist of the light, such that locally to a single Eu^{3+} centre the electronic polarisation of all O^{2-} ions would be in the same direction at any given moment. Returning to the crystal field analogy, an electrostatic field - created by surrounding ligands or crystal structure - lifting the degeneracy of electronic states of the metal ion is known to be a result of the crystal field effect. In the meta-crystal field here, the polarised anions perturb the symmetry of the metal cations because of the electronic torque caused by the transfer of chirality when in the presence of a chiral field.

This must now be extended to explain why the luminescence spectra are altered by this meta-crystal field. The luminescence spectra obtained from the Eu_2O_3 films all produce spectra in which the transitions from the $^5D_0$ state to ^7F_J (J = 0 - 4) are observed, where the hypersensitive $^7F_2$ transition (peak at 615nm) is the strongest. Based on work by Mariscal et al, qualitatively the spectra obtained are consistent with these Eu_2O_3 films consisting of a mixture of the Eu^{3+} co-ordination environments found in the monoclinic and cubic polymorphs.[145] However, the images collected with transmission electron microscopy, **figure 6.6**, suggest that the films are in fact amorphous; there is no long-range crystalline order implying that the Eu_2O_3 formula units will be randomly arranged and oriented. It is expected though that the point group symmetries of the local Eu^{3+} ion co-ordination environments in the two polymorphs – C_s in monoclinic and C_2 in cubic – will be maintained at individual ion sites, as suggested by the analysis of the luminescence spectra.[146] The diagram in **figure 6.5(b)** is an example of how the symmetry of a local C_s symmetry site will be reduced by the meta-crystal field so long as the incident light is not orthogonal to the mirror plane in the ion symmetry. The spirals in the diagram indicate the direction of CPL incidence, along a different bond in each case for ease of visualisation, showing that in the first and third situation the symmetry is reduced to C_1 but it is not in the second, where the light is perpendicular to the mirror plane. By conventional wisdom it might be expected that reducing symmetry in the local ion environment would increase the emission as a result of relaxing selection rules.

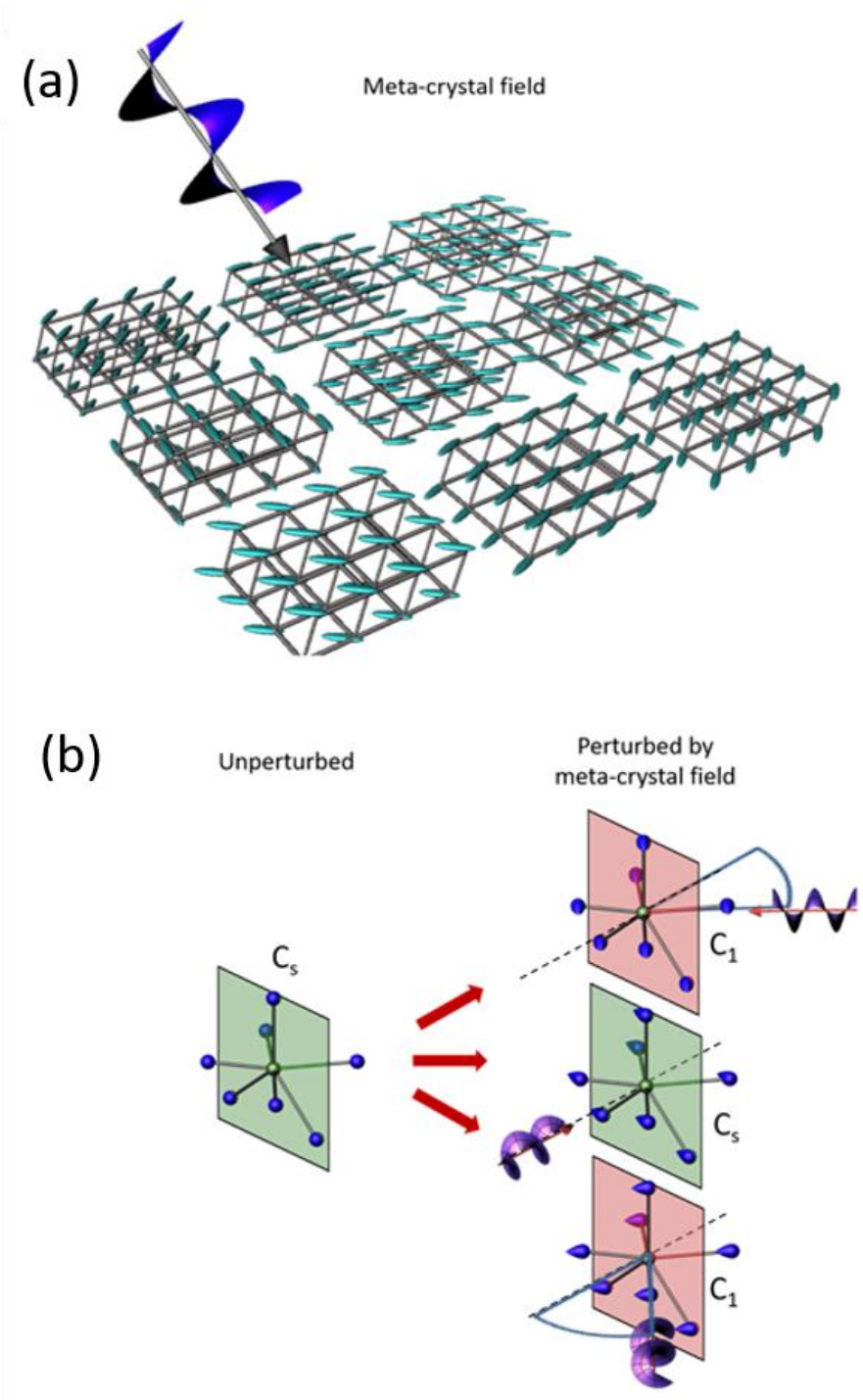

Figure 6.5 Symmetry Reduction in Eu_2O_3 by a Meta-crystal Field. (a) The precession of the bulk polarization (green ellipsoids) induced by an applied electronic torque is represented over an extended length scale in a simple monoclinic film. The lattice is idealised for simplicity but in reality, would be more disordered. The incident CPL is shown by the grey arrow and blue spiral. (b) A Eu^{3+} ion with monoclinic-like C_s symmetry has its symmetry reduced by the meta-crystal field to C_1 (green and blue spheres and ellipsoids are Eu^{3+} and O^{2-} ions respectively). The three cases presented on the right represent the incident CPL being oriented in different directions, where the dotted line is the normal to the mirror plane. The red and green shaded areas are mirror planes that have been lifted or retained respectively after the perturbation by the meta-crystal field. When the light is orthogonal to the mirror plane, the symmetry is not reduced.

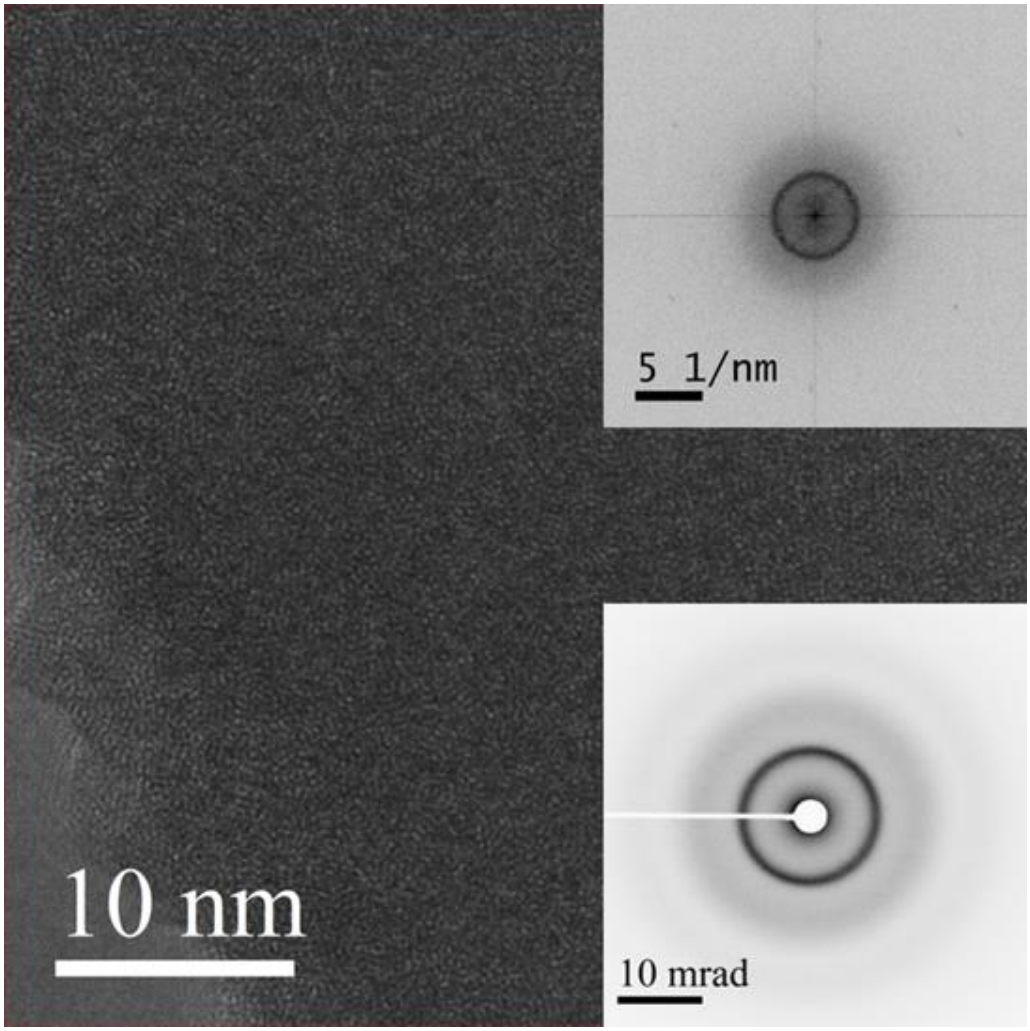

Figure 6.6 Transmission Electron Microscopy Images of the Eu_2O_3 Film. The main image lacks interference fringes that are characteristic of a crystalline material, suggesting an amorphous or glassy film. A Fourier transform (inset, top) and selected electron diffraction pattern (inset, bottom) similarly lack sharp diffractive features. A single, diffuse ring is observed in diffraction that is characteristic of an amorphous, or glassy material.

Contrary to this, it was demonstrated by Tanner that for the 3+ ions of europium (and cerium) the strength of the emission depends on the specific symmetry of the ion rather than a lack of symmetry – indeed, ions with C_s and C_2 symmetries are shown to have relatively high luminescence intensities for the $^7F_2$ band compared to other symmetries.[147] This suggests then that any reduction in this symmetry caused by the meta-crystal field, such as the change from C_s to C_1 for the monoclinic-like ion centres, will result in a relative decrease in the intensity of the hypersensitive transition. This model of symmetry reduction by the meta-crystal field then explains the results of decreasing luminescence obtained in **figures 6.2(a)** and **6.3(a)**, justified by the exchange of chirality at interfaces (**equation 6.21**) inducing an electronic torque. Furthermore, the understanding that either in the case of not

chirality being present in the light, or that of equal permittivity gradients at the nanofilm interfaces there is no net chirality exchanged explains the absence of any decrease in luminescence in **figures 6.2(d)** and **6.3(a)**.

Other explanations for the observed effect in the Eu_2O_3 have been considered, for example, the possibility of the changes in luminescence arising from a mechanical strain placed on the material as opposed to a bulk electron polarisation. Indeed, light bearing angular momentum transfer has previously been demonstrated to be capable of deforming metals.[148,149] However, the laser powers used were too low to provide enough pressure to meaningfully deform the material, given the tens to hundreds of GPa necessary to see such a change in this material and metal oxides in general.[150,151]

Heating of the sample from the laser was another possible origin of the effect, which could lead to changes in its structure leading to the observed decreases in luminescence. In this case though, the experiments were designed to eliminate this as a possibility. It is true that heating would cause changes in the spectra, but prior to measurements being taken the laser was left on illuminating the sample and the changes monitored over time. Only once it was evident that this effect over time was no longer changing the measured luminescence, and once the laser itself was stable according to the temperature control, were the measurements taken. Given the effect was still observed even when there were no fluctuations from heat, we know heating was not the cause.

Luminescence and Simulations of Nanostructured Eu_2O_3 Meta-films

For a final set of experiments, chiral electrostatic fields will be introduced using chiral nanostructures allowing for the exchange of optical chirality density to the Eu_2O_3 film to be modulated in a different manner. By scattering CPL and linearly polarised light from gammadion-shaped chiral nanostructures (see SEM in chapter 3), nearfields can be generated that exhibit spatial variations in both field intensity and *C*. It has previously been discussed in this work that it is possible for the values of *C* to be locally be either higher or lower than that of incident CPL alone, a phenomenon known as superchirality. These periodic arrays of nanostructures take the same hybrid form as has been used earlier in this thesis. 80 nm deep Indentations formed in an injection moulded polycarbonate film are coated in a 150 nm thick film of Eu_2O_3 using pulsed laser deposition, resulting in a 150 nm thick solid gammadion structure with an identically shaped 80 nm deep inverse ‘hole’ structure

directly above it in the nanofilm. The film itself has the same composition as the unstructured film, being amorphous and intrinsically achiral, and as such will have the same gradients in permittivity as the experimental system studied in **figure 6.2**. However, as the optical chirality density and the electromagnetic field intensities can vary spatially over these structures, the exchange of chirality described in **equation 6.21** can also be different to that for the unstructured film, as a result of variations in the $(\mathcal{E} \times \mathcal{E}^*)$ part. Another key difference for the structured films compared to unstructured films is that chiral nearfields are still generated when excited by linearly polarised light and as such chirality can still be transferred to the film to a lesser extent than it would be for CPL.

Initially, a structure whose luminescence spectra exhibited strong emission in the hypersensitive peak was chosen to be studied; spectra were collected for excitation with linear, LCP and RCP light and shown in **figure 6.7** for both the **(a)** LH and **(b)** RH nanostructures. Labels including the diameter and interstitial spacing of the gammadions keep track of the identities of each different nanostructure array, in this case it was 200x300 (200 nm diameter, 300 nm spacing).

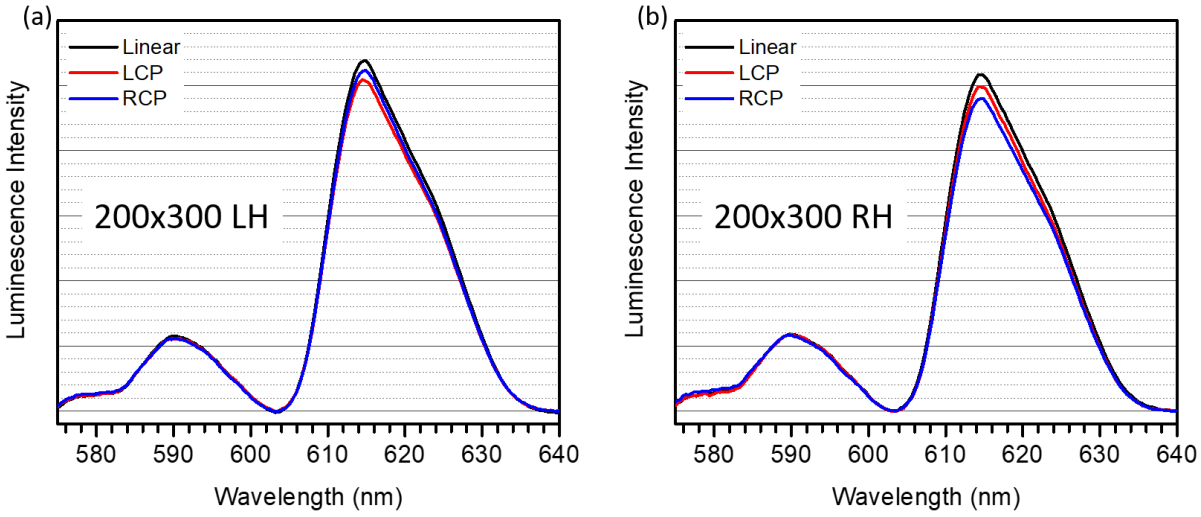

Figure 6.7. Dependence on Light Polarisation for Luminescence of a Nanostructured Eu_2O_3 Film. Luminescence intensities of the insensitive (590 nm) and hypersensitive (615 nm) peaks of Eu^{3+} as excited by Linear (black), LCP (red) and RCP (blue) light. Spectra are shown for the (a) LH gammadion nanostructures and (b) RH structures, showing an equal and opposite intensity dependence on the handedness of the incident CPL. Intensity for linear light is higher than CPL as anticipated from previous results

The effect observed in **figure 6.2(a)** occurs in this case as well, where the intensity of the $^7F_2$ transition peak is decreased for circularly polarised light in comparison to linear. However, now the degeneracy of the CPL emissions has been lifted as for the LH nanostructure the LCP hypersensitive peak decreases to a greater than extent than the RCP, and vice-versa for the RH. Based on the model of chirality exchange, this suggests that the level of chirality exchanged between CPL and a nanostructure interface is also dependent on the chirality of the nearfield in relation to the light, such that the strength of the meta-crystal field applied to these nanostructured films is further modulated resulting in an asymmetry in the luminescence emission intensity. It was discovered though that there may be an issue with using this exact nanostructure identity – the Purcell Effect.

The Purcell Effect is a phenomenon by which an emitter situated in a cavity resonating at its emission frequency experiences an increased rate of spontaneous emission.[152] This could obviously cause problems in interpreting the luminescence data if the nanostructure arrays exhibits a resonance close to the ^7F_J transition peaks. Looking at the reflectivity spectrum (collected using a broadband light source) in **figure 6.8(a)** it is confirmed that a small resonance-like feature exists for the 200x300 array, meaning that the results in **figure 6.7** may be unreliable.

To combat this and remove the influence of these final state effects, other sample arrays were measured, looking for those that showed reasonably high emission without any possible resonances. **Figure 6.8(b)** shows similarly collected reflectivity spectra for three select arrays – 200x500, 400x300 and 500x500 for which there are no resonant peaks and so would not be expected to be influenced by the Purcell Effect. Additionally, the LH and RH forms of these nanostructures have been characterised using ORD spectra, demonstrating no significant optical rotation. Thus, any possible final state effects caused by an optically active sample are not possible for these chosen arrays. With a suitable set of structures chosen a series of luminescence spectra were collected for LCP and RCP light to determine if the emission intensities have the same light and structure handedness dependence as those for the 200x300 meta-film.

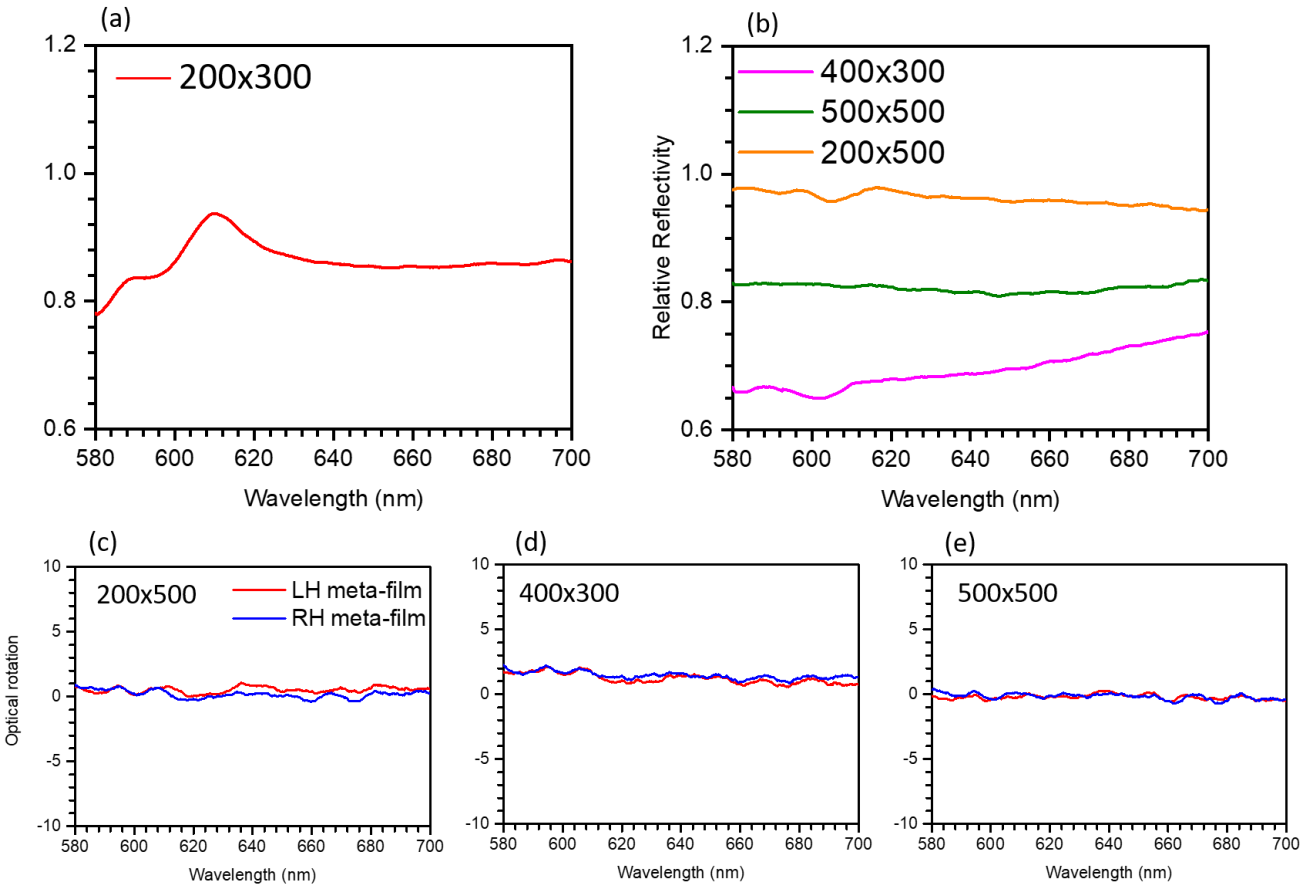

Figure 6.8. Reflectivity and ORD Spectra of various Nanostructured Eu_2O_3 films. (a) Reflectivity of the 200x300 gammadion meta-film has a small resonant feature, but those for (b) 400x300, 500x500 and 200x500 do not comparatively. This combined with the (c-e) LH (red) and RH (blue) structure ORD spectra for the films show little in the way of potential final state effects, making them good choices for the luminescence experiments. The meta-film labels in the legend refer to the nanostructure diameter in nm, followed by their interstitial spacing in nm.

The results are shown in **figure 6.9** for the three new nanostructure variants. In the top right panel for the RH 200x500 meta-film a zoomed-in image is shown to more clearly demonstrate the difference between the $^7F_2$ peak intensities for the LCP and RCP light spectra. A set of luminescence difference spectra, i.e., RCP minus LCP for each structure and handedness, is given in **figure 6.11** as a companion to this though more discussion is required to describe the figure fully. Similar to the result in **figure 6.7**, the 200x500, 400x300 and 500x500 meta-films all exhibit a difference in the relative intensity of the hypersensitive peak between the LCP and RCP spectra as well as a reverse of that difference from the LH to RH structures. However, which of the intensities for LCP and RCP is decreased more by the applied meta-crystal field is not the same for each meta-film – the effect is the opposite for the 400x300 film compared to the other two.

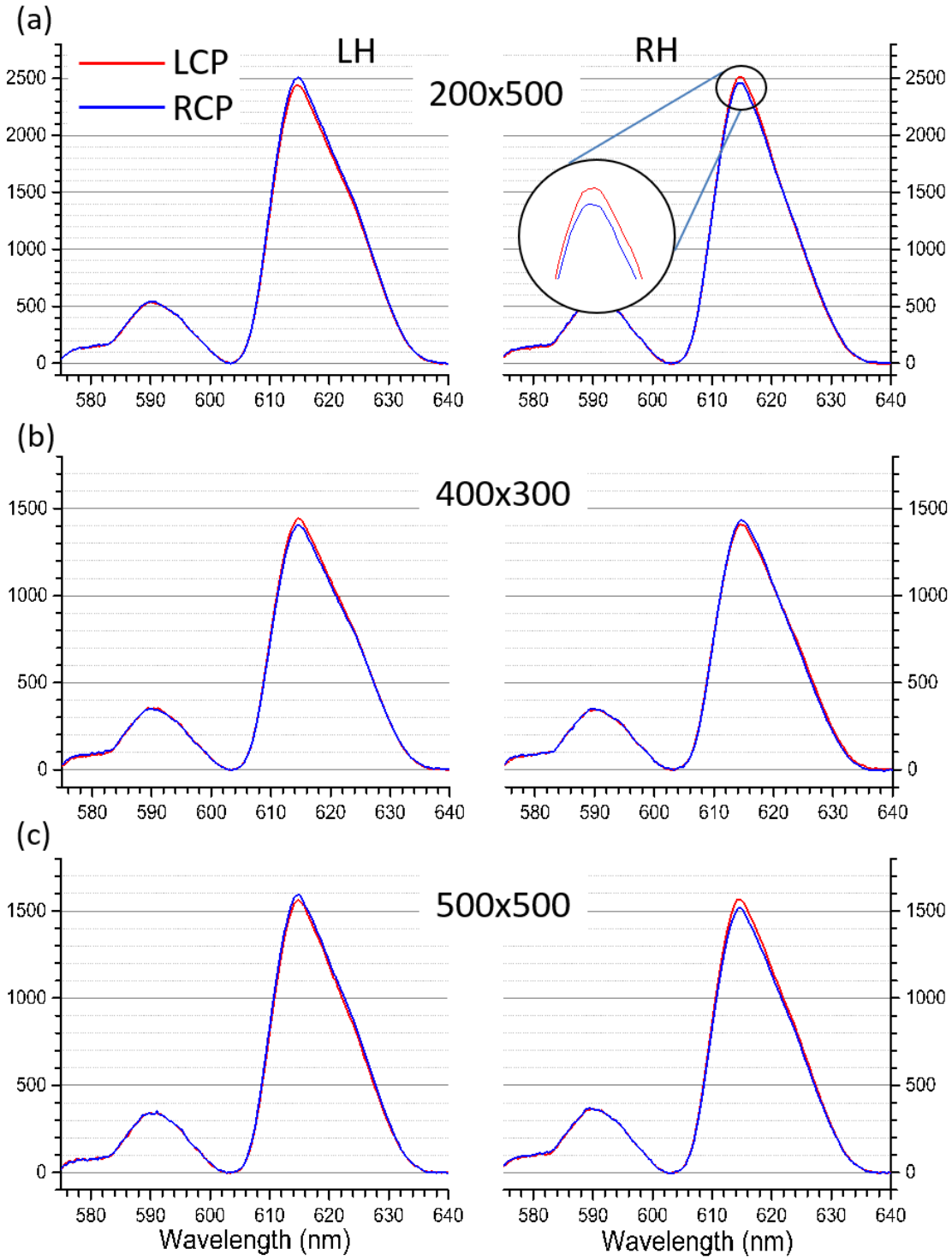

Figure 6.9. Luminescence Spectra of Eu_2O_3 Gammadion Meta-films Under CPL. Luminescence spectra are shown for the (a) 200x500 nanostructured film, (b) 400x300 film and (c) 500x500 film, including the LH left side) and RH (right side) structures. The films were measured being illuminated with LCP (red) and RCP (blue) light. The inset in (a) is a close-up of the change in $^7F_2$ transition peak from LCP to RCP, seen for each meta-film. The observed difference is reversed when moving from LH to RH structures in each case.

Most likely then the difference is not related to the relative handedness of the structure and light, but on the specific geometry of each individual meta-film. In order to validate this experimental observation, numerical simulations can be performed to calculate the Δ*IE* value for the nanostructured films, in the same manner as was done with the unstructured films.

Gammadion nanostructures were constructed using a CAD software and imported into COMSOL, and geometries of each structure used are shown in the insets in **figure 6.10**. The areas of unstructured Eu_2O_3 film surrounding the structures along with the Floquet boundary conditions applied define the interstitial spacing of the periodic gammadion arrays in the x and y directions, mimicking the physical samples. In addition to those structures used for the results in **figure 6.9**, one with the dimensions of 200 nm diameter and 200 nm spacing was created. This structure was previously known to have a strong resonance in the visible region, and so was made to check for consistency between experiment and simulation. In **figure 6.10**, an experimental reflectivity spectrum for the 200x200 meta-film is shown alongside that calculated by simulation showing good qualitative agreement, supporting the models being used for the structures. This figure also shows a visualisation of the optical chirality distribution of this structure with incident LCP and RCP light. Having calculated *C* for the structure as shown, it can also be integrated over each necessary surface, such that ΔIE values can be obtained for structure and polarisation combination. A slightly different approach is necessary here though, compared to the unstructured surface, as measuring *C* directly at the interfaces given the topology of the nanostructure would prove unreliable.

In this instance the values of *C* are calculated near the input port to represent the incident light, *C*(incidence), and at the output port for the transmission *C*(transmission). The reason is that the difference between the chirality entering and leaving the system is equal to the combination of that lost in the intervening material due to absorption, and transferred to the film by the interface-exchange mechanism, i.e., *C*(absorbed+exchanged) = *C*(incidence) – *C*(transmission). As Eu_2O_3 itself is achiral the absorption is expected to be identical for LCP and RCP, so that when the difference between them is calculated this term is removed, resulting in only the difference in the exchange ($\Delta IE_{RCP} - \Delta IE_{LCP}$) being produced.

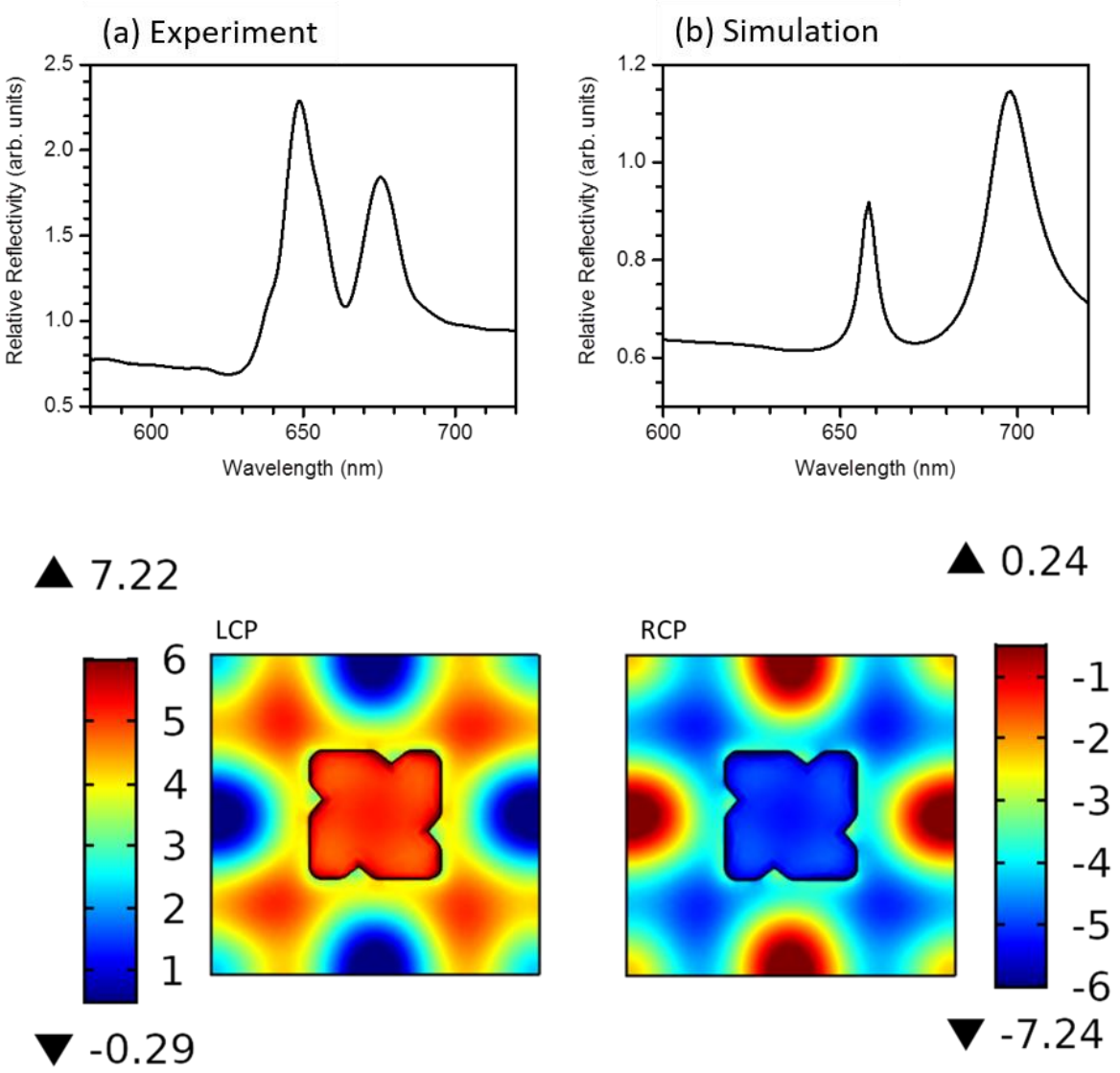

Figure 6.10. Comparison of Experimental and Simulated Reflectivity for a Eu_2O_3 Meta-film and Associated chirality maps. (a) Experimental reflectivity and (b) that obtained from numerical simulation show good qualitative agreement for the 200x200 meta-film, used as an example of a structure exhibiting a strong resonance. The spatial distribution of optical chirality is shown in the lower images for LCP (left) and RCP (right) incident light on this structure.

The values of *C* for incidence, transmission and their difference for each structure and circular polarisation and the equivalent for the unstructured surface are provided in **table 6-1**. The values in the table are normalised against those found for CPL in air (incidence) and polycarbonate (transmission) such that *C* at the input with no material interfaces would be 1. However, on reflection from the air-Eu_2O_3 interface the calculation being performed interprets this as a reversal of the sign of *C* (reproducing the expected reversal of CPL handedness on reflection). The interference of the incident and reflected light combining their respective optical chiralities is what results in the *C*(incidence) values in **table 6-1** being less than 1.

TABLE 6-1. NORMALISED INEGRATED OPTICAL CHIRALITY DENSITY CALCULATED IN COMSOL MODELS. A VARIETY OF EU_2O_3 METAFILMS AS WELL AS THE UNSTRUCTURED FILM HAVE C CALCULATED AT THE INPUT (INCIDENCE) AND OUTPUT (TRANSMISSION), WHERE THE C(ABSORBED+EXCHANGED) IS THE DIFFERENCE BETWEEN THEM.

Film type and Polarisation	*C*(incidence)	*C*(transmission)	*C* (absorbed +exchanged)
Surface LCP	0.7726	0.6912	0.0814
Surface RCP	0.7726	0.6912	0.0814
200x500 LCP	0.8235	0.7018	0.1217
200x500 RCP	0.8235	0.7062	0.1173
400x300 LCP	0.8267	0.7353	0.0914
400x300 RCP	0.8296	0.7296	0.1000
500x500 LCP	0.8245	0.726	0.0984
500x500 RCP	0.8315	0.7552	0.0763

The differential exchange values ($\Delta IE_{RCP} - \Delta IE_{LCP}$) are calculated from **table 6-1** as described and are shown in **figure 6.11** for the LH nanostructures in red and the RH in blue. The figure also includes a difference spectrum obtained from the unstructured surface (black lines), for comparison with a case with no asymmetry between LCP and RCP. With the spectra in **figure 6.11**, the differences described in figure 6.8 can be more clearly visualised. The signs of the differential exchange terms given in the figure correlate with the direction of the $^7F_2$ transition peaks in the difference spectra. Specifically, positive values for the exchange asymmetry correspond to a negative sense in the difference spectrum, and vice-versa. This is consistent with the meta-crystal field model established that a greater level of optical chirality exchange is concurrent with a lowering of the luminescence intensity.

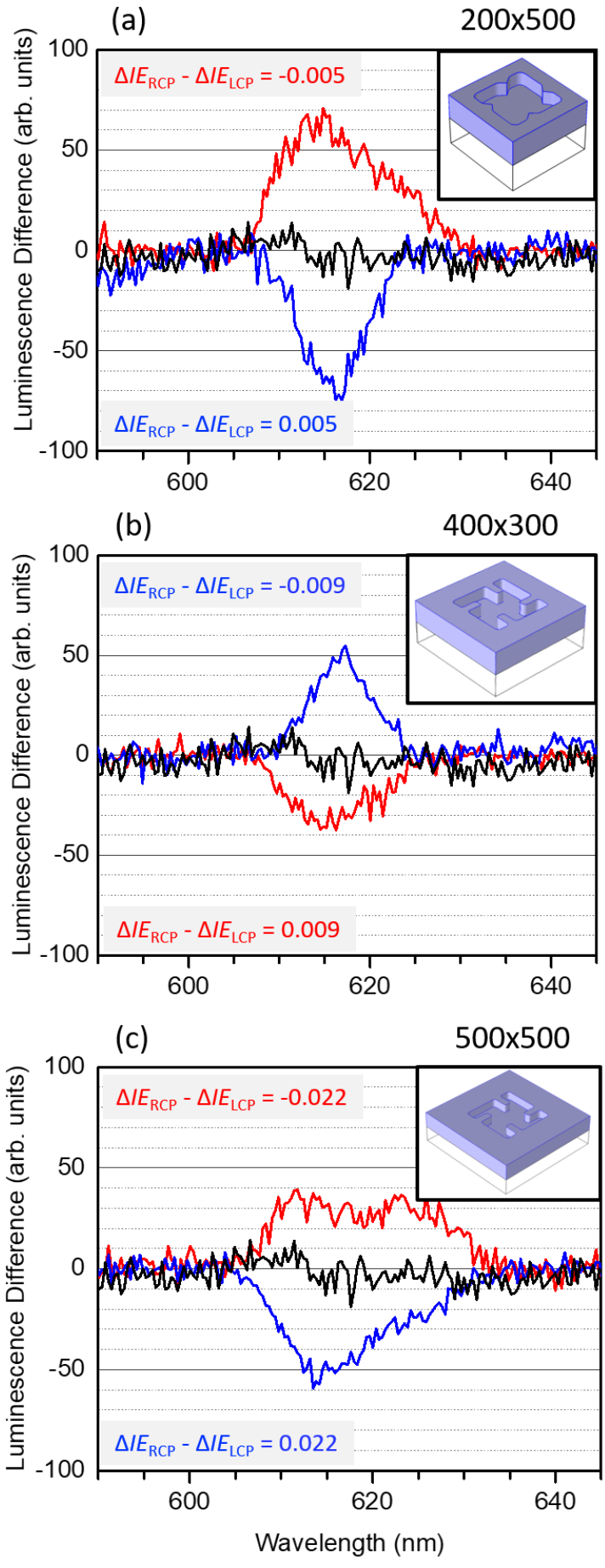

Figure 6.11. Luminescence difference spectra for metafilms. (A)-(C) show the difference in luminescence RCP - LCP for the LH nanostructure (red), RH nanostructure (blue) and equivalent unstructured surface (black). The LH and RH structures show opposite differences at the $^7F_2$ peak. The width and spacing labels equate to the lateral size and interstitial spacing of the nanostructures respectively. ΔIE_{RCP} - ΔIE_{LCP} values for each handedness of structure is shown (Red and Blue for LH and RH structures respectively), demonstrating the same equal and opposite behaviour as the difference spectra. Insets show structure geometries not drawn to scale (See supplementary information for scale diagrams).

Finally, to understand the connection between the magnitude of the exchange and that of the luminescence difference an asymmetry parameter *g*, **equation 6.23**, is calculated and compared with ($\Delta IE_{RCP} - \Delta IE_{LCP}$) in **table 6-2**

$$g = \frac{2(I^{RH} - I^{LH})}{(I^{RH} + I^{LH})}, \qquad [6.23]$$

where I^{lH} and I^{RH} are the intensities of the $^7F_2$ emission band for the LH and RH nanostructure difference spectra respectively. The meta-films that had the highest differential optical chirality exchange, 500x500, are also found to have the highest asymmetry factor in the spectra. Beyond this there appears to be no connection in the magnitude of the two factors – there is no simple correlation between the nanostructure geometry and the amount of chirality transferred to it.

The explanation is that the simulations deal with idealised structures that do not account for defects in the structures and inconsistencies from the design to the fabricated sample. These aspects of the samples may lead to changes in the level of chirality exchange that are not predicted by the electromagnetic modelling. This also accounts for difference spectra not being exact mirror images of each other, as LH and RH structures on the samples may have slight variations from one to the other as a result of the fabrication process.

TABLE 6-2. ASYMMETRY PARAMETERS AND OPTICAL CHIRALITY EXCHANGE FOR META-FILMS.

Meta-film type and handedness	*g*	$\Delta IE_{RCP} - \Delta IE_{LCP}$
200x500 LH	0.023±0.003	-0.005
200x500 RH	-0.015±0.003	0.005
400x300 LH	-0.019±0.003	0.009
400x300 RH	0.018±0.003	-0.009
500x500 LH	0.028±0.003	-0.022
500x500 RH	-0. 032±0.003	0.022

CONCLUSIONS AND FINAL REMARKS

In this thesis the effects of chiral fields and molecules on the properties of metal and inorganic metamaterials have been investigated. In the first section it was discovered that the coupling between electromagnetic modes in the PIR resonance of chiral gold metamaterials could be manipulated through use of chiral incident light (in the form of CPL) and layers of chiral molecules at the surface. By application of numerical simulations, this effect was understood to be the result of asymmetries in the optical chirality density of the electromagnetic nearfields. This is caused by interactions of light, nanostructures and molecules of the same handedness, increasing *C* relative to the achiral case, or the opposite handedness decreasing *C*. This was further progressed to the replication of asymmetries in dielectric layers with specific orientations (proteins) by the addition of anisotropic properties to the dielectric in the simulation.

In the second section, changes in chemical symmetry of europium (III) oxide films and metamaterials were probed using luminescence spectroscopy. A luminescence microscope was first custom built and tested to optimise luminescence signal and stability. Then, optical chirality density in the fields, either from incident CPL or chiral nearfields of nanostructures, was found to change the relative luminescence intensities of a hypersensitive transition in the Eu_2O_3. A model describing the mechanism of these changes was proposed, working from the continuity equation for the conservation of optical chirality density. It suggested that optical chirality could be exchanged between materials at their interfaces, resulting in a bulk chiral polarisation of ions in the film that would change the electronic symmetry around the Eu^{3+} ion, changing its emission intensities. Electromagnetic simulations validated this hypothesis by demonstrating an exchange of chirality into the film in a three-layer system (air, Eu_2O_3, polycarbonate). Further, it was demonstrated that this transfer only occurs if the gradient in dielectric constant at the top and bottom interfaces were different, creating a differential chirality transfer between the two interfaces. Lastly, the asymmetry in the luminescence changes for chiral nanostructures exposed to LCP and RCP were found to be opposite for right- and left-handed structures, further validating the interface-exchange model.

A potential continuation of the work presented in Chapter 6 would be to investigate the effect of light carrying orbital angular momentum (OAM) on the Eu_2O_3 films. Laguerre-Gauss modes of light have spatially varying phasefronts and propagate as light twisting around a central void, with $m\hbar$ angular momentum per photon. The value *m* is the topological charge of the beam i.e., the number of twists in the beam in one oscillation period. In theory, OAM obeys a similar conservation law as that discussed for optical chirality density and so interface OAM transfer processes could also be expected to affect the Eu_2O_3 film. Some preliminary luminescence experiments have been conducted using OAM beams generated by a spiral phaseplate optical component, but those results are not yet fully understood. The decision was made not to include that work here as further experiments and accompanying numerical simulations would be needed to complete it, and time did not allow for it.

REFERENCES

(1) Martín, F. Metamaterials for Wireless Communications, Radiofrequency Identification, and Sensors. *ISRN Electron.* **2012**, *2012*, 1–29.

(2) Alù, A.; Engheta, N. Plasmonic and Metamaterial Cloaking: Physical Mechanisms and Potentials. *J. Opt. A Pure Appl. Opt.* **2008**, *10*, 093002.

(3) Anker, J. N.; Hall, W. P.; Lyandres, O.; Shah, N. C.; Zhao, J.; Van Duyne, R. P. Biosensing with Plasmonic Nanosensors. *Nat. Mater.* **2008**, *7*, 442–453.

(4) Atwater, H. A.; Polman, A. Plasmonics for Improved Photovoltaic Devices. *Nat. Mater.* **2010**, *9*, 205–213.

(5) Zhang, J.; Gecevičius, M.; Beresna, M.; Kazansky, P. G. Seemingly Unlimited Lifetime Data Storage in Nanostructured Glass. *Phys. Rev. Lett.* **2014**, *112*, 033901.

(6) Tassin, P.; Zhang, L.; Koschny, T.; Economou, E. N.; Soukoulis, C. M. Electromagnetically Induced Transparency in Metamaterials. In *Conference on Lasers and Electro-Optics/International Quantum Electronics Conference*; OSA: Washington, D.C., 2009; Vol. 17, p ITuD7.

(7) Vafapour, Z.; Alaei, H. Achieving a High Q-Factor and Tunable Slow-Light via Classical Electromagnetically Induced Transparency (Cl-EIT) in Metamaterials. *Plasmonics* **2017**, *12*, 479–488.

(8) Lee, Y. Y.; Kim, R. M.; Im, S. W.; Balamurugan, M.; Nam, K. T. Plasmonic Metamaterials for Chiral Sensing Applications. *Nanoscale* **2020**, *12*, 58–66.

(9) Yoo, S.; Park, Q.-H. Metamaterials and Chiral Sensing: A Review of Fundamentals and Applications. *Nanophotonics* **2019**, *8*, 249–261.

(10) Kittel, C. *Introduction to Solid State Physics, 8th Edition*; 2004.

(11) Lu, X.; Rycenga, M.; Skrabalak, S. E.; Wiley, B.; Xia, Y. Chemical Synthesis of Novel Plasmonic Nanoparticles. *Annu. Rev. Phys. Chem.* **2009**, *60*, 167–192.

(12) Zhong, Y.; Malagari, S. D.; Hamilton, T.; Wasserman, D. Review of Mid-Infrared Plasmonic Materials. *J. Nanophotonics* **2015**, *9*, 093791.

(13) Khurgin, J. B.; Boltasseva, A. Reflecting upon the Losses in Plasmonics and Metamaterials. *MRS Bull.* **2012**, *37*, 768–779.

(14) Zhang, J.; Zhang, L.; Xu, W. Surface Plasmon Polaritons: Physics and Applications. *J. Phys. D. Appl. Phys.* **2012**, *45*, 113001.

(15) Petryayeva, E.; Krull, U. J. Localized Surface Plasmon Resonance: Nanostructures, Bioassays and Biosensing—A Review. *Anal. Chim. Acta* **2011**, *706*, 8–24.

(16) Rodrigo, D.; Tittl, A.; Ait-Bouziad, N.; John-Herpin, A.; Limaj, O.; Kelly, C.; Yoo, D.; Wittenberg, N. J.; Oh, S.-H.; Lashuel, H. A.; Altug, H. Resolving Molecule-Specific Information in Dynamic Lipid Membrane Processes with Multi-Resonant Infrared Metasurfaces. *Nat. Commun.* **2018**, *9*, 2160.

(17) Pattnaik, P. Surface Plasmon Resonance: Applications in Understanding Receptor–Ligand Interaction. *Appl. Biochem. Biotechnol.* **2005**, *126*, 079–092.

(18) Haynes, C. L.; McFarland, A. D.; Van Duyne, R. P. Surface-Enhanced Raman Spectroscopy. *Anal. Chem.* **2005**, *77*, 338 A-346 A.

(19) Ataka, K.; Heberle, J. Biochemical Applications of Surface-Enhanced Infrared Absorption Spectroscopy. *Anal. Bioanal. Chem.* **2007**, *388*, 47–54.

(20) Tang, Y.; Zeng, X.; Liang, J. Surface Plasmon Resonance: An Introduction to a Surface Spectroscopy Technique. *J. Chem. Educ.* **2010**, *87*, 742–746.

(21) Willets, K. A.; Van Duyne, R. P. Localized Surface Plasmon Resonance Spectroscopy and Sensing. *Annu. Rev. Phys. Chem.* **2007**.

(22) Barron, L. D. *Molecular Light Scattering and Optical Activity*; Cambridge University Press, 2004.

(23) Barron, L. D. Symmetry and Molecular Chirality. *Chem. Soc. Rev.* **1986**, *15*, 189.

(24) Cahn, R. S.; Ingold, C. K.; Prelog, V. The Specification of Asymmetric Configuration in Organic Chemistry. *Experientia* **1956**, *12*, 81–94.

(25) (JCBN), I.-I. J. C. on B. N. Nomenclature and Symbolism for Amino Acids and Peptides. Recommendations 1983. *Eur. J. Biochem.* **1984**, *138*, 9–37.

(26) Bada, J. L. Origins of Homochirality. *Nature* **1995**, *374*, 594–595.

(27) Malyshko, E. V.; Tverdislov, V. A. Chirality as a Physical Aspect of Structure Formation in Biological Macromolecular Systems. *J. Phys. Conf. Ser.* **2016**, *741*, 012065.

(28) Efimov, A. V. Chirality and Handedness of Protein Structures. *Biochem.* **2018**, *83*, S103–S110.

(29) Kean, W. F.; Howard-Lock, H. E.; Lock, C. J. L. Chirality in Antirheumatic Drugs. *Lancet* **1991**, *338*, 1565–1568.

(30) He, M.; Zhao, S.; Chen, J. Chiral Separation of Penicillamine Enantiomers by Capillary Electrophoresis and Its Application. *Chinese J. Anal. Chem.* **2006**, *34*, 655–658.

(31) Kim, J. H.; Scialli, A. R. Thalidomide: The Tragedy of Birth Defects and the Effective Treatment of Disease. *Toxicol. Sci.* **2011**, *122*, 1–6.

(32) Tokunaga, E.; Yamamoto, T.; Ito, E.; Shibata, N. Understanding the Thalidomide Chirality in Biological Processes by the Self-Disproportionation of Enantiomers. *Sci. Rep.* **2018**, *8*, 17131.

(33) Nguyen, L. A.; He, H.; Pham-Huy, C. Chiral Drugs: An Overview. *Int. J. Biomed. Sci.* **2006**, *2*, 85–100.

(34) Schellman, J. A. Circular Dichroism and Optical Rotation. *Chem. Rev.* **1975**, *75*, 323–331.

(35) Giraud-Cotton, S.; Kaftandjian, V. P.; Klein, L. Magnetic Optical Activity in Intense Laser Fields. II. Forward Scattering. *Phys. Rev. A* **1985**, *32*, 2223–2229.

(36) Qiu, Z. Q.; Bader, S. D. Surface Magneto-Optic Kerr Effect (SMOKE). *J. Magn. Magn. Mater.* **1999**, *200*, 664–678.

(37) Buckingham, A. D.; Stephens, P. J. Magnetic Optical Activity. *Annu. Rev. Phys. Chem.* **1966**, *17*, 399–432.

(38) Wagnière, G. H. The Magnetochiral Effect and Related Optical Phenomena. *Chem. Phys.* **1999**, *245*, 165–173.

(39) Rikken, G. L. J. A.; Raupach, E. Observation of Magneto-Chiral Dichroism. *Nature* **1997**, *390*, 493–494.

(40) Sessoli, R.; Boulon, M.-E.; Caneschi, A.; Mannini, M.; Poggini, L.; Wilhelm, F.; Rogalev, A. Strong Magneto-Chiral Dichroism in a Paramagnetic Molecular Helix Observed by Hard X-Rays. *Nat. Phys.* **2015**, *11*, 69–74.

(41) Monteiro, M.; Stari, C.; Cabeza, C.; Martí, A. C. The Polarization of Light and Malus' Law Using Smartphones. *Phys. Teach.* **2017**, *55*, 264–266.

(42) Mason, S. F. Optical Activity and Molecular Dissymmetry. *Contemp. Phys.* **1968**, *9*, 239–256.

(43) Polavarapu, P. L.; Petrovic, A.; Wang, F. Intrinsic Rotation and Molecular Structure. *Chirality* **2003**, *15*, S143–S149.

(44) Chen, Y.-H.; Yang, J. T.; Martinez, H. M. Determination of the Secondary Structures of Proteins by Circular Dichroism and Optical Rotatory Dispersion. *Biochemistry* **1972**, *11*, 4120–4131.

(45) Bohren, C. F. What Did Kramers and Kronig Do and How Did They Do It? *Eur. J. Phys.* **2010**, *31*, 573–577.

(46) Polavarapu, P. L. Kramers−Kronig Transformation for Optical Rotatory Dispersion Studies. *J. Phys. Chem. A* **2005**, *109*, 7013–7023.

(47) Byers, N. E. Noether's Discovery of the Deep Connection Between Symmetries and Conservation Laws. *Isr. Math. Conf. Proc* **1998**, *12*, 67–82.

(48) Hanc, J.; Tuleja, S.; Hancova, M. Symmetries and Conservation Laws: Consequences of Noether's Theorem. *Am. J. Phys.* **2004**, *72*, 428–435.

(49) Philbin, T. G. Lipkin's Conservation Law, Noether's Theorem, and the Relation to Optical Helicity. *Phys. Rev. A - At. Mol. Opt. Phys.* **2013**, *87*.

(50) Campos, I.; Jimenez, J. L. About Poynting's Theorem. *Eur. J. Phys.* **1992**, *13*, 117–121.

(51) Lipkin, D. M. Existence of a New Conservation Law in Electromagnetic Theory. *J. Math. Phys.* **1964**, *5*, 696–700.

(52) PRZANOWSKI, M.; RAJCA, B.; TOSIEK, J. On Some Conservation Laws in the Maxwell Electrodynamics in Vacuum. *Acta Phys. Pol. B* **1994**, *25*, 1065–1077.

(53) Kibble, T. W. B. Conservation Laws for Free Fields. *J. Math. Phys.* **1965**, *6*, 1022–1026.

(54) Tang, Y.; Cohen, A. E. Optical Chirality and Its Interaction with Matter. *Phys. Rev. Lett.* **2010**, *104*, 163901.

(55) Poulikakos, L. V.; Dionne, J. A.; García-Etxarri, A. Optical Helicity and Optical Chirality in Free Space and in the Presence of Matter. *Symmetry (Basel).* **2019**, *11*, 1113.

(56) Tang, Y.; Cohen, A. E. Enhanced Enantioselectivity in Excitation of Chiral Molecules by Superchiral Light. *Science (80-.).* **2011**, *332*, 333–336.

(57) Allen, L.; Beijersbergen, M. W.; Spreeuw, R. J. C.; Woerdman, J. P. Orbital Angular Momentum of Light and the Transformation of Laguerre-Gaussian Laser Modes. In *Optical Angular Momentum*; IOP Publishing Ltd, 2016; Vol. 45, pp 31–35.

(58) Cameron, R. P.; Götte, J. B.; Barnett, S. M.; Yao, A. M. Chirality and the Angular Momentum of Light. *Philos. Trans. R. Soc. A Math. Phys. Eng. Sci.* **2017**, *375*, 20150433.

(59) Bliokh, K. Y.; Nori, F. Characterizing Optical Chirality. *Phys. Rev. A* **2011**, *83*, 021803.

(60) Crimin, F.; Mackinnon, N.; Götte, J.; Barnett, S. Optical Helicity and Chirality: Conservation and Sources. *Appl. Sci.* **2019**, *9*, 828.

(61) Schäferling, M.; Dregely, D.; Hentschel, M.; Giessen, H. Tailoring Enhanced Optical Chirality: Design Principles for Chiral Plasmonic Nanostructures. *Phys. Rev. X* **2012**, *2*, 031010.

(62) Schäferling, M.; Yin, X.; Giessen, H. Formation of Chiral Fields in a Symmetric Environment. *Opt. Express* **2012**, *20*, 26326.

(63) Tullius, R.; Karimullah, A. S.; Rodier, M.; Fitzpatrick, B.; Gadegaard, N.; Barron, L. D.; Rotello,

V. M.; Cooke, G.; Lapthorn, A.; Kadodwala, M. “superchiral” Spectroscopy: Detection of Protein Higher Order Hierarchical Structure with Chiral Plasmonic Nanostructures. *J. Am. Chem. Soc.* **2015**, *137*, 8380–8383.

(64) Jack, C.; Karimullah, A. S.; Tullius, R.; Khorashad, L. K.; Rodier, M.; Fitzpatrick, B.; Barron, L. D.; Gadegaard, N.; Lapthorn, A. J.; Rotello, V. M.; Cooke, G.; Govorov, A. O.; Kadodwala, M. Spatial Control of Chemical Processes on Nanostructures through Nano-Localized Water Heating. *Nat. Commun.* **2016**, *7*, 10946.

(65) Valev, V. K.; Baumberg, J. J.; Sibilia, C.; Verbiest, T. Chirality and Chiroptical Effects in Plasmonic Nanostructures: Fundamentals, Recent Progress, and Outlook. *Adv. Mater.* **2013**, *25*, 2517–2534.

(66) Hendry, E.; Carpy, T.; Johnston, J.; Popland, M.; Mikhaylovskiy, R. V.; Lapthorn, A. J.; Kelly, S. M.; Barron, L. D.; Gadegaard, N.; Kadodwala, M. Ultrasensitive Detection and Characterization of Biomolecules Using Superchiral Fields. *Nat. Nanotechnol.* **2010**, *5*, 783–787.

(67) Mohammadi, E.; Tsakmakidis, K. L.; Askarpour, A. N.; Dehkhoda, P.; Tavakoli, A.; Altug, H. Nanophotonic Platforms for Enhanced Chiral Sensing. *ACS Photonics* **2018**, *5*, 2669–2675.

(68) Mohammadi, E.; Tavakoli, A.; Dehkhoda, P.; Jahani, Y.; Tsakmakidis, K. L.; Tittl, A.; Altug, H. Accessible Superchiral Near-Fields Driven by Tailored Electric and Magnetic Resonances in All-Dielectric Nanostructures. *ACS Photonics* **2019**, *6*, 1939–1946.

(69) Kwon, D.-H.; Werner, P. L.; Werner, D. H. Optical Planar Chiral Metamaterial Designs for Strong Circular Dichroism and Polarization Rotation. *Opt. Express* **2008**, *16*, 11802.

(70) Luo, Y.; Chi, C.; Jiang, M.; Li, R.; Zu, S.; Li, Y.; Fang, Z. Plasmonic Chiral Nanostructures: Chiroptical Effects and Applications. *Adv. Opt. Mater.* **2017**, *5*, 1700040.

(71) Fan, Z.; Govorov, A. O. Plasmonic Circular Dichroism of Chiral Metal Nanoparticle Assemblies. *Nano Lett.* **2010**, *10*, 2580–2587.

(72) Burford, B. P.; Robison, B. H. Bioluminescent Backlighting Illuminates the Complex Visual Signals of a Social Squid in the Deep Sea. *Proc. Natl. Acad. Sci.* **2020**, *117*, 8524–8531.

(73) Shcheslavskiy, V. I.; Neubauer, A.; Bukowiecki, R.; Dinter, F.; Becker, W. Combined Fluorescence and Phosphorescence Lifetime Imaging. *Appl. Phys. Lett.* **2016**, *108*, 091111.

(74) Horrocks, W. D.; Sudnick, D. R. Lanthanide Ion Luminescence Probes of the Structure of Biological Macromolecules. *Acc. Chem. Res.* **1981**, *14*, 384–392.

(75) Iwamura, M.; Kimura, Y.; Miyamoto, R.; Nozaki, K. Chiral Sensing Using an Achiral Europium(III) Complex by Induced Circularly Polarized Luminescence. *Inorg. Chem.* **2012**, *51*, 4094–4098.

(76) Lunstroot, K.; Driesen, K.; Nockemann, P.; Görller-Walrand, C.; Binnemans, K.; Bellayer, S.; Le Bideau, J.; Vioux, A. Luminescent Ionogels Based on Europium-Doped Ionic Liquids Confined within Silica-Derived Networks. *Chem. Mater.* **2006**, *18*, 5711–5715.

(77) Hatanaka, M.; Yabushita, S. Mechanisms of f–f Hypersensitive Transition Intensities of Lanthanide Trihalide Molecules: A Spin–Orbit Configuration Interaction Study. *Theor. Chem. Acc.* **2014**, *133*, 1517.

(78) Piksova, K.; Koštejn, M.; Grym, J. Characterization of Eu2O3 Nanolayers Deposited on Semiconductors. *NANOCON 2011 - Conf. Proceedings, 3rd Int. Conf.* **2011**, 715–718.

(79) Puntus, L. N.; Zolin, V. F.; Kudryashova, V. A.; Tsaryuk, V. I.; Legendziewicz, J.; Gawryszewska, P.; Szostak, R. Charge Transfer Bands in the Eu3+ Luminescence Excitation Spectra of Isomeric Europium Pyridine-Dicarboxylates. *Phys. Solid State* **2002**, *44*, 1440–1444.

(80) Judd, B. R. Optical Absorption Intensities of Rare-Earth Ions. *Phys. Rev.* **1962**, *127*, 750–761.

(81) Ofelt, G. S. Intensities of Crystal Spectra of Rare-Earth Ions. *J. Chem. Phys.* **1962**, *37*, 511–520.

(82) Walsh, B. M. Judd-Ofelt Theory: Principles and Practices. In *Advances in Spectroscopy for Lasers and Sensing*; Di Bartolo, B., Forte, O., Eds.; Springer Netherlands: Dordrecht, 2006; pp 403–433.

(83) Binnemans, K. Interpretation of Europium(III) Spectra. *Coord. Chem. Rev.* **2015**, *295*, 1–45.

(84) Carnall, W. T.; Crosswhite, H.; Crosswhite, H. M. *Energy Level Structure and Transition Probabilities in the Spectra of the Trivalent Lanthanides in LaF_3*; Argonne, IL (United States), 1978.

(85) Werts, M. H. V.; Jukes, R. T. F.; Verhoeven, J. W. The Emission Spectrum and the Radiative Lifetime of Eu3+ in Luminescent Lanthanide Complexes. *Phys. Chem. Chem. Phys.* **2002**, *4*, 1542–1548.

(86) Judd, B. R. Ionic Transitions Hypersensitive to Environment. *J. Chem. Phys.* **1979**, *70*, 4830–4833.

(87) Henrie, D. E.; Fellows, R. L.; Choppin, G. R. Hypersensitivity in the Electronic Transitions of Lanthanide and Actinide Complexes. *Coord. Chem. Rev.* **1976**, *18*, 199–224.

(88) Souza, A. S.; Couto dos Santos, M. A. The J-Mixing Effect in Ln3+ Ions Crystal Field Levels. *Chem. Phys. Lett.* **2012**, *521*, 138–141.

(89) Gadegaard, N.; Mosler, S.; Larsen, N. B. Biomimetic Polymer Nanostructures by Injection Molding. *Macromol. Mater. Eng.* **2003**, *288*, 76–83.

(90) Karimullah, A. S.; Jack, C.; Tullius, R.; Rotello, V. M.; Cooke, G.; Gadegaard, N.; Barron, L. D.; Kadodwala, M. Disposable Plasmonics: Plastic Templated Plasmonic Metamaterials with Tunable Chirality. *Adv. Mater.* **2015**, *27*, 5610–5616.

(91) Kelly, C.; Tullius, R.; Lapthorn, A. J.; Gadegaard, N.; Cooke, G.; Barron, L. D.; Karimullah, A. S.; Rotello, V. M.; Kadodwala, M. Chiral Plasmonic Fields Probe Structural Order of Biointerfaces. *J. Am. Chem. Soc.* **2018**, *140*, 8509–8517.

(92) Vericat, C.; Vela, M. E.; Benitez, G.; Carro, P.; Salvarezza, R. C. Self-Assembled Monolayers of Thiols and Dithiols on Gold: New Challenges for a Well-Known System. *Chem. Soc. Rev.* **2010**, *39*, 1805.

(93) Kelly, C.; Khosravi Khorashad, L.; Gadegaard, N.; Barron, L. D.; Govorov, A. O.; Karimullah, A. S.; Kadodwala, M. Controlling Metamaterial Transparency with Superchiral Fields. *ACS Photonics* **2017**, acsphotonics.7b01071.

(94) Govorov, A. O.; Gun'ko, Y. K.; Slocik, J. M.; Gérard, V. A.; Fan, Z.; Naik, R. R. Chiral Nanoparticle Assemblies: Circular Dichroism, Plasmonic Interactions, and Exciton Effects. *J. Mater. Chem.* **2011**, *21*, 16806.

(95) Gautier, C.; Bürgi, T. Chiral Gold Nanoparticles. *ChemPhysChem* **2009**, *10*, 483–492.

(96) Govorov, A. O.; Fan, Z. Theory of Chiral Plasmonic Nanostructures Comprising Metal Nanocrystals and Chiral Molecular Media. *ChemPhysChem* **2012**, *13*, 2551–2560.

(97) Decker, M.; Klein, M. W.; Wegener, M.; Linden, S. Circular Dichroism of Planar Chiral Magnetic Metamaterials. **2007**.

(98) Peng, B.; Özdemir, Ş. K.; Chen, W.; Nori, F.; Yang, L. What Is and What Is Not Electromagnetically Induced Transparency in Whispering-Gallery Microcavities. *Nat. Commun.* **2014**, *5*, 5082.

(99) Milne, D. F.; Korolkova, N. Electromagnetically Induced Invisibility Cloaking. *arXiv Prepr. arXiv1206.3944* **2012**, No. 2.

(100) Kang, L.; Hao Jiang, Z.; Yue, T.; Werner, D. H. Handedness Dependent Electromagnetically Induced Transparency in Hybrid Chiral Metamaterials. *Sci. Rep.* **2015**, *5*, 12224.

(101) Autler, S. H.; Townes, C. H. Stark Effect in Rapidly Varying Fields. *Phys. Rev.* **1955**, *100*, 703–722.

(102) Piotrowicz, M. J.; MacCormick, C.; Kowalczyk, A.; Bergamini, S.; Beterov, I. I.; Yakshina, E. A. Measurement of the Electric Dipole Moments for Transitions to Rubidium Rydberg States via Autler–Townes Splitting. *New J. Phys.* **2011**, *13*, 093012.

(103) Ahmed, E. H.; Ingram, S.; Kirova, T.; Salihoglu, O.; Huennekens, J.; Qi, J.; Guan, Y.; Lyyra,

A. M. Quantum Control of the Spin-Orbit Interaction Using the Autler-Townes Effect. *Phys. Rev. Lett.* **2011**, *107*, 163601.

(104) Liu, J.; Yang, H.; Wang, C.; Xu, K.; Xiao, J. Experimental Distinction of Autler-Townes Splitting from Electromagnetically Induced Transparency Using Coupled Mechanical Oscillators System. *Sci. Rep.* **2016**, *6*, 19040.

(105) Giner, L.; Veissier, L.; Sparkes, B.; Sheremet, A. S.; Nicolas, A.; Mishina, O. S.; Scherman, M.; Burks, S.; Shomroni, I.; Kupriyanov, D. V.; Lam, P. K.; Giacobino, E.; Laurat, J. Experimental Investigation of the Transition between Autler-Townes Splitting and Electromagnetically-Induced-Transparency Models. *Phys. Rev. A* **2013**, *87*, 013823.

(106) Anisimov, P. M.; Dowling, J. P.; Sanders, B. C. Objectively Discerning Autler-Townes Splitting from Electromagnetically Induced Transparency. *Phys. Rev. Lett.* **2011**, *107*, 163604.

(107) Liu, N.; Langguth, L.; Weiss, T.; Kästel, J.; Fleischhauer, M.; Pfau, T.; Giessen, H. Plasmonic Analogue of Electromagnetically Induced Transparency at the Drude Damping Limit. *Nat. Mater.* **2009**, *8*, 758–762.

(108) Lin, H.; Yang, D.; Han, S.; Liu, Y.; Yang, H. Analog Electromagnetically Induced Transparency for Circularly Polarized Wave Using Three-Dimensional Chiral Metamaterials. *Opt. Express* **2016**, *24*, 30068.

(109) Zhang, S.; Genov, D. a.; Wang, Y.; Liu, M.; Zhang, X. Plasmon-Induced Transparency in Metamaterials. *Phys. Rev. Lett.* **2008**, *101*, 047401.

(110) Tassin, P.; Zhang, L.; Zhao, R.; Jain, A.; Koschny, T.; Soukoulis, C. M. Electromagnetically Induced Transparency and Absorption in Metamaterials: The Radiating Two-Oscillator Model and Its Experimental Confirmation. *Phys. Rev. Lett.* **2012**, *109*, 187401.

(111) Landauer, R. Electrical Conductivity in Inhomogeneous Media. **2008**, *2*, 2–45.

(112) Abdulrahman, N. A.; Fan, Z.; Tonooka, T.; Kelly, S. M.; Gadegaard, N.; Hendry, E.; Govorov, A. O.; Kadodwala, M. Induced Chirality through Electromagnetic Coupling between Chiral Molecular Layers and Plasmonic Nanostructures. *Nano Lett.* **2012**, *12*, 977–983.

(113) Collins, J. T.; Kuppe, C.; Hooper, D. C.; Sibilia, C.; Centini, M.; Valev, V. K. Chirality and Chiroptical Effects in Metal Nanostructures: Fundamentals and Current Trends. *Adv. Opt. Mater.* **2017**, *5*, 1700182.

(114) Luk'yanchuk, B.; Zheludev, N. I.; Maier, S. A.; Halas, N. J.; Nordlander, P.; Giessen, H.; Chong, C. T. The Fano Resonance in Plasmonic Nanostructures and Metamaterials. *Nat. Mater.* **2010**, *9*, 707–715.

(115) Sadiku, M. N. O. A Simple Introduction to Finite Element Analysis of Electromagnetic Problems. *IEEE Trans. Educ.* **1989**, *32*, 85–93.

(116) Hakoda, C.; Rose, J.; Shokouhi, P.; Lissenden, C. Using Floquet Periodicity to Easily Calculate Dispersion Curves and Wave Structures of Homogeneous Waveguides. In *AIP Conference Proceedings*; 2018; Vol. 1949, p 020016.

(117) Bassiri, S.; Papas, C. H.; Engheta, N. Electromagnetic Wave Propagation through a Dielectric–Chiral Interface and through a Chiral Slab: Errata. *J. Opt. Soc. Am. A* **1990**, *7*, 2154.

(118) Theron, I. P.; Cloete, J. H. The Electric Quadrupole Contribution to the Circular Birefringence of Nonmagnetic Anisotropie Chiral Media: A Circular Waveguide Experiment. *IEEE Trans. Microw. Theory Tech.* **1996**, *44*, 1451–1459.

(119) Bürck, J.; Wadhwani, P.; Fanghänel, S.; Ulrich, A. S. Oriented Circular Dichroism: A Method to Characterize Membrane-Active Peptides in Oriented Lipid Bilayers. *Acc. Chem. Res.* **2016**, *49*, 184–192.

(120) Zhang, H.; Govorov, A. O. Giant Circular Dichroism of a Molecule in a Region of Strong Plasmon Resonances between Two Neighboring Gold Nanocrystals. *Phys. Rev. B* **2013**, *87*, 075410.

(121) Bochenkov, V.; Shabatina, T. Chiral Plasmonic Biosensors. *Biosensors* **2018**, *8*, 120.

(122) Silin, V.; Weetall, H.; Vanderah, D. J. SPR Studies of the Nonspecific Adsorption Kinetics of Human IgG and BSA on Gold Surfaces Modified by Self-Assembled Monolayers (SAMs). *J. Colloid Interface Sci.* **1997**, *185*, 94–103.

(123) Chen, S.; Liu, L.; Zhou, J.; Jiang, S. Controlling Antibody Orientation on Charged Self-Assembled Monolayers. *Langmuir* **2003**, *19*, 2859–2864.

(124) ANKER, J. N.; HALL, W. P.; LYANDRES, O.; SHAH, N. C.; ZHAO, J.; VAN DUYNE, R. P. Biosensing with Plasmonic Nanosensors. In *Nanoscience and Technology*; Co-Published with Macmillan Publishers Ltd, UK, 2009; Vol. 7, pp 308–319.

(125) Mollerup, J. M. A Review of the Thermodynamics of Protein Association to Ligands, Protein Adsorption, and Adsorption Isotherms. *Chem. Eng. Technol.* **2008**, *31*, 864–874.

(126) Zhang, W.; Wu, T.; Wang, R.; Zhang, X. Surface-Enhanced Circular Dichroism of Oriented Chiral Molecules by Plasmonic Nanostructures. *J. Phys. Chem. C* **2017**, *121*, 666–675.

(127) Jahani, S.; Jacob, Z. All-Dielectric Metamaterials. *Nat. Nanotechnol.* **2016**, *11*, 23–36.

(128) Wang, Q.; Rogers, E. T. F.; Gholipour, B.; Wang, C.-M.; Yuan, G.; Teng, J.; Zheludev, N. I. Optically Reconfigurable Metasurfaces and Photonic Devices Based on Phase Change Materials. *Nat. Photonics* **2016**, *10*, 60–65.

(129) Kelly, C.; MacLaren, D. A.; McKay, K.; McFarlane, A.; Karimullah, A. S.; Gadegaard, N.; Barron, L. D.; Franke-Arnold, S.; Crimin, F.; Götte, J. B.; Barnett, S. M.; Kadodwala, M.

Controlling the Symmetry of Inorganic Ionic Nanofilms with Optical Chirality. *Nat. Commun.* **2020**, *11*, 5169.

(130) Kakkar, T.; Keijzer, C.; Rodier, M.; Bukharova, T.; Taliansky, M.; Love, A. J.; Milner, J. J.; Karimullah, A. S.; Barron, L. D.; Gadegaard, N.; Lapthorn, A. J.; Kadodwala, M. Superchiral near Fields Detect Virus Structure. *Light Sci. Appl.* **2020**, *9*, 195.

(131) Wu, Z.; Chen, X.; Wang, M.; Dong, J.; Zheng, Y. High-Performance Ultrathin Active Chiral Metamaterials. *ACS Nano* **2018**, *12*, 5030–5041.

(132) Konishi, K.; Nomura, M.; Kumagai, N.; Iwamoto, S.; Arakawa, Y.; Kuwata-Gonokami, M. Circularly Polarized Light Emission from Semiconductor Planar Chiral Nanostructures. *Phys. Rev. Lett.* **2011**, *106*, 057402.

(133) Gilroy, C.; Hashiyada, S.; Endo, K.; Karimullah, A. S.; Barron, L. D.; Okamoto, H.; Togawa, Y.; Kadodwala, M. Roles of Superchirality and Interference in Chiral Plasmonic Biodetection. *J. Phys. Chem. C* **2019**, *123*, 15195–15203.

(134) Beth, R. A. Mechanical Detection and Measurement of the Angular Momentum of Light. *Phys. Rev.* **1936**, *50*, 115–125.

(135) Juan, M. L.; Righini, M.; Quidant, R. Plasmon Nano-Optical Tweezers. *Nat. Photonics* **2011**, *5*, 349–356.

(136) Padgett, M.; Bowman, R. Tweezers with a Twist. *Nat. Photonics* **2011**, *5*, 343–348.

(137) Babiker, M.; Power, W. L.; Allen, L. Light-Induced Torque on Moving Atoms. *Phys. Rev. Lett.* **1994**, *73*, 1239–1242.

(138) Shimomura, K.; Ikai, T.; Kanoh, S.; Yashima, E.; Maeda, K. Switchable Enantioseparation Based on Macromolecular Memory of a Helical Polyacetylene in the Solid State. *Nat. Chem.* **2014**, *6*, 429–434.

(139) Kim, M.-J.; Shin, B.-G.; Kim, J.-J.; Kim, D.-Y. Photoinduced Supramolecular Chirality in Amorphous Azobenzene Polymer Films. *J. Am. Chem. Soc.* **2002**, *124*, 3504–3505.

(140) Noorduin, W. L.; Bode, A. A. C.; van der Meijden, M.; Meekes, H.; van Etteger, A. F.; van Enckevort, W. J. P.; Christianen, P. C. M.; Kaptein, B.; Kellogg, R. M.; Rasing, T.; Vlieg, E. Complete Chiral Symmetry Breaking of an Amino Acid Derivative Directed by Circularly Polarized Light. *Nat. Chem.* **2009**, *1*, 729–732.

(141) Poulikakos, L. V.; Gutsche, P.; McPeak, K. M.; Burger, S.; Niegemann, J.; Hafner, C.; Norris, D. J. Optical Chirality Flux as a Useful Far-Field Probe of Chiral Near Fields. *ACS Photonics* **2016**, *3*, 1619–1625.

(142) Barnett, S. M.; Cameron, R. P.; Yao, A. M. Duplex Symmetry and Its Relation to the

Conservation of Optical Helicity. *Phys. Rev. A* **2012**, *86*, 013845.

(143) Cameron, R. P.; Barnett, S. M.; Yao, A. M. Optical Helicity, Optical Spin and Related Quantities in Electromagnetic Theory. *New J. Phys.* **2012**, *14*, 053050.

(144) Jayaraj, M. .; Vallabhan, C. P. . Dielectric and Optical Properties of Europium Oxide Films. *Thin Solid Films* **1989**, *177*, 59–67.

(145) Mariscal, A.; Quesada, A.; Camps, I.; Palomares, F. J.; Fernández, J. F.; Serna, R. Tuning Eu3+ Emission in Europium Sesquioxide Films by Changing the Crystalline Phase. *Appl. Surf. Sci.* **2016**, *374*, 71–76.

(146) Sheng, K. C.; Korenowski, G. M. Laser-Induced Optical Emission Studies of Europium(3+) Sites in Polycrystalline Powders of Monoclinic and Bcc. Europium Sesquioxide. *J. Phys. Chem.* **1988**, *92*, 50–56.

(147) Tanner, P. A. Some Misconceptions Concerning the Electronic Spectra of Tri-Positive Europium and Cerium. *Chem. Soc. Rev.* **2013**, *42*, 5090.

(148) Takizawa, S.; Tokizane, Y.; Miyamoto, K.; Morita, R.; Takahashi, F.; Omatsu, T.; Toyoda, K. Transfer of Light Helicity to Nanostructures. *Phys. Rev. Lett.* **2013**, *110*, 1–5.

(149) Toyoda, K.; Miyamoto, K.; Aoki, N.; Morita, R.; Omatsu, T. Using Optical Vortex To Control the Chirality of Twisted Metal Nanostructures. *Nano Lett.* **2012**, *12*, 3645–3649.

(150) Güler, M.; Güler, E. High Pressure Phase Transition and Elastic Behavior of Europium Oxide. *J. Optoelectron. Adv. Mater.* **2014**, *16*, 1322–1327.

(151) Tsuchiya, T.; Kawamura, K. Systematics of Elasticity: Ab Initio Study in B1-Type Alkaline Earth Oxides. *J. Chem. Phys.* **2001**, *114*, 10086–10093.

(152) Yoo, S.; Park, Q.-H. Chiral Light-Matter Interaction in Optical Resonators. *Phys. Rev. Lett.* **2015**, *114*, 203003.